Microwave-Assisted Solvothermal Synthesis and Optical Characterization of $M(RE)F_4$ (M – Alkali Metal; RE – Rare-Earth Metal) Nano- and Microscale Particles

Nikita Panov

A thesis submitted to the University of Ottawa
in partial fulfillment of the requirements for the
Master's degree in Chemistry

Department of Chemistry and Biomolecular Sciences
Faculty of Science
University of Ottawa

Abstract

Interest in rare-earth-doped crystalline materials, *e.g.*, $M(RE)F_4$ (M – alkali metal, RE – rare-earth metal), featuring unique optical properties such as light upconversion and downshifting is experiencing a surge due to the broad spectrum of applications that these photonic systems are facilitating. The development of reliable synthetic methods that grant rapid access to these materials is therefore of great importance. Microwave-assisted synthesis is appealing in this regard, because microwave radiation enables rapid and uniform heating of the reaction mixture and allows for rigid control of the reaction conditions, factors that facilitate the production of high-quality materials within minutes. Surprisingly, the investigation around microwave-assisted synthesis of $M(RE)F_4$ materials featuring upconversion and downshifting luminescence is limited. Methods that have already been developed predominately target Na-based systems, despite the evidence that the Li-based analogues also display excellent optical properties. In fact, only a single microwave-assisted approach toward a nanoscale Li-based system has been reported to date, while to my knowledge, no report of a microwave-assisted synthesis of a microscale Li-based system existed prior to the commencement of the work presented in this thesis. The challenge lies in the fact that access to $Li(RE)F_4$ is not easily achieved through a simple substitution of the alkali metal source in the established protocols that yield $Na(RE)F_4$; rather, a complete re-optimization of the synthesis method is required. This particular challenge was successfully addressed in this work.

Presented and discussed in **Chapter 3** of this thesis is a rapid microwave-assisted solvothermal synthesis approach toward both upconverting and downshifting $LiYF_4:RE^{3+}$ microparticle systems. More specifically, it is detailed how the rigorous optimization of the reaction temperature/duration profile, initial reaction mixture pH, and ratio of the metal precursors was necessary in gaining control over the crystalline phase, morphology, and size of the microparticles under microwave-induced solvothermal conditions. Importantly, a materials growth mechanism involving the depletion of a Li-free crystal phase, followed by a particle ripening process is also proposed. Moreover, the versatility of the developed method is highlighted by showcasing how it can be extended toward the synthesis of other relevant Li- and Na-based $M(RE)F_4$ nano- and microscale materials (*i.e.*, $LiYbF_4$, $NaYF_4$,

and $NaGdF_4$) featuring upconversion luminescence. Lastly, potential challenges associated with microwave-assisted synthesis are discussed, and appropriate solutions are proposed.

The upconversion and downshifting luminescence of the $M(RE)F_4$ materials attained *via* the developed synthesis approach is investigated in **Chapter 4**. The first part of the chapter provides a general assessment of the characteristic luminescence generated by the $M(RE)F_4$ materials featuring various RE^{3+} dopant systems. The second part of the chapter is devoted to a much more thorough single-particle investigation of the anisotropic luminescence behaviour exhibited by the $LiYF_4:RE^{3+}$ microparticles *via* hyperspectral imaging, polarized emission spectroscopy, and optical trapping.

It is my hope that you, the reader, will find the work presented in this thesis stimulating from two vantage points – from the development of the most rapid microwave-assisted solvothermal synthesis of upconverting and downshifting $M(RE)F_4$ nano/microscale materials reported to date, as well as from the utilization of specialized luminescence characterization techniques to provide fundamental insight into a seldom-considered luminescence property of crystalline materials such as $LiYF_4$.

Acknowledgements

It is the job of every scientist to venture into the unknown and to return with new insight. At the time of exploration, a scientist is tethered to the realm of known facts by a mere hypothesis, the strength of which is directly proportional to the degree of their wisdom. However, irrespective of age and experience, every scientist is humbled on occasion when this tether breaks, and one is plunged, head-first, into the chaos of what at first glance seems to be irreconcilable nonsense. Often humiliated, a *Good* scientist makes their way back to the realm of known facts remembering what they have seen, re-assesses the situation, strengthens their hypothesis tether, and ventures out once again. It takes true strength and character to choose the act of expanding the boundaries of perceived objective reality as a profession. It takes being a *Good* scientist. I have been lucky enough to conduct research alongside such individuals and to learn from them. I admire their diligence and perseverance, and I aspire to resemble them in what ever endeavour. To these individuals, I want to express my gratitude.

I want to thank my supervisor Prof. Eva Hemmer for her endless patience, for seeing in me what I couldn't see myself, for challenging me to grow both professionally and personally, and for accommodating my inter-continental long-distance relationship with a girl that is now my wife! Dear Eva, thank you for your guidance, honesty, and involvement – I consider myself very lucky for having joined your research group.

I want to thank Dr. Riccardo Marin for showing me what it takes to be an excellent leader, an inspiring role model, and a source of positive energy for all and always. Riccardo, you have set a very high bar. "*Lavora, carogna*!" 4 LiYF.

I want to thank my colleagues and mentors at the Universidad Autónoma de Madrid, especially Prof. Daniel Jaque and Prof. Patricia Haro, for welcoming me into their research group and for helping me navigate the world of photonics during my three-month long stay.

I want to thank all of my other Hemmer Group colleagues: Dr. Emille Martinazzo Rodriguez for her kindness and positivity; Ilias Halimi for our engaging, loud, though-provoking, and good-spirited political discussions; Nan Liu for her enthusiasm and endless supply of Chinese snacks; and lastly, all past members of the Hemmer Group for showing

me the ropes, and all current members for patiently letting me exercise (not always) effective knowledge dissemination. Furthermore, I want to thank Dr. Yun Liu for her help with TEM/SEM measurements, Dr. Jeffrey Ovens for his help with the interpretation of crystallographic data, Prof. Tito Scaiano for provision of the fluorometer used for the optical study, and Prof. Javier Giorgi for provision of the FTIR pellet press.

Of course, I also want to express my gratitude to my *Good* (grand)parents for their love and support that can't be measured; my *Good* sister for motivating me to be a better brother; my *Good* friends, especially Camille Jesús Mirmiran and Dane Martin-Falla, for being there at the right place and at the right time; and my *Good* wife for being so patient and understanding during my writing of this thesis. Thank you all!

Table of contents

List of tables

List of figures

List of abbreviations

AR	Aspect ratio
ca.	*Circa* (approximately)
CMOS	Complementary metal oxide semiconductor
CCD	Charge-coupled device
EDS	Energy-dispersive X-ray spectroscopy
e.g.	*Exempli gratia* (for example)
EMCCD	Electron multiplying CCD
ESA	Excited state absorption
ETU	Energy transfer upconversion
FTIR	Fourier-transform infrared spectroscopy
GSA	Ground state absorption
ICP-MS	Inductively coupled plasma mass spectrometry
i.e.	*Id est* (that is to say)
IR	Infrared
MRICTS	Microwave reactor infrared camera temperature sensor
M	Alkali metal
NA	Numerical aperture
NIR	Near-infrared
OA	Optic axis
OS	Oscillator strength
PP	Polypropylene
RCF	Relative centrifugal force
RE	Rare-earth metal
RM	Reaction mixture
S	Substrate
SEM	Scanning electron microscopy
TEM	Transition electron microscopy
UV	Ultraviolet
Vis	Visible
vide infra	See below
vide supra	See above
vs.	*Versus* (in contrast to)
XRD	X-ray diffraction

List of symbols

α	Polarization state ($\vec{E}$ and $\vec{M} \perp$ OA)
β	Angle between OA and S
α-, β-Na(RE)F_4	Cubic and hexagonal crystalline phase Na(RE)F_4, respectively
ε	Molar absorptivity
ΔH	Enthalpy of vapourization
η	Upconversion efficiency
θ	Angle between $\vec{K}$ and OA
λ (λ_{EX}, λ_{EM})	Wavelength (excitation or emission, respectively)
ν	Frequency
π	Polarization state ($\vec{E} \parallel$ OA; $\vec{M} \perp$ OA)
ρ	Polarizability constant
σ	Polarization state ($\vec{E} \perp$ OA; $\vec{M} \parallel$ OA)
τ	Lifetime
ω	Linear polarizer angle
a, b, c; α, β, γ	Crystallographic lattice parameters
F_{Grad}	Gradient force
F_{Scat}	Scattering force
I_{Max}	Maximum value ratio (from polar plot)
I_{Min}	Minimum value ratio (from polar plot)
NPs	Nanoparticles of unidentified phase
P	Vapour pressure
pH	Power of hydrogen
R	Ideal gas constant
T (T_{NOM}, T_{TRUE})	Temperature (nominal or true, respectively)
V_{HS}	Headspace volume
V_{RM}	Reaction mixture volume
$\vec{E}$	Electric field vector
$\vec{K}$	Probed emission direction vector
$\vec{M}$	Magnetic field vector
$\parallel$	Parallel to…
$\perp$	Perpendicular to…

Statement of contribution

Some of the experimental data/results presented in this thesis were acquired by other technicians and colleagues. Hyperspectral images presented in **Figures 37-A/B-1**, **38-A-1/2**, and **40-A-1/2**, as well as photographs presented in **Figures 24-A/B** and **32** were acquired by my supervisor, Prof. Eva Hemmer. All SEM micrographs were acquired by Dr. Yun Liu, manager of the uOttawa Materials Characterization Core Facility. X-ray diffraction pattern simulation presented in **Figure 15** (and the figure itself) was performed (provided) by Dr. Riccardo Marin, a post-doctoral fellow in the Hemmer group. All other measurements and data analysis were performed by myself. Permission to reuse figures from other sources is provided in the captions of the respective figures.

A part of this thesis was reprinted (adapted) with permission from Panov, N., Marin, R., and Hemmer, E. Microwave-Assisted Solvothermal Synthesis of Upconverting and Downshifting Rare-Earth-Doped $LiYF_4$ Microparticles, *Inorg. Chem.* **2018**, *57*, 14920–14929. Copyright 2018 American Chemical Society. The respective article was written by myself, under the guidance of Dr. Riccardo Marin and Prof. Eva Hemmer. This thesis was written by myself, under the guidance of Prof. Eva Hemmer.

Chapter 1. Introduction

The lanthanide metal family is comprised of the first 15 f-block elements with atomic numbers ranging from 57 to 71, from lanthanum to lutetium, respectively.[1] Together with scandium and yttrium – the transition metal analogues – lanthanides are referred to as the rare-earth metals (REs).[I, 1] Albeit more abundant in nature than their name suggests, the current global demand for REs already exceeds the supply, and keeps rising further still.[2] Ultimately, this is a testament to the indispensable technological utility of the REs, which can be attributed to their unique spectroscopic and magnetic properties.[1] Because the work presented in this thesis revolves around optically active, RE-based materials only, the following discussion will be limited to their respective luminescence properties.

1.0. Historic background

In 1794, Johan *Gadolin* discovered a new element inside a mineral sample harvested from a mine located in the Swedish village of *Ytterby*.[3] Respectively, the element was named *Yttrium*, and the RE-rich mineral *Gadolinite*.[3] Four more REs (La, Ce, Tb, and Er) were discovered in time for Mendeleev's publication of the periodic table in 1869.[1]

Shortly after in 1891, Carl Auer von Welsbach commenced the technological development of RE-based devices by patenting a brightly-emitting gas mantle featuring ThO_2:Ce^{4+}.[1] Indeed, since then, luminescence generated by REs has enabled a plethora of technologies: *solid state lasers* (*e.g.*, $Y_3Al_5O_{12}$:Nd^{3+}), *increasingly efficient lighting and coloured television* (*e.g.*, red-emitting Y_2O_3:Eu^{3+}, green-emitting $LaPO_4$:Ce^{3+},Tb^{3+}, and blue-emitting $BaMgAl_{10}O_{17}$:Eu^{2+}), Er^{3+}-based *signal amplifiers in intercontinental submarine optical fibers*, *anticounterfeiting labels* (*e.g.*, ultraviolet (UV)- and near-infrared (NIR)-active RE^{3+} pigments in Euro and Chinese Yuan banknotes), *luminescent probes for biomedical assays* (*e.g.*, Eu^{3+}-chelate in the dissociation-enhanced lanthanide fluorescent immunoassay platform), and more.[1,4] Today, the advent of nanoscience has

[I] From here on, all lanthanides will be referred to as the rare-earth metals, abbreviated by RE (or RE^{3+}).

spurred the development of novel multifunctional RE-based materials for a wide range of other applications, such as: photodynamic and photothermal cancer therapy, nanothermometry, optogenetics, solar energy conversion, and photocatalysis.[1,4]

The avid reader may have noticed that all of the aforementioned applications utilize REs with non-zero oxidation states as part of an organometallic complex or incorporated into an inorganic crystalline host matrix. Indeed, what fosters the unique luminescence properties of the REs has a peculiar origin, explanation of which has challenged many great minds of the 19th and early 20th centuries. It was in the 1920s that Bethe, Kramers, and Bequerel proposed that a particular type of luminescence generated by most REs is a product of quantum-mechanically forbidden electronic transitions.[5] J. H. Van Vleck provided a plausible explanation for the respectively "most complicated spectra of any of the elements" in 1936,[6] and all mysticism was finally dispelled (for anyone well-versed in quantum mechanics…) by B. R. Judd and G. S. Ofelt in two independently-derived mathematic models published on the same day in 1962.[7–9] Within a year, G. H. Dieke's group provided the growing RE community with the Dieke diagram, an energy level diagram up to 40,000 cm^{-1} depicting assigned 4f electronic sublevels of the REs (*vide infra* **Figure 1**).[6] To this day, a printed copy of the original or since expanded Dieke diagram decorates the wall of every laboratory involved with RE-oriented research.[5]

The following sections of the introduction aim to provide the reader with a basic level of understanding of the origin of the unique luminescence properties of REs, the role of the inorganic crystalline host material in facilitating (and altering) this luminescence, and how the various forms of luminescence enable some of the aforementioned applications. In large, the following discussion will be limited to specific REs and inorganic host materials utilized in the context of this thesis. To gain a deeper understanding of the concepts discussed herein, the reader is kindly referred to many excellent reviews and publications referenced throughout the text.

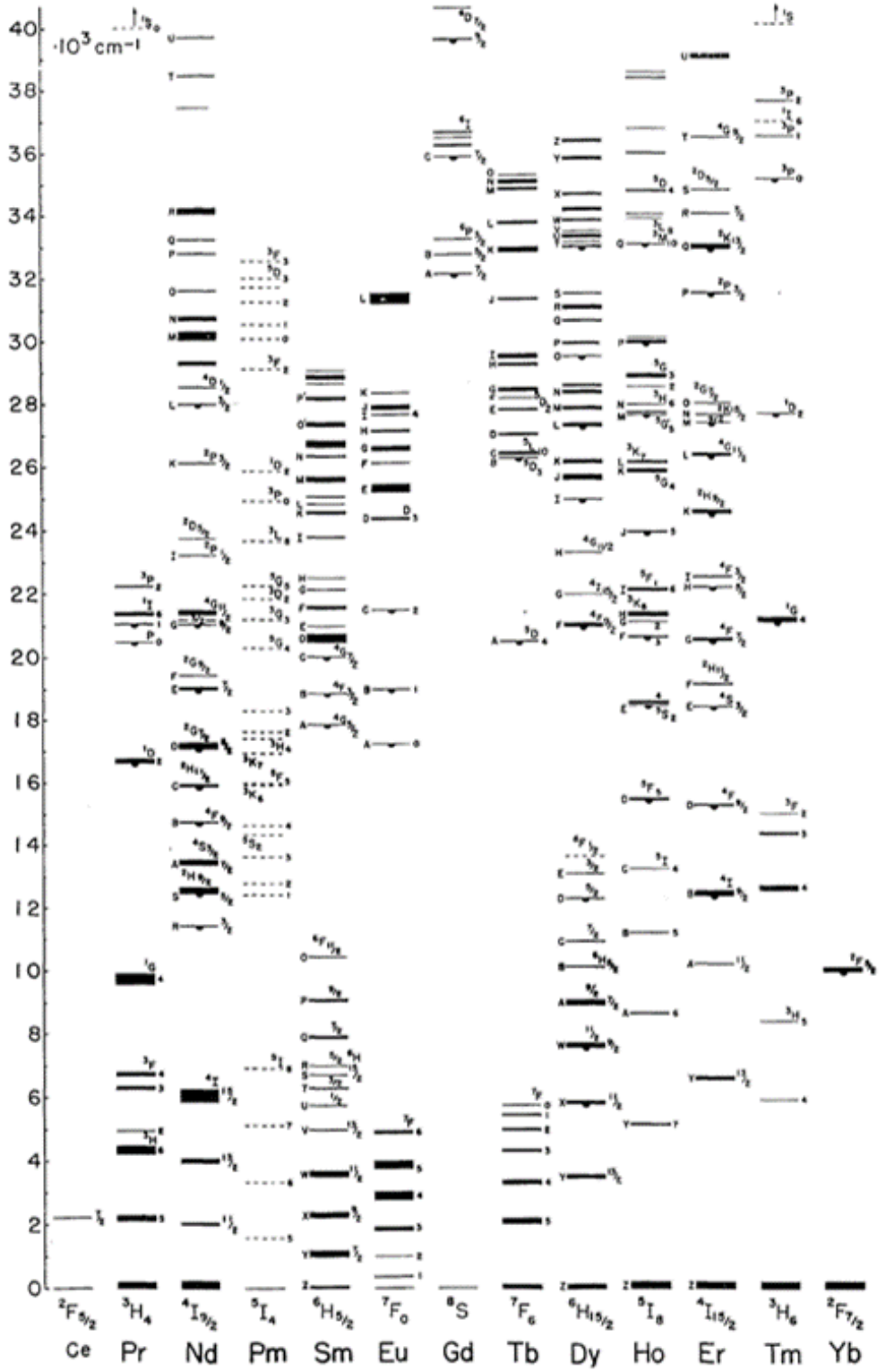

Figure 1. Original Dieke diagram depicting the energy levels of the trivalent RE^{3+} ions (up to 40,000 cm^{-1}). Reprinted with permission from Dieke, G. H., Crosswhite, H. M., and Dunn, B. J. *Opt. Soc. Am.* **1961**, *51*, 820. © The Optical Society.

1.1. RE-mediated luminescence

1.1.1. Effect of metal oxidation and ground state electronic structure

The formal, *i.e.*, "textbook", valence electronic configuration of La (n = 1), Ce (n = 2), Gd (n = 8), and Lu (n = 15) is $[Xe]4f^{n-1}5d^{1}6s^{2}$, and is $[Xe]4f^{n}6s^{2}$ for the remaining REs.[10] However, by far the most common electronic configuration for all REs is $[Xe]4f^{n-1}$ (n = 1 for La^{3+} and n = 15 for Lu^{3+}), which corresponds to the oxidation state of +III.[1] Oxidation states of +II and +IV can be also accessed by Eu and Yb, as well as Ce and Tb, respectively, due to the extra stabilization achieved upon obtaining an empty (Ce^{+4}), half-filled (Eu^{2+} and Tb^{4+}), and fully-filled (Yb^{2+}) 4f orbital.[II, 1]

A brief mention of the common RE oxidation states was important, because the respective ground state electronic configurations play a role in determining which electronic transitions can and cannot occur. For example, visible (Vis) light (470 nm) can stimulate a 4f ↔ 5d transition of the single $4f^{1}$ electron in Ce^{3+}.[11] Conversely, Ce^{4+} lacks the mobile $4f^{1}$ electron and can be rendered luminescent only when sensitized by a ligand-to-metal charge transfer, *e.g.*, upon excitation in the UV range, an electron is transferred from a valence band of Ce–O in Sr_2CeO_4 to the empty $4f^{0}$ configuration of Ce^{4+}; blue emission is then generated by subsequent relaxation from the $4f^{1}$ configuration of Ce^{3+} to the valence band of Ce-O.[12] Analogously, a $4f^{13}$ electron in Yb^{3+} can be forced to undergo an intraconfigurational 4f ↔ 4f rearrangement when stimulated by NIR radiation (980 nm).[13] However, the same rearrangement in Yb^{2+} is not possible due to a complete $4f^{14}$ configuration; instead, only UV/Vis-stimulated (280-660 nm) 4f ↔ 5d transitions can be triggered.[14] Lastly, La^{3+} and Lu^{3+} are not luminescent at all, because of very stable $4f^{0}$ and $4f^{14}$ configurations, respectively.[15] Because the work presented in this thesis exclusively involves RE^{3+}, it is appropriate to provide the following generalization: all RE^{3+} other than La^{3+}, Ce^{3+}, and Lu^{3+} exhibit *intra*configurational 4f ↔ 4f electronic

[II] Beyond Eu^{2+} and Yb^{2+}, all REs (expect for the radioactive Pm^{2+}) can access the +II oxidation state when part of specific organometallic complexes.[1]

transitions, whereas *inter*configurational 4f ↔ 5d transitions are limited to Ce^{3+}, Pr^{3+}, Tb^{3+}.[III, 4,15]

1.1.2. Selection rules for the 4f ↔ 4f and 4f ↔ 5d electronic transitions

A transition between two electronic states can be achieved by means of interaction of the respective electron with either the electric or magnetic components of the electromagnetic radiation, *i.e.*, electric dipole or quadrupole, and magnetic dipole transitions.[15] A set of selection rules with respect to quantum numbers *l* (orbital), S (total spin), L (total orbital), and J (total angular momentum), electronic state symmetry considerations, as well as the polarization of the excitation and emission radiation all govern the probability of a particular type of electronic transition between two specific electronic states.[15,16] In fact, one needs a relatively comprehensive understanding of group theory and its role in quantum mechanics to discuss this in detail. Nevertheless, Laporte selection rules, *i.e.*, those considering the orbital quantum number of any two participating electronic states, are most often invoked when introducing the peculiar nature of RE-mediated luminescence.[15,16]

As predicted by Van Vleck and later supported by the Judd-Ofelt theory, RE-mediated luminescence is dominated by electric dipole transitions, with magnetic dipole transitions being less common, and electric quadrupole transitions being essentially negligible.[6,9,15,16] With respect to electric dipole transitions, the Laporte rules state that the two respective electronic levels must have opposite parity, with parity being defined as $(-1)^l$ such that $(-1)^l = -1$ is odd and $(-1)^l = 1$ is even, and that the respective change in the angular momentum quantum number (Δl) must equal ±1.[17] By definition, s and d orbitals have even parities, whereas p and f orbitals have odd parities, because their respective angular momentum quantum numbers *l* are 0 (s), 1 (p), 2 (d), and 3 (f). Thus, it follows from the Laporte selection rules that RE-mediated luminescence *via* electric dipole transitions is

III More specifically, interconfigurational 4f ↔ 5d transitions are observed for Ce^{3+}, Pr^{3+}, Tb^{3+}, and the less common +II oxidation states of other REs in the common UV/Vis spectroscopic range. More broadly, however, such transitions can be forced by high energy (λ_{EX} 100-200 nm) vacuum ultraviolet excitation if the respective RE cation is in possession of at least one mobile $4f^n$ electron.[4]

only allowed for the d ↔ f transitions. Conversely, from the same set of rules it stems that magnetic dipole transitions are allowed only between states of identical parity, *e.g.*, f ↔ f.[15] From this, it may seem obvious that the aforementioned *inter*configurational 4f ↔ 5d electronic transitions in non-zerovalent REs are always of the electric-dipole type and that *intra*configurational 4f ↔ 4f transitions are always of the magnetic-dipole type. However, it is a fact that *intra*configurational 4f ↔ 4f electronic transitions in non-zerovalent REs are also primarily of the electric-dipole type, with magnetic dipole transitions accounting for only a few known cases, *e.g.*, $^5D_0 \rightarrow {}^7F_1$ transition in Eu^{3+} (*vide infra* state term notation $^{2S+1}L_J$).[16]

Suggesting, explaining, and proving that RE-mediated luminescence is primarily dependent on "Laporte-forbidden", *i.e.*, very low probability, electric dipole f ↔ f transitions was precisely the challenge that Bethe, Kramers, Bequerel, Van Vleck, Judd, Ofelt, and others struggled with from the 1920s to 1962. The result of their cumulative work can be summarized as such – formally forbidden electric dipole 4f ↔ 4f transitions in non-zerovalent REs become partially allowed, *i.e.*, can be "induced", only when the RE cation is exposed to a non-centrosymmetric electric field, which results in an admixture of the $4f^n$ configuration with higher energy configurations of opposite parity.[8,9,18] In practise, this can be achieved *via* substitutional incorporation (doping) of non-zerovalent REs into crystalline host matrices featuring non-centrosymmetric crystal fields, *i.e.*, those defined by point groups lacking the inversion symmetry element.[17] However, as discussed in the next section, doing so carries considerable implications for the spectroscopic properties of both 4f ↔ 4f and 4f ↔ 5d electronic transitions.

1.1.3. Spectral properties of the 4f ↔ 4f and 4f ↔ 5d electronic transitions

Having outlined the origin of both formally forbidden (induced electric dipole 4f ↔ 4f transitions) and allowed (4f ↔ 5d transitions) RE-mediated luminescence, it is important to provide a brief discussion of the spectroscopic differences between the 4f ↔ 4f and 4f ↔ 5d electronic transitions, as well as between 4f ↔ 4f transitions themselves. To do so, it is important to consider the differences in the Laporte-governed probability between

the 4f ↔ 4f and 4f ↔ 5d transitions and in the susceptibility of the respective $4f^n$ and $5d^n$ configurations to crystal field influence.

The first spectroscopic difference between the electric dipole 4f ↔ 5d and induced electric dipole 4f ↔ 4f transitions concerns the relative intensity of their respective spectral bands. Indeed, absorption and emission spectra depicting 4f ↔ 5d transitions is characterized by spectral bands of much higher intensity.[19] This is explained by the respective difference in the electric dipole transition probability, *i.e.*, order of magnitude of the oscillator strength (OS), between the Laporte-allowed 4f ↔ 5d (OS *ca*. 10^{-2}–10^{0}) transitions and the formally Laporte-forbidden 4f ↔ 4f (OS *ca*. 10^{-4}) transitions, the latter of which can be induced upon perturbance of the $4f^n$ configuration by a non-centrosymmetric crystal field.[17]

The second spectroscopic difference between the 4f ↔ 5d and 4f ↔ 4f electronic transitions concerns both the spectral band shape (broad *vs*. narrow) and position (high variation *vs*. low variation).[15,19] More specifically, spectral bands corresponding to the electric dipole 4f ↔ 5d transitions possess a relatively broad profile and their position, *i.e.*, energy difference between the participating electronic states, is very much dependent on the crystal field strength and symmetry.[15,19] Conversely, spectral bands corresponding to the electric dipole 4f ↔ 4f transitions are narrow, and their position is not as sensitive to crystal field influence.[16,19] An example of this spectral difference from the literature is provided in **Figure 2** (*vide infra*), which depicts a set of emission spectra obtained from $GdPO_4$:Ce^{3+}(20%)/Tb^{3+} nanorods as a function of increasing Tb^{3+} content (0.5-15%).[20]

As evident from **Figure 2**, the broad band centered at *ca*. 360 nm corresponds to a Laporte-allowed 5d → 4f electronic transition in Ce^{3+}, whereas the four narrow bands centered at 490 nm, 544 nm, 585 nm, and 620 nm, respectively, correspond to the Laporte-forbidden 4f → 4f electronic transitions in Tb^{3+} (more on this RE dopant pair in **Section 1.1.4.1**). It is also evident that as the crystal lattice of $GdPO_4$:Ce^{3+}(20%)/Tb^{3+}(0.5–15%) is distorted to a greater degree upon increasing Tb^{3+} doping content (due to a mismatch in ionic radii between the constituent ions), the Ce^{3+} emission band experiences a blue-shift, whereas no change in band position is observed for the four Tb^{3+} emission bands. In addition to the blue-shift, the Ce^{3+} emission band also experiences a decrease in intensity as the doping concentration of Tb^{3+} increases.

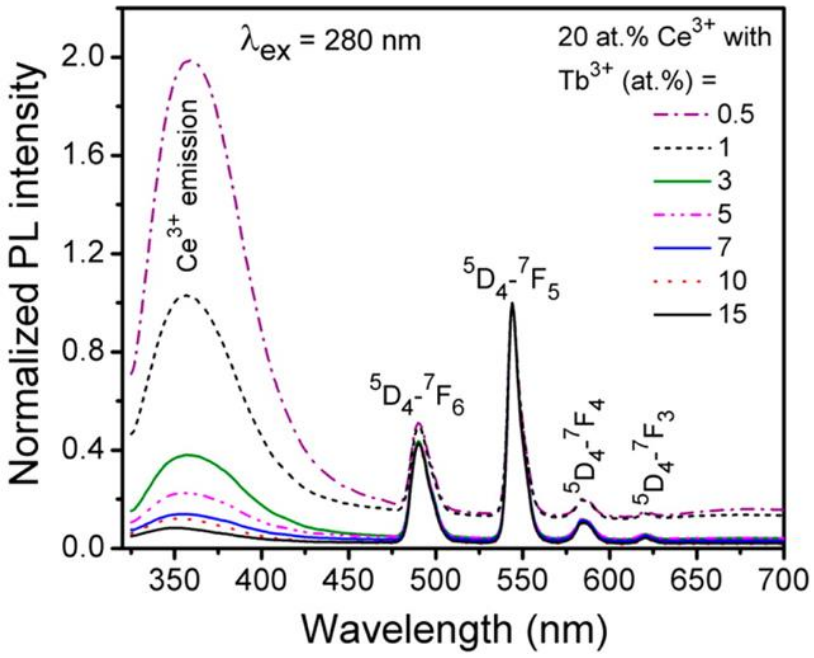

Figure 2. Normalized (at λ = 544 nm) emission spectra of $GdPO_4:Ce^{3+}$(20%)/Tb^{3+}(0.5–15%) under 280 nm excitation. Reprinted (adapted) with permission from Sahu, N. K. *et al.*, Ce^{3+}-Sensitized $GdPO_4:Tb^{3+}$ Nanorods: An Investigation on Energy Transfer, Luminescence Switching, and Quantum Yield, *ACS Photonics* **2014**, *1*, 337–346. Copyright 2014 American Chemical Society.

However, the two phenomena are unrelated. Whereas the blue-shift occurs as a result of a crystal lattice distortion (*vide infra*), the decrease in emission intensity is attributed to the increase in energy transfer efficiency from the excited (and emissive) 5d* level of Ce^{3+} to the ^5H_J levels of Tb^{3+}, from which the four typical Tb^{3+} emission bands are generated. Luminescence mediated by this dopant pair is described in more detail in **Section 1.1.4.1**.

The reason why the Ce^{3+} emission band experiences a shift in energy, whereas the Tb^{3+} emission bands do not can be explained by the difference in radial charge distribution of the $4f^n$ and $5d^n$ configurations and the consequent difference in their exposure to the local coordination environment, *i.e.*, ionic vibrations in the inner coordination sphere (which induce spectral band broadening) and crystal field symmetry (which influences spectral band position).[15,16,19]

To be precise, the core-like 4f orbital is almost entirely screened from the local coordination environment by the filled $5s^2$ and $5p^6$ orbitals, whereas the more spatially diffuse 5d orbital is not.[16,19] The crystal field strength experienced by the $5d^n$ configuration is thus much stronger in comparison with that experienced by the $4f^n$ configuration,

ca. 25,000 cm^{-1} *vs*. 500 cm^{-1}, respectively.[16] Hence, the electronic structure of the $5d^n$ configuration is subject to a greater degree of change as a function of the crystal field symmetry and strength in comparison to the electronic structure of the well-shielded $4f^n$ configuration. Nevertheless, that is not to say that the electronic structure of the $4f^n$ configuration is completely independent of crystal field influence. In fact, although spectral characteristics of the 4f ↔ 4f bands such as broadness and position are not subject to much variation, spectral band structure *i.e.*, spectral band resolution, is determined by crystal field symmetry.[16] An example from the literature is provided in **Figure 3**, which depicts a set of emission spectra obtained from various crystalline host materials doped with 2% of Eu^{3+}: hexagonal phase $NaLaF_4$, LaF_3, and $NaYF_4$, cubic phase $NaYF_4$, as well as tetragonal phase $LiYF_4$ and LaOF.[21]

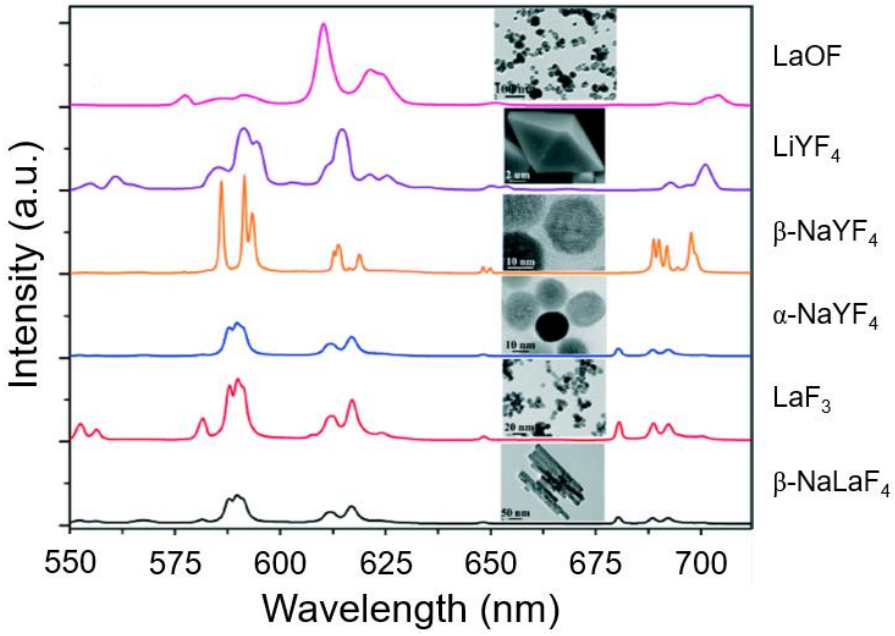

Figure 3. Spectra depicting Eu^{3+} emission from various crystalline host matrices doped with 2% Eu^{3+}: hexagonal phase (β) $NaLaF_4$, LaF_3, and $NaYF_4$, cubic phase (α) $NaYF_4$, as well as tetragonal phase $LiYF_4$ and LaOF. Emission was enabled with 395.5 nm excitation. TEM/SEM micrographs of the respective materials are presented. Republished with permission of Royal Society of Chemistry, from "The effects of structural characterization on the luminescence of Eu^{3+}-doped fluoride nano/microcrystals", Gao, D., Zhang, X., and Zhang, 16, 48, 2014; permission conveyed through Copyright Clearance Center, Inc.

It is evident from **Figure 3** that the position of the Eu^{3+} emission bands is largely unaffected by the change in crystalline environment, whereas the band resolution (and relative band intensity) varies rather significantly.

To understand the origin of this influence, it is necessary to consider the difference in electronic structure of the $4f^n$ configuration in a free RE ion *vs.* an ion exposed to a local crystal field. This can be achieved with the aid of a Russell-Saunders coupling scheme. As an example, a partial representation of a Russell-Saunders coupling scheme for Eu^{3+} ($4f^6$ configuration) in a crystal field defined by the O_h point group symmetry is depicted in **Figure 4**.[16]

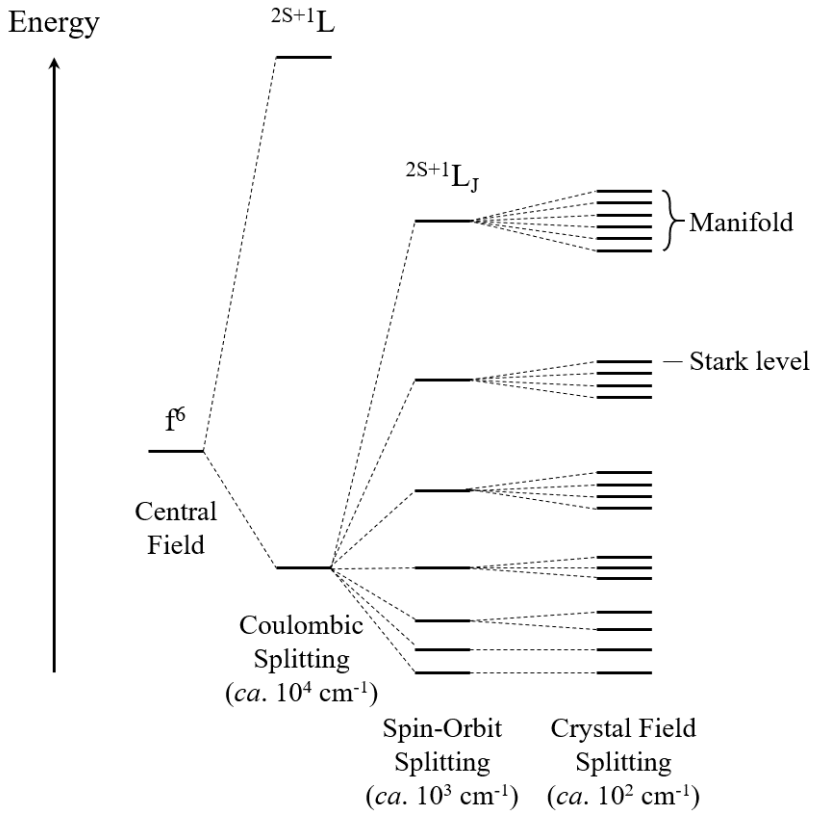

Figure 4. Russell-Saunders coupling scheme depicting the change in the electronic structure of the $4f^6$ configuration in a Eu^{3+} ion upon exposure to an octahedral (O_h) crystal field. Republished (redrawn) with permission (and modified) from Introduction to Lanthanide Ion Luminescence in Luminescence of Lanthanide Ions in Coordination Compounds and Nanomaterials, pg. 18, de Bettencourt-Dias, A., ed. De Bettencourt-Dias, A., John Wiley and Sons, Ltd., **2014**.

Although this particular case features a specific $4f^n$ configuration ($4f^6$) and a crystal field characterized by a specific symmetry (O_h), it sets the stage for a broader discussion about

crystal field influence on the electronic structures of $4f^n$ ($1 < n < 14$) configurations in non-zerovalent REs.

Firstly, it is evident from **Figure 4** that in the absence of a crystal field, the formal energy state of a particular $4f^n$ configuration is already split by Coulomb forces (order of 10^4 cm^{-1}) and spin-orbit coupling (order of 10^3 cm^{-1}) into distinct sublevels denoted by the $^{2S+1}L_J$ term symbols, *e.g.*, $^7F_6$, which summarize the quantum number information of the respective sublevels.[IV, 16] Secondly, an external crystal field induces additional splitting (order of 10^2 cm^{-1}) of the respective $^{2S+1}L_J$ sublevels into manifolds with varying numbers of Stark levels.[16] The number of distinct Stark levels in a particular manifold is determined by the point group of the crystal field and the J value of the respective $^{2S+1}L_J$ term symbol.[16]

Ultimately, whereas crystal field splitting plays a significant role in determining the spectral positions of 5d ↔ 4f bands, spectral positions of the 4f ↔ 4f bands are primarily determined by the splitting of the formal $4f^n$ energy states by Coulomb forces and spin-orbit coupling, the combined effect of which is rather large in comparison with further crystal field splitting of the resulting $^{2S+1}L_J$ sublevel energies.[16] Nevertheless, the low degree of symmetry-dependent crystal field splitting that is present determines the number of Stark levels comprising each manifold between which a particular 4f ↔ 4f electronic transition occurs, and thus influences the spectral resolution of the respective 4f ↔ 4f band.[22] In other words, lower crystal field symmetry increases the number of Stark levels in participating manifolds,[16] which increases the number of possible 4f ↔ 4f transitions between any two respective manifolds and hence increases the number of Stark bands comprising any one 4f ↔ 4f spectral band, *i.e.*, spectral resolution (*vide infra* **Figure 36** in **Section 4.2.2** for further experimental evidence of this effect). Referring back to **Figure 3**, it is evident that hexagonal phase $NaYF_4$ fosters the strongest crystal-field splitting of the Eu^{3+} $4f^6$ configuration, and thus yields an emission spectrum that is characterized by the highest emission band resolution in comparison to the emission spectra obtained from other Eu^{3+}-doped host matrices.

IV In the term symbol $^{2S+1}L_J$, 2S+1 is the spin multiplicity where S is the total spin quantum number (sum of spin quantum numbers m_s), L is the total orbital quantum number (sum of orbital quantum numbers *l*), and J is the total angular momentum quantum number ($J = |L + S|$ when $n > 7$ in $4f^n$ and $J = |L – S|$ when $n < 7$ in $4f^n$).[16]

Having provided the necessary level of insight into the origin of both RE-mediated luminescence and spectroscopic characteristics of the 4f ↔ 5d and 4f ↔ 4f transitions, it is now appropriate to introduce the various types of RE-mediated luminescence that feature these electronic transitions.

1.1.4. Types of RE-mediated luminescence (with applications)

One of the primary reasons for the existence of such a wide range of RE-enabled applications is due to the capacity of the REs to mediate various types of luminescence, namely downshifting, downconversion, and upconversion. In brief, the difference between these three types of luminescence lies in both the quantity and energy of photons that are absorbed and emitted.

Downshifting is the classic type of Stokes shift luminescence, *i.e.*, absorption of a single higher energy photon and emission of a single lower energy photon.[23] Downconversion, more broadly referred to as quantum cutting, is the absorption of a single higher energy photon and emission of multiple lower energy photons (this form of luminescence was not involved in this thesis and will not be discussed beyond this point).[24] And lastly, upconversion is a type of anti-Stokes shift luminescence, *i.e.*, absorption of multiple lower energy photons (typically NIR) and emission of a single higher energy photon (higher energy NIR, Vis, or UV).[23]

In theory, each type of luminescence can be enabled by a photonic system featuring a single RE ion type.[23,25] In fact, this is often the case for Nd^{3+}-mediated downshifting luminescence.[26–28] However, due to the forbidden nature of electric dipole 4f ↔ 4f transitions in a single ion, *i.e.*, low absorption and emission probabilities, more efficient downshifting and upconversion luminescence can be facilitated by sensitizing REs with the desirable emission characteristics, *e.g.*, Tb^{3+}, Er^{3+}, and Tm^{3+}, with better-absorbing REs, *e.g.*, Ce^{3+}, Yb^{3+}, Nd^{3+}.[23,29] Similarly, downconversion efficiency can be increased by employing multiple REs, *e.g.*, Gd^{3+} with Eu^{3+}, which mitigates the extent of competing, undesirable radiative relaxations that often plague downconversion luminescence mediated by photonic systems featuring a single RE ion type.[25]

What follows is a more thorough description of RE-mediated downshifting and upconversion luminescence. Examples used to illustrate the mechanisms by which both types of luminescence are fostered involve the RE dopant systems featured in this thesis, *e.g.*, Nd^{3+} and Ce^{3+}/Tb^{3+} for downshifting, and Yb^{3+}/RE^{3+} (RE^{3+} – Er^{3+} or Tm^{3+}) for upconversion. Moreover, applications of the photonic materials featuring these dopant systems are mentioned.

1.1.4.1. *Downshifting luminescence*

In the context of this thesis, downshifting luminescence was enabled by microscale $LiYF_4$ particles (tetragonal crystalline phase) doped with various concentrations of Nd^{3+} (2.5-25%, *i.e.*, 2.5%, 5.0%, 7.5%, *etc*.) or co-doped with both Ce^{3+}(2%) and Tb^{3+}(2%). **Figure 5** (*vide infra*) depicts the energy level diagrams of both dopant systems and the respective electronic transitions that foster their downshifting luminescence. It should be noted that crystal field splitting of the $^{2S+1}L_J$ states is not indicated.

As evident from **Figure 5-A**, both excitation and emission in Nd^{3+} occur by means of 4f ↔ 4f electronic transitions. Upon absorbing 808 nm radiation,[26] an electron is promoted from the $^4I_{9/2}$ ground state of Nd^{3+} to the $^4F_{5/2}$ excited state. Then, non-radiative relaxation of the excited state populates the metastable (*i.e.*, relatively long-lived) emissive $^4F_{3/2}$ state, from which multiple radiative relaxations are possible, *e.g.*, to the $^4I_{13/2}$ (λ_{EM} – 1.32 μm), $^4I_{11/2}$ (1.06 μm), and $^4I_{9/2}$ (900 nm) states.[27,28] Because the frequency of the emission is lower than that of the excitation, the respective 4f ↔ 4f electronic transitions in Nd^{3+} exhibit classic Stokes shift luminescence, which is not entirely the case for the Ce^{3+}/Tb^{3+} co-dopant system (*vide infra*).

Because the excitation and emission frequencies associated with Nd^{3+}-meditated downshifting luminescence fall in the range of the first (650–950 nm) and second (1–1.35 μm) biological windows, *i.e.*, spectral ranges in which light has maximum penetration depth of biological tissue,[30] Nd^{3+}-based nanoscale phosphors are emerging as promising candidates for biomedical applications such as *in-vivo* NIR-NIR imaging[26] and remote-controlled nanothermometry.[28]

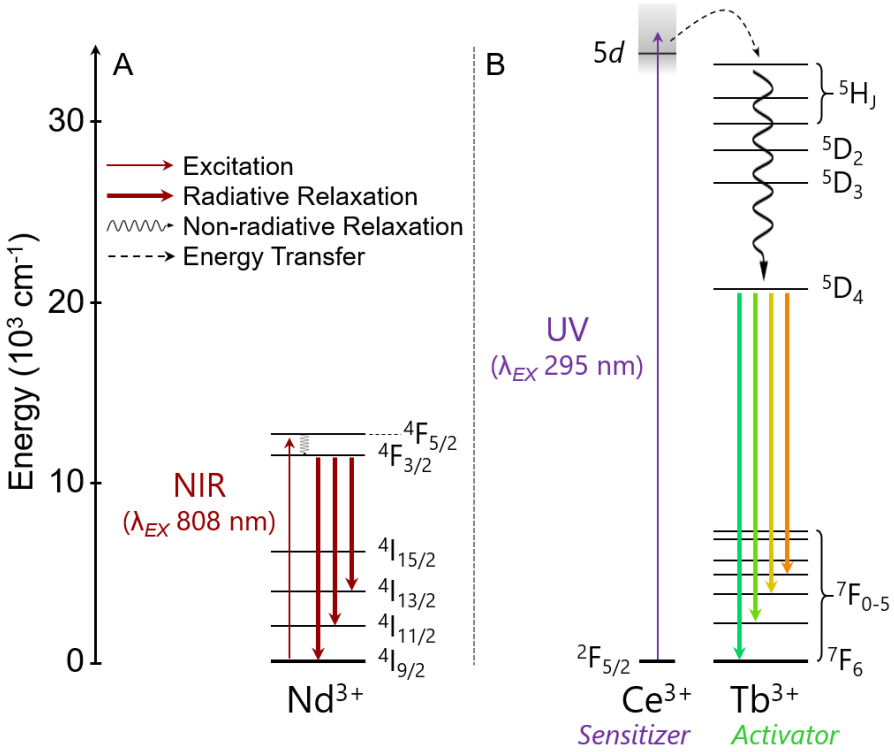

Figure 5. Energy level diagrams depicting (A) a partial $4f^n$ electronic configuration of Nd^{3+}, and (B) partial $5d^n$ and $4f^n$ configurations of Ce^{3+} and Tb^{3+}, respectively. Relevant electronic transitions are indicated. Energy of the 5d band is not to scale. Crystal field splitting of the $^{2S+1}L_J$ states is not indicated.

With respect to *in-vivo* bioimaging, the NIR excitation/NIR emission approach diminishes the extent of biological tissue auto-fluorescence, light absorption, and scattering that is otherwise prominent in UV-Vis-based bioimaging approaches.[30] Ultimately, this increases the depth at which the imaging can be accomplished while maintaining adequate spatial resolution of the respective images (*ca*. 1 cm with LaF_3:Nd^{3+}, but as deep as 3 cm has been achieved with other RE^{3+}-based phosphors).[26,31] Beyond mere bioimaging, the spectral match between Nd^{3+} excitation/emission frequencies and the NIR transparency range of biological tissue can be leveraged in addition to the thermal sensitivity[V] of its 4f ↔ 4f electronic transitions between particular Stark levels of the $^4F_{3/2}$ and $^4I_{9/2}$ manifolds.[28] *In-vivo* NIR-NIR thermal sensing of this type is highly relevant for potential biomedical applications such as early cancer diagnosis and controlled hyperthermia treatment.[28]

[V] Temperature-dependent emission band position and intensity.

In contrast to downshifting in Nd^{3+}, downshifting mediated by the Ce^{3+}/Tb^{3+} dopant pair does not qualify as Stokes shift luminescence due to the presence of an energy transfer step between the two ions.[23] Nevertheless, the process still involves emission of a single lower energy photon upon absorption of a single higher energy photon. More specifically, a Laporte-allowed 4f ($^2F_{5/2}$ ground state) ↔ 5d electronic transition in Ce^{3+} is first stimulated by a UV photon (strongest Ce^{3+} absorption in $LiYF_4$ is at *ca*. 300 nm).[32] Then, an energy transfer takes place from the excited 5d* state of Ce^{3+} to a ^5H_J state of Tb^{3+}, from which non-radiative relaxation populates the metastable emissive $^5D_4$ state.[32,33] Lastly, four characteristic Tb^{3+} radiative relaxations (4f ↔ 4f electronic transitions) take place from the excited $^5D_4$ state down to the ^7F_J (J = 3–6) manifolds (emission bands centered at 621 nm, 580 nm, 545 nm, and 490 nm, respectively).[29] In the case just described, Ce^{3+} acts as the sensitizer (donor) and Tb^{3+} as the activator (acceptor).[23] Tb^{3+} emission can be directly stimulated by UV (254 nm) excitation; however, its sensitization *via* Ce^{3+} has been proven to be much more efficient, *e.g.*, 65-fold stronger Tb^{3+} emission from $LiYF_4:Ce^{3+}/Tb^{3+}$ (λ_{EX} 300 nm) *vs*. $LiYF_4:Tb^{3+}$ (λ_{EX} 254 nm).[32]

With respect to applications, the readily UV-stimulated 4f → 5d transition in Ce^{3+} is used to sensitize green Tb^{3+} emission in fluorescent lamps, *e.g.*, commercially applied $LaPO_4:Ce^{3+}/Tb^{3+}$.[34] Furthermore, Ce^{3+} can be used to sensitize red, pink, and green/blue emission from Eu^{3+}, Sm^{3+}, and Dy^{3+}, respectively, and is thus of high relevance to the development of display technologies, for example.[29,32,35]

1.1.4.2. *Upconversion luminescence*

In the context of RE-mediated luminescence, whereas downshifting can be enabled by both 4f ↔ 4f (*e.g.*, Nd^{3+}) and 4f ↔ 5d (*e.g.*, Ce^{3+}/Tb^{3+}) electronic transitions, upconversion is limited to 4f ↔ 4f transitions when low frequency excitation radiation (NIR) is employed. Thus, because of the forbidden nature of an intraconfigurational $4f^n$ electron rearrangement, the molar absorptivity is low, whereas the lifetime of the excited states is long, *i.e.*, the probability of both photon absorption and emission is low.[36] More specifically, the typical molar absorptivity (ε) for an RE^{3+} is less than 1 $M^{-1}cm^{-1}$

vs. ca. 10^5 $M^{-1}cm^{-1}$ in organic dyes, and the typical excited state lifetime (τ) is in the μs–ms range (with the longest lifetime of *ca.* 10–20 ms being accredited to the $^4I_{13/2}$ state of Er^{3+}), whereas for an organic dye τ is less than 100 ns.[37] Hence, although upconversion luminescence can be mediated by a single RE^{3+} ion type, utilizing another RE^{3+} co-dopant with a higher molar absorptivity as the sensitizer enables higher upconversion efficiency.[23] Yb^{3+} is a particularly good sensitizer for Er^{3+}, Ho^{3+}, and Tm^{3+} due to its relatively high molar absorptivity of 980 nm radiation (ε *ca.* 10 $M^{-1}cm^{-1}$) and a good match in energy between its excited state and the ladderlike arrangement of the respective activators' energy levels (a necessary requirement for an efficient energy transfer from sensitizer to activator).[34,38] Nd^{3+} is also a good sensitizer with a relatively high molar absorptivity of *ca.* 800 nm radiation, which explains why it can be also used by itself for mediating downshifting luminescence.[37]

The two most common and efficient upconversion mechanisms are the excited state absorption (ESA) and energy transfer upconversion (ETU; **Figure 6**).

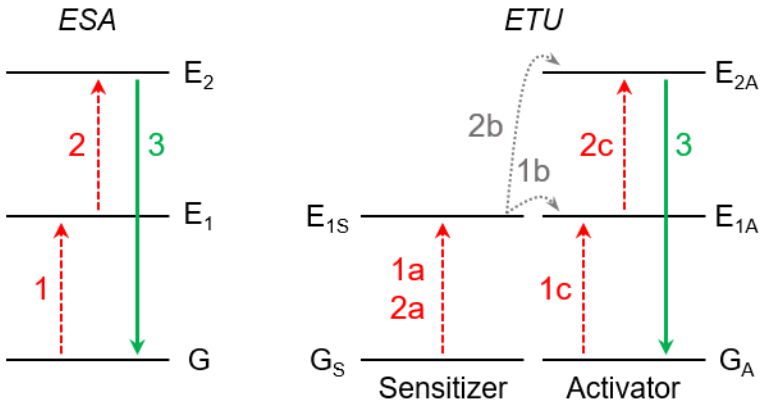

Figure 6. Excited state absorption (ESA) and energy transfer upconversion (ETU) mechanisms for upconversion luminescence. Chronological steps for both mechanisms are numbered (assuming a two-photon process). ESA – (1) absorption of a photon, (2) absorption of another photon, and (3) emission. ETU – (1a/2a) consecutive absorption of two photons, (1b/2b) primarily non-radiative energy transfer from the sensitizer to the activator, (1c/2c) excitation of the activator as a consequence of the preceding energy transfer from the sensitizer, and (3) emission. Republished (redrawn) with permission (and modified) from Upconverting Nanoparticles, M. Haase and H. Schafer, *Angew. Chemie Int. Ed.* **2011**, *50*, 5808–5829.

Upconversion in a single ion type system typically occurs *via* the ESA mechanism, in which multiple photons are consecutively absorbed, *i.e.*, the first photon promotes an

electron from the ground state (G) to the first excited state (E_1), absorption of a second photon within the lifetime period of E_1 promotes the respective electron from E_1 to E_2, and *etc*.[VI, 23] In an ETU mechanism involving a sensitizer and an activator pair (ε of sensitizer > ε of activator), the sensitizer absorbs a photon thereby promoting an electron from G_S to E_{1S}. Then, the energy is transferred from E_{1S} of the sensitizer to the activator (primarily *via* the non-radiative energy transfer process), thus promoting an electron of the activator from G_A to E_{1A}. The process of sensitizer excitation and subsequent energy transfer to the activator can repeat multiple times, increasing the energy of the activator to E_{2A} and beyond, respectively, before radiative relaxation takes place within the activator.[23,34] In fact, the ETU mechanism can repeat up to five times in the Yb^{3+}/Tm^{3+} dopant pair, resulting in the upconversion of NIR excitation (980 nm) into UV emission (290 nm).[22] Other mechanisms by which upconversion luminescence can be fostered exist, but they are outside the scope of this work.[23]

In the context of this thesis, upconversion luminescence was enabled by microscale $LiYF_4$ particles (tetragonal crystalline phase) co-doped with Yb^{3+}(18%)/Er^{3+}(2%) and Yb^{3+}(25%)/Tm^{3+}(0.5%), microscale $LiYbF_4$ particles (tetragonal crystalline phase) doped with Er^{3+}(2%), nanoscale $NaGdF_4$ particles (hexagonal crystalline phase) co-doped with Yb^{3+}(18%)/Er^{3+}(2%), and nanoscale $NaYF_4$ particles (cubic crystalline phase) co-doped with Yb^{3+}(18%)/Er^{3+}(2%). **Figure 7** (*vide infra*) depicts the energy level diagrams of both dopant systems and the respective electronic transitions that foster their upconversion luminescence *via* the ETU mechanism.[22,30]

A step-by-step description of the mechanism by which upconversion luminescence is generated by the two respective dopant systems will not be provided herein because **Figures 6** and **7**, as well as the accompanying text provide the necessary level of detail for the purpose of this discussion. However, it should be mentioned that upon excitation with 980 nm radiation, the wavelengths of the typical emission bands generated by the Yb^{3+}/Er^{3+} co-dopant system are *ca*. 410 nm ($^2H_{9/2} \rightarrow {}^4I_{15/2}$), 520 nm ($^2H_{11/2} \rightarrow {}^4I_{15/2}$), 550 nm ($^4S_{3/2} \rightarrow {}^4I_{15/2}$), and 660 nm ($^4F_{9/2} \rightarrow {}^4I_{15/2}$).[39]

[VI] The mechanism by which an electron is promoted from the ground state to the first excited state is refereed to as ground state absorption (GSA). Thus, GSA is part of the two upconversion mechanisms discussed herein (ESA and ETU).[23]

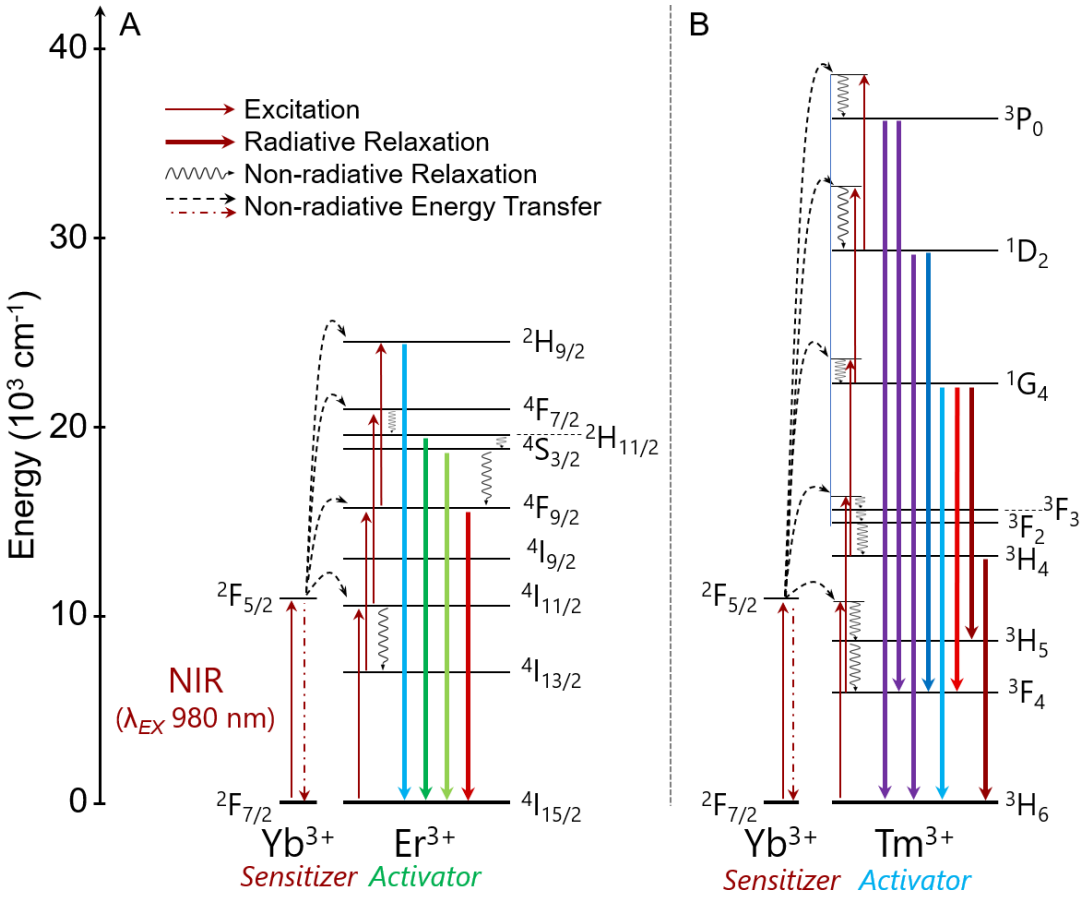

Figure 7. Energy level diagrams depicting partial $4f^n$ electronic configurations of (A) Yb^{3+} and Er^{3+}, and (B) Yb^{3+} and Tm^{3+}. Observed electronic transitions are indicated. Crystal field splitting of the $^{2S+1}L_J$ states is not indicated.

For the Yb^{3+}/Tm^{3+} co-dopant system, the wavelengths of the typical emission bands are *ca*. 290 nm ($^3P_0 \rightarrow {}^3H_6$), 350 nm ($^3P_0 \rightarrow {}^3F_4$), 370 nm ($^1D_2 \rightarrow {}^3H_6$), 455 ($^1D_2 \rightarrow {}^3F_4$), 480 nm ($^1G_4 \rightarrow {}^3H_6$), 650 nm ($^1G_4 \rightarrow {}^3F_4$), 790 nm ($^1G_4 \rightarrow {}^3H_5$), and 801 nm ($^3H_4 \rightarrow {}^3H_6$).[22]

With respect to potential and existing applications, RE-based upconverting materials – nanoparticles, in particular – exhibit exceptional variety.[40] One relatively recent, outstanding, and relevant example comes from the field of optogenetics, and involves selective stimulation of deep brain neurons in mice *via* NIR (980 nm)-induced green and blue emission stemming from Yb^{3+}/Er^{3+} and Yb^{3+}/Tm^{3+} co-doped $NaYF_4$ nanoparticles, respectively.[41] This particular study demonstrated the efficacy of upconverting nanoparticles in minimally invasive neurological disorder therapy.[41] The success of this

and other nominal examples of luminescent, RE-based materials in action is at least in part predicated on the careful consideration of the RE dopant system, the dopant concentration within the host matrix, as well as the crystalline phase and sizescale of the host material. The following sections are devoted to a brief overview of these parameters.

1.2. Optimizing RE-mediated luminescence

1.2.1. Optimal dopant concentration

As mentioned above, some RE-based photonic materials function strictly as a result of Laporte-forbidden 4f ↔ 4f electronic transitions. Although these materials present a wide range of exciting opportunities for novel functional material development, they generally suffer from relatively low luminescence efficiency.[40] This is primarily due to the low absorption probability of incident excitation radiation.[42]

It may seem intuitive that simply increasing the dopant concentration of *e.g.*, Nd^{3+} will facilitate brighter downshifting luminescence, or that increasing the relative amount of Yb^{3+}, the stronger-absorbing sensitizer in the *e.g.*, Yb^{3+} and Er^{3+} dopant pair, will facilitate brighter upconversion luminescence. However, in the context of RE-mediated luminescence, higher dopant concentration does not necessarily lead to stronger emission.[42]

In brief, increasing the dopant concentration to a certain limit does in fact compensate for the low molar absorptivity of the respective ion type, thus yielding stronger emission.[36] However, beyond the critical dopant concentration, *i.e.*, concentration that yields optimal luminescence intensity, inter-ionic non-radiative energy transfer (which leads to emission quenching at crystalline defect sites)[34] and unproductive cross-relaxation (which decreases the intensity of higher-energy emissions)[42] start dominating productive radiative relaxation, thus leading to weaker intensities of desirable emissions.[36] This is a consequence of the relatively long, RE-specific lifetimes of the excited 4f* states.[42]

In an attempt to mitigate the aforementioned "concentration quenching" effects, optimal dopant concentrations for the popular upconverting Yb^{3+}/Er^{3+} and Yb^{3+}/Tm^{3+} dopant pairs

have been established – Yb^{3+}(18–20%)/Er^{3+}(2%) and Yb^{3+}(25%)/Tm^{3+}(0.5%), respectively.[42] No such gold-standard has been established for Nd^{3+}-based systems, but a value of 15% has been proposed for nanoscale LaF_3 and 5% for nanoscale $LiYF_4$ [28,43] Doping concentrations for the Ce^{3+}/Tb^{3+} dopant pair also range quite broadly, *e.g.*, Ce^{3+}(15%)/Tb^{3+}(15%),[29,32] Ce^{3+}(7%)/Tb^{3+}(5%),[20] and Ce^{3+}(2.5%)/Tb^{3+}(2.5%),[35] but this is associated with other reasons, *i.e.*, the fact that Ce^{3+} excitation is Laporte-allowed (4f → 5d) and that the energy-transfer efficiency between Ce^{3+} and Tb^{3+} is very much dependent on the host matrix.[33]

In the context of this thesis, the optimal Yb^{3+}(18%)/Er^{3+}(2%) and Yb^{3+}(25%)/Tm^{3+}(0.5%) dopant concentrations were implemented for the upconverting systems. Ce^{3+}(2%)/Tb^{3+}(2%) was targeted simply as a proof of concept (*vide infra* **Section 4.2.1**), and a range of Nd^{3+} concentrations (2.5 – 25%, *i.e.*, 2.5%, 5.0%, 7.5%, *etc*.) was targeted primarily for the purpose of a future-perspectives project (*vide infra* **Section 5.2**).

1.2.2. Crystalline host materials for RE-mediated luminescence

In addition to concentration quenching effects described in the previous section, phonon-mediated[VII] non-radiative relaxation also contributes to the weakening of emission intensity.[42] In crystalline materials that are characterized by a low lattice phonon energy, more phonon quanta are required to quench a particular RE^{3+} excited state; hence, phonon-mediated non-radiative relaxation is less efficient in said materials.[36] Ultimately, low phonon energy host matrices facilitate Laporte-forbidden, radiative 4f → 4f relaxations from long-lived excited 4f* states by mitigating the extent of competing, non-radiative multiphonon relaxations.[42]

Fluoride-based inorganic matrices, and $M(RE)F_4$ matrices in particular, *e.g.*, $NaYF_4$, $NaGdF_4$, and $LiYF_4$, are especially suitable for hosting luminescent REs due to their relatively low phonon energies (*ca*. 350 cm^{-1}) and high chemical stability, as compared to *e.g.*, phosphates (< 1050 cm^{-1}), vanadates (< 600 cm^{-1}), and oxides (> 500^{-1} cm).[42,44] In

[VII] A phonon is a quantized unit of vibrational energy in a crystal lattice.

fact, all RE-based crystalline particles featured in this thesis belong to the $M(RE)F_4$ group, namely: tetragonal phase $Li(RE)F_4$ (RE – Y, Yb), hexagonal phase (β) $NaGdF_4$, and cubic phase (α) $NaYF_4$.

In tetragonal phase $Li(RE)F_4$, RE^{3+} dopants occupy the crystalline sites designated with the non-centrosymmetric S_4 point symmetry.[45] In β-$Na(RE)F_4$, RE^{3+} dopants are split between an all-RE^{3+} site and a site populated by both RE^{3+} and Na^+, with both sites designated with the non-centrosymmetric C_{3h} point symmetry.[46] Lastly, in α-$Na(RE)F_4$, RE^{3+} dopants occupy the only cation site equally populated by RE^{3+} and Na^{3+}.[44] In contrast to the non-centrosymmetric cation sites in tetragonal phase $Li(RE)F_4$ and β-$Na(RE)F_4$, S_4 and C_{3h}, respectively, the cation site in α-$Na(RE)F_4$ is designated with the centrosymmetric O_h point symmetry.[44] It should be noted that despite having a nominal O_h point symmetry, RE^{3+} doped into α-$Na(RE)F_4$ still exhibit luminescence due to lowering of the respective site symmetry upon lattice distortion that arises as a consequence of a size mismatch between the host and dopant ions.[44,47]

Nevertheless, between the two $NaYF_4$ polymorphs, α-$NaYF_4$ facilitates much weaker RE-mediated upconversion luminescence due to having a random distribution of Na^+ and RE^{3+} within the lattice.[48] **Figure 8** depicts all three crystalline phases involved in this work.

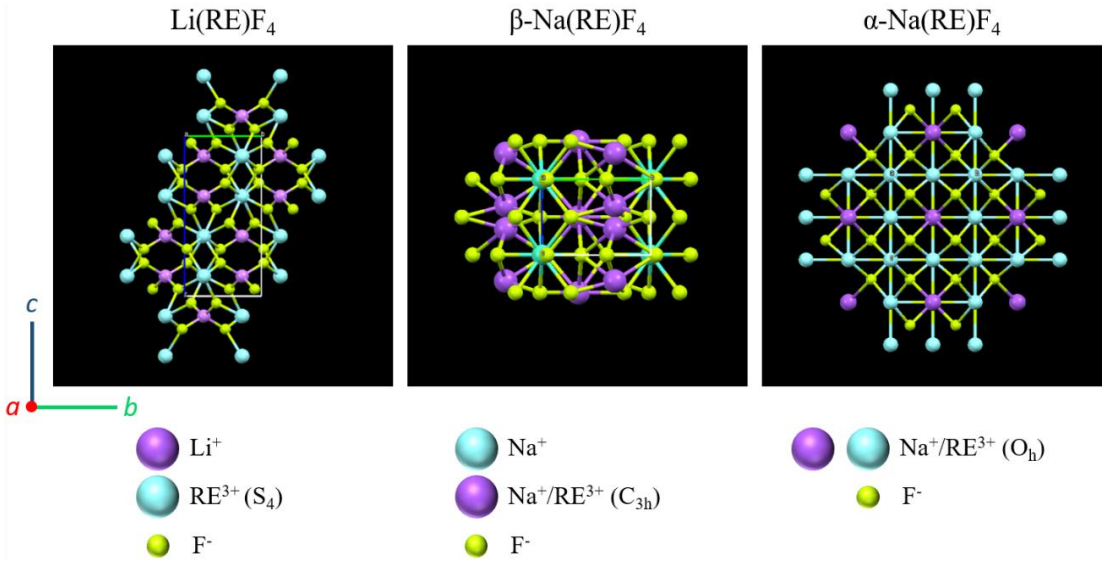

Figure 8. Crystalline structures of tetragonal phase $LiYF_4$, hexagonal phase (β) $NaYF_4$, and cubic phase (α) $NaYF_4$. Lattice parameters are oriented such that 'a' is pointing out of the page. Constituent ions are identified. Point symmetry of the RE^{3+} sites is identified. Images were generated by Mercury software.

1.2.3. Effect of particle size

There is strong evidence that quantum yield[VIII] is inversely proportional to the surface-to-volume ratio of a particle.[36,42] In fact, this relationship had been independently corroborated for $LiYF_4$ particles co-doped with both Yb^{3+}/Er^{3+} and Yb^{3+}/Tm^{3+}, as well as β-$NaYF_4$ particles co-doped with Yb^{3+}/Er^{3+}.[49–51]

The reason for this inverse relationship is two-fold. First, in addition to dopant concentration effects and phonon-mediated non-radiative relaxation discussed earlier, crystalline "defects" at the surface of a particle also foster luminescence quenching.[36] However, the nature of said surface defects has not been explicitly elucidated.[36] Second, it has been demonstrated that luminescence quenching at the particle surface is mediated *via* coupling of the excited RE^{3+} state with vibrational modes of C–H and O–H bonds contained in the particle-stabilizing organic ligands and/or the solvent in which the particles are dispersed.[49,52]

For applications where small particle size (nanoscale) is a prerequisite *e.g., in-vivo* biomedical applications, surface-induced luminescence quenching has been mitigated, and in some cases ameliorated by growing protective crystalline shells (doped or undoped) around the respective particles.[50,51] Alternatively, larger, stronger-emitting particles can be utilized if their respective size doesn't hinder their efficacy.

1.3. Specialized optical characterization techniques

1.3.1. Hyperspectral imaging

Hyperspectral imaging is a powerful optical characterization technique that simultaneously provides spatial and spectral information about an assayed sample.[53] More

[VIII] Absolute quantum yield is the ratio (expressed as a percentage) between the number of emitted photons and the number of absorbed photons. Maximum quantum yield for downshifting luminescence is 100% (one photon emitted for every one photon absorbed), for a two-photon upconversion process it is 50% (one photon emitted for every two photons absorbed; lower for three-, four-, and five-photon processes, respectively), and for downconversion luminescence it is > 100% (multiple photons emitted for every one photon absorbed).

specifically, a hyperspectral image is a three-dimensional data cube, in which the *x* and *y* axes correspond to the two-dimensional image, and the *z* axis corresponds to the wavelength range used to probe a particular optical property of a sample, *e.g.*, absorption, emission, or reflection.[53] In other words, every pixel comprising a hyperspectral image carries specific spectral information about the assayed sample.

This technique was initially implemented for the purpose of remote sensing in *e.g.*, resource exploration, but has been gaining attention in the field of nano/micromaterials as well.[53,54] However, its application toward investigating the luminescence properties of RE-based materials is still very limited.[55,56] Thus, utilizing this technique for studying the spatial distribution of upconverting luminescence generated by the microscale $LiYF_4$:RE^{3+} particles was highly opportune. More specifically, **Section 4.3.1** details how hyperspectral and SEM imaging were used in tandem to reveal a relationship between spatial particle orientation and interparticle differences in upconversion emission intensity.

1.3.2. Single-particle polarized emission spectroscopy

All crystalline materials characterized by the hexagonal, trigonal, or tetragonal crystal systems exhibit uniaxial crystalline anisotropy, *i.e.*, possess an optic axis (OA).[57] Thus, some of the constituent lattice ions (those located at crystalline sites defined by the non-centrosymmetric point groups) experience an anisotropic crystal field that varies as a function of the angle relative to the OA.[58] In the context of RE-doped crystalline materials, this means that the selection rules governing the probability of induced electric dipole and magnetic dipole 4f → 4f transitions become influenced, in part, by the polarization of the emission radiation relative to the OA of the host matrix.[59] For example, the specific selection rules for both induced electric dipole and magnetic dipole transitions between 4f configurations (defined by the specific irreducible representations Γ) in S_4 and C_{3h} point symmetries are presented in **Table 1** (*vide infra*).[59] These specific point symmetries are observed for tetragonal-phase Li(RE)F_4 and hexagonal-phase (β) Na(RE)F_4, respectively, both of which are particularly relevant host matrices in the context of RE-mediated luminescence.

Table 1. Selection rules for the induced electric dipole and magnetic dipole transitions in S_4 and C_{h3} point symmetries. Irreducible representations (Γ) of the 4f configuration term symbols ($^{2S+1}L_J$) are labeled according to the Koster notation.

	Induced electric dipole			Magnetic dipole		
S_4	Γ_1	Γ_2	$\Gamma_{3,4}$	Γ_1	Γ_2	$\Gamma_{3,4}$
Γ_1	–	π	α, σ	σ	–	α, π
Γ_2	π	–	α, σ	–	σ	α, π
$\Gamma_{3,4}$	α, σ	α, σ	π	α, π	α, π	σ

C_{3h}	Γ_1	$\Gamma_{2,3}$	Γ_4	$\Gamma_{5,6}$	Γ_1	$\Gamma_{2,3}$	Γ_4	$\Gamma_{5,6}$
Γ_1	–	α, σ	π	–	σ	–	–	α, π
$\Gamma_{2,3}$	α, σ	α, σ	–	π	–	σ	α, π	α, π
Γ_4	π	–	–	α, σ	–	α, π	σ	–
$\Gamma_{5,6}$	–	π	α, σ	α, σ	α, π	α, π	–	σ

As evident from **Table 1**, induced electric dipole transitions in S_4 and C_{3h} point symmetries can have the following polarization states: α (both electric ($\vec{E}$) and magnetic ($\vec{M}$) field vectors of the emission radiation are orthogonal with the OA), σ ($\vec{E}$ is orthogonal with the OA; $\vec{M}$ is parallel with the OA, and π ($\vec{E}$ is parallel with the OA; $\vec{M}$ is orthogonal with the OA). Of course, as with the Laporte selection rules, the polarization-dependent selection rules shown above simply reflect which polarization states will result in the highest electronic transition probability between two particular 4f Stark levels defined by the respective irreducible representations. Thus, a transition that deviates from the polarization requirements imposed by the selection rules is not impossible; rather, it is less probable.[58]

Polarized emission spectroscopy is employed to investigate the polarization-dependent emission behaviour of luminescent, uniaxial crystalline materials.[60] For example, it is rather simple to assess the difference in polarization of a particular 4f ↔ 4f emission band stemming from two β-$NaYF_4$:Yb^{3+}/Er^{3+} particles (hexagonal prism morphology) that are spatially orientated such that the OA of one particle is parallel with the substrate (S; OA ∥ S), and is perpendicular for the other (OA ⊥ S).[60] This can be accomplished by passing the emission of the separately probed particles through a linear polarizer that is positioned in various radial orientations (*e.g.*, 36 orientations for every 10° increment in the range from 0° to 350°) prior to detecting it at the monochromator (*vide infra* **Section 4.3.2** for further details).[60] Constructing two polar plots by plotting the intensity

(integrated spectral band area) of the respective emission band (or a ratio between two specific bands) as a function of the linear polarizer angle would then illustrate the radial polarization state distribution in the direction of emission propagation that was probed for each spatial particle orientation (**Figure 9**).

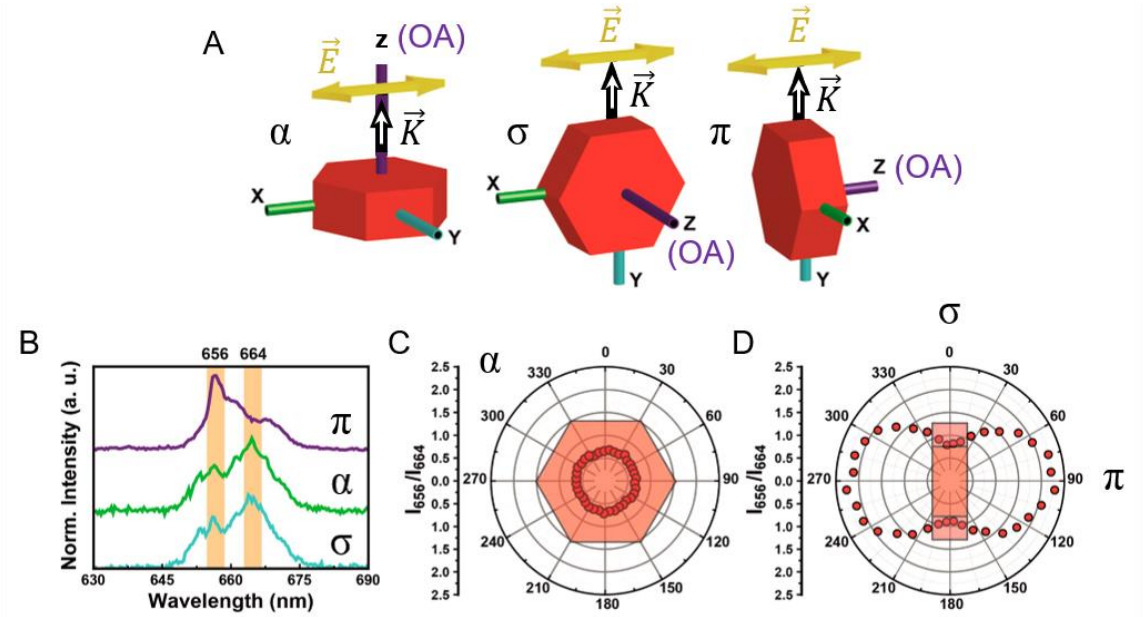

Figure 9. A) Schematic representation of the α, σ, and π polarization states relative to the optic axis (OA) of a β-$NaYF_4Yb^{3+}/Er^{3+}$ particle with hexagonal prism morphology. $\vec{E}$ is the electromagnetic field vector and $\vec{K}$ is the probed emission direction vector. B) Respective luminescence spectra obtained for the three particle orientations. C) Polar plot depicting the ratio between the 656 nm and 664 nm spectral bands as a function of the linear polarizer angle for the α polarization state. D) Polar plot depicting the ratio between the 656 nm and 664 nm spectral bands as a function of the linear polarizer angle for the σ, π, and intermediate polarization states. Reprinted (adapted) with permission from Rodríguez-Sevilla, P. *et al.*, Optical Torques on Upconverting Particles for Intracellular Microrheometry, *Nano Lett.* **2016**, *16*, 8005–8014. Copyright 2014 American Chemical Society.

In such an experiment, probing the emission stemming parallel to the OA (α polarization) of one of the β-$NaYF_4$:Yb^{3+}/Er^{3+} particles (OA $\perp$ S) would yield a circular polar plot, because emission is not polarized along this direction (**Figure 9-C**).[60,61] Conversely, emission stemming perpendicular to the optic axis of the other β-$NaYF_4$:Yb^{3+}/Er^{3+} particle (OA $\parallel$ S) would exhibit a polarization state change as a function of the linear polarizer angle, because the orientation of the associated electric field vector can be perpendicular ($\vec{E}$ $\perp$ OA; σ polarization state), parallel ($\vec{E}$ $\parallel$ OA;

π polarization state), or oblique (composed of both $\vec{E} \perp$ OA and $\vec{E} \parallel$ OA vector components) to the OA in this direction, *i.e.*, the respective polar plot would depict a figure "8" (**Figure 9-D**).[60,61] Ultimately, these observations would arise as a consequence of the specific selection rules that govern the probability of the respective emission in the two directions being probed.

However, if was the case that the β-$NaYF_4$ particles exhibited either a long rod or a very narrow-width disk morphology, the most prominent (if not the only) spatial particle orientation would be such that OA $\parallel$ S for the long rods and OA $\perp$ S for the disks. In either case, conducting a thorough single-particle polarized emission spectroscopy study on a dry sample would be impossible, since more than one spatial particle orientation is required to assess the change in polarized emission behavior as a function of emission direction relative to the OA. The same problem would arise for any uniaxial crystalline material whose particles are characterized by a morphology that yields one distinct spatial particle orientation in a monolayer of a dry sample, *e.g.*, square-based bipyramidal $LiYF_4$ microparticles. In this regard, optical trapping can be of very high utility.

Developed by A. Ashkin and colleagues of the Bell Laboratories in 1986, optical trapping is a technique that allows for three-dimensional manipulation of atoms, nano- and microscale dielectric particles, and even biologic systems such as bacteria, viruses, and whole cells.[IX, 62,63] This technique is enabled by the interaction of scattering and gradient forces produced by a highly-focused laser beam on a dielectric particle located near or inside the focal point of the laser.[63] The scattering force (F_{Scat}) points in the direction of laser propagation, whereas the gradient force (F_{Grad}) points in the direction of its intensity gradient, *i.e.*, the focal point.[63] A particle can be trapped inside the laser focus when $F_{Grad} \gg F_{Scat}$, a condition that is dependent on experimental variables such as: particle size and geometry, difference in the refractive indices between the particle and the surrounding medium, power and frequency of the laser radiation, and numerical aperture of the objective used to focus the laser.[64] For further insight into this topic, a review by P. Rodriguez-Sevilla *et al*. is recommended.[64]

IX At the age of 96, Arthur Ashkin was awarded the 2018 Nobel Prize in Physics for his work on optical trapping![127]

The Fluorescence Imaging Group of the Universidad Autónoma de Madrid has been actively leveraging optical trapping in the context of RE-based nano/microscale materials.[65–68] Some of their work explicitly deals with utilizing optical trapping for the purpose of conducing single-particle polarized spectroscopy studies. In particular, they demonstrated that the β-$NaYF_4$ particle morphology-related problem described earlier can be circumvented by manipulating the spatial orientation of both β-$NaYF_4$ nanorods (aspect ratio (AR) of *ca*. 8)[69] and submicron-scale disks (AR = 0.5)[60] inside an optical trap in a manner that grants access to both extreme spatial particle orientations (with respect to the OA orientation), *i.e.*, OA ∥ S and OA ⊥ S, for each particle morphology. In the context of this thesis, the same approach was utilized to investigate the change in polarized emission behaviour as a function of emission direction relative to the OA of the Yb^{3+}/Er^{3+} co-doped square-based bipyramidal $LiYF_4$ microparticles. In fact, this study was conduced in collaboration with the Fluorescence Imaging Group (*vide infra* **Section 4.3.2**).

1.4. Synthesis of M(RE)F_4 nano/microparticles

1.4.1. Traditional synthesis routes

A variety of synthesis approaches toward RE-doped nano- and microscale materials have been developed, *e.g.*, co-precipitation, sol-gel, hydro/solvothermal, and thermal decomposition synthesis.[70] In the context of M(RE)F_4-based luminescent materials, thermal decomposition of M^+-/RE^{3+}-trifluoroacetate precursors in high boiling point solvents is most often employed for the synthesis of nanoparticles,[71] whereas microscale particles are typically targeted *via* hydro/solvothermal syntheses utilizing (sub-)supercritical aqueous and/or polar organic solvents,[72] as well as $RECl_3$/$RENO_3$, MF/MOH, and NH_4F precursors as the source of RE^{3+}, M^+, and F^-, respectively.[71]

In both cases, particle growth occurs *via* the LaMer mechanism.[72] In brief, an increase in temperature facilitates the solubilization of the (*in-situ*-formed) inorganic precursors during the course of the reaction. Reactant concentration increases until the critical limit of supersaturation is reached, at which point rapid nucleation occurs. Particle nucleation

results in a sudden decrease in reactant concentration, which halts further nucleation. Subsequently, remaining solubilized precursors contribute toward particle growth. Duration of the particle nucleation phase greatly influences particle size distribution, whereas the duration of the particle growth phase affects particle size.[72] Thus, the temporal temperature profile of the reaction exhibits significant influence over the size and degree of monodispersity of the final product.

Both methods also employ ligands/solvents featuring a (partial) negative charge that (selectively) binds to the surface RE^{3+} of the particle nuclei, thereby coordinating their subsequent growth and morphological development.[36,70,73] The thermal decomposition route employs octadecene as the high boiling point solvent and a mixture of oleylamine and oleic acid as coordinating ligands.[36] The hydro/solvothermal routes employ solvents such as water and ethanol, and water-soluble coordinating ligands such as ethylenediaminetetraacetic acid, citrate, acetate, and oleic acid.[70] high boiling point polyols (*e.g.*, (di)ethylene glycol and glycerol) are also used as both solvents and coordinating ligands in hydro/solvothermal syntheses.[70]

In general, many parameters affect the crystalline phase, size, and morphology of the final product.[36,71,74,75] In addition to reaction temperature/duration and solvent/ligand type, other key reaction parameters include the stoichiometric M^{+}:RE^{3+}:F^{-} ratios and the concentration of the respective reagents, the concentration of the coordinating ligand and the reaction mixture pH, and of course the physicochemical properties of all the reagents (*e.g.*, solubility, ionic radius and polarizability), coordinating ligand(s) (*e.g.*, pKa, miscibility in solvent), and solvent system (*e.g.*, boiling point). Seminal works such as those by H.-X. Mai *et al*.[74] and F. Wang *et al*.[75] consider the aforementioned parameters in the context of thermodynamics and kinetics, and outline systematic approaches toward the development of rational $M(RE)F_4$ synthesis routes.

1.4.2. Microwave-assisted synthesis

Traditionally, thermal energy is supplied *via* convectional heating for both thermal decomposition and hydro/solvothermal synthesis, *i.e.*, synthesis is performed in an oil bath or a high-pressure autoclave, respectively.[74,76] Because convectional heating is relatively

inefficient, total synthesis duration for the thermal decomposition route is *ca*. 2 h, and ≥ 12 h for the hydro/solvothermal synthesis.[74,76,77] For this reason, rapid microwave-assisted synthesis is emerging as an intriguing alternative to both approaches.[77]

Microwave irradiation fosters rapid and uniform internal heating of the reaction mixture,[78] which results in significantly shorter reaction durations (minutes *vs*. hours) in comparison to those associated with the convectional heating approaches.[77,78] Furthermore, under the appropriate physicochemical reaction conditions, microwave-induced heating can shorten the duration of the particle nucleation phase, thus allowing for the synthesis of highly monodisperse particles.[77–79] Precise computer control and real-time monitoring of reaction parameters such as irradiation power, reaction temperature, and pressure also aid in this regard.[77]

For the sake of brevity, the specific mechanisms of microwave-induced heating will not be discussed herein, but a review by M. Baghbanzadeh *et al*. is recommended.[73] It is only worth mentioning that the energy supplied by the microwave reactors (ν = 2.45 GHz; λ = 12.45 cm) is too low to directly break chemical bonds or even to induce Brownian motion of molecules and ions.[77,78] Rather, the associated electromagnetic field oscillation induces rotational motion of dipolar and/or charged molecules/ions, which causes friction.[77] Ultimately, this friction generates heat, which then induces chemical change.

The ability of a specific material (*e.g.*, solvent or reagent) to absorb microwave energy and to convert it to heat depends on its dielectric constant (susceptibility to polarization by the electric field) and dielectric loss (microwave radiation-to-heat conversion efficiency).[77] Thus, all chemical species comprising a reaction mixture differ, at least slightly, in their microwave absorbance.[77] As a result, chemical processes such as precursor dissolution and subsequent particle nucleation may differ between microwave-assisted synthesis and traditional synthesis reliant on convectional heating.[77] Ultimately, although microwave-assisted approaches can provide much faster access to state-of-the-art inorganic nano- and microscale materials, fundamental principles governing their synthesis have not been made explicit.[73] Future technological advancements that allow for systematic, *in-situ* investigation of nanoparticle formation under microwave irradiation will aid in the development of even more efficient syntheses.[77]

Chapter 2. Objectives (and *why* microscale $LiYF_4$?)

As mentioned in the introduction, $M(RE)F_4$-based crystalline materials featuring RE-mediated luminescence such as upconversion and downshifting have emerged as promising candidates for a broad range of applications. However, Na-based systems currently have the spotlight, both with respect to the number of available synthesis approaches (including the popularized microwave-assisted synthesis) and the number of envisaged applications, despite the fact that their Li-based analogues present comparable, or at times even better optical performance. More specifically, $LiYF_4$ is a particularly suitable host matrix for the upconverting Yb^{3+}/Tm^{3+} dopant pair, because it facilitates a broad spectrum of well-resolved emission bands from the deep UV (294 nm) to NIR (800 nm), and enables stronger blue and UV emission from Tm^{3+} than both $NaYF_4$ polymorphs.[22,80,81] In the context of downshifting luminescence, Nd^{3+} doped $LiYF_4$ single crystals have been long known for enabling good lasing,[82] and $LiYF_4$ has been also used to host the UV-downshifting dopant pair Ce^{3+}/Tb^{3+}.[32]

It was discussed in the introduction that irrespective of the dopant system, emission intensity can be enhanced on the microscale, since the lower surface-to-volume ratio associated with larger particles mitigates emission quenching at the surface.[49–51,83] Larger $LiYF_4:RE^{3+}$ particles would be therefore advantageous with respect to emission intensity when envisaging applications for which "nano" is not a prerequisite. However, today, such applications, *e.g.* temperature sensing,[67,84] photocatalysis,[85] and anticounterfeiting,[86] are almost exclusively dominated by the more thoroughly explored $Na(RE)F_4$ microscale systems. Furthermore, quite some attention has been recently devoted to studying polarized emission stemming from β-$NaYF_4$ nano- and microscale particles suspended inside an optical trap.[67,69] No such study yet exists for the $LiYF_4$ system (not including the one reported in this thesis), and only one case of optical trapping of a $LiYF_4$ particle has been reported to my knowledge.[87]

With respect to the emerging microwave-assisted synthesis, indeed, a vast majority of the reported synthesis routes target $Na(RE)F_4$ systems.[88–94] In fact, a microwave-assisted solvothermal synthesis (utilizing M^+-/RE^{3+}-trifluoroacetate precursors and high boiling point solvents) of nanoscale $LiYF_4$ has been only reported once,[95] and no reports of

microscale $LiYF_4$ being accessed *via* any microwave-assisted synthesis approach existed at the time of our publication (to the best of my knowledge). However, a microwave-assisted hydrothermal synthesis of submicron-scale $LiYF_4:RE^{3+}$ particles was recently reported, but no insight into the particle formation mechanism was provided.[96]

Consequently, the development of a rapid microwave-assisted synthesis method that grants controlled access to a range of $LiYF_4:RE^{3+}$ microscale systems was the first overarching objective of this thesis. The second overarching objective was to gain greater insight into the optical behaviour of the attained $LiYF_4:RE^{3+}$ microparticles at a single-particle level, with the intention that that will facilitate their future application as remote controlled microdrills and as single-particle NIR photon detectors (*vide infra* **Section 5.2**). The specific objectives for this thesis were as follows:

1. Develop a rapid microwave-assisted solvothermal synthesis route toward luminescent $LiYF_4$ microparticles featuring various RE^{3+} dopant systems, specifically: $LiYF_4:Yb^{3+}(18\%)/Er^{3+}(2\%)$ and $LiYF_4:Yb^{3+}(25\%)/Tm^{3+}(0.5\%)$ microparticles for upconversion luminescence, as well as $LiYF_4:Ce^{3+}(2\%)/Tb^{3+}(2\%)$ and $LiYF_4:Nd^{3+}(2.5\text{-}25\%)$ microparticles for downshifted luminescence.

2. Extend the microwave-assisted approach toward other luminescent $M(RE)F_4$ systems, specifically: $LiYbF_4:Er^{3+}(2\%)$, $NaYF_4:Yb^{3+}(18\%)/Er^{3+}(2\%)$, and $NaGdF_4:Yb^{3+}(18\%)/Er^{3+}(18\%)$.

3. Perform a general luminescence characterization of the attained $M(RE)F_4$ materials.

4. Conduct a more thorough luminescence characterization of the $LiYF_4:RE^{3+}$ microparticles *via* hyperspectral imaging and polarized-emission spectroscopy at a single-particle level.

5. Investigate the behaviour of $LiYF_4:RE^{3+}$ microparticles inside an optical trap.

Chapter 3. Microwave-assisted solvothermal synthesis of the RE^{3+}-doped (RE^{3+}: Yb^{3+}/Tm^{3+}, Yb^{3+}/Er^{3+}, Ce^{3+}/Tb^{3+}, and Nd^{3+}) $LiYF_4$ and Er^{3+}-doped $LiYbF_4$ microparticles, as well as the Yb^{3+}/Er^{3+}-doped $Na(RE)F_4$ (RE: Y, Gd) nanoparticles

3.0. Introduction

Synthesis of $LiYF_4$-based phosphors has been predominately limited to thermal decomposition and high-pressure solvothermal approaches employing convectional heating and solvent systems consisting entirely or partially of high boiling point solvents, *e.g.*, 1-octadecene, oleic acid, oleylamine.[22,49,97–100] However, a few hydrothermal (*i.e.*, solvothermal, but utilizing water as the solvent) methods targeting these materials have also been reported.[76,101] Albeit characterized by relatively short reaction durations (*ca.* 2 h), a potential drawback of the thermal decomposition routes lays in the fact that obtained particles undergo an *in-situ* surface functionalization with hydrophobic oleate groups. Solvothermal reactions in high-pressure autoclaves that also employ high boiling point solvents and non-water-dispersible ligands also encounter this issue, with an additional disadvantage of requiring long reaction durations (≥ 12 h). For both approaches, a subsequent surface modification step is thus often times required to render the particles water-dispersible, *e.g.*, for applications in biological milieu.[102] While this post-synthesis treatment of particles is circumvented by the high-pressure hydrothermal approaches utilizing aqueous solvent systems and water-dispersible ligands, these approaches also suffer from long reaction durations (≥ 12 h).[76,103] Consequently, there is a demand for the development of innovative routes toward $LiYF_4$ that implement the benefits of the aforementioned approaches and negate their undesirable qualities.

This chapter details the development of a microwave-assisted solvothermal synthesis approach toward microscale $LiYF_4$:RE^{3+}. The salient characteristics of the approach are the drastic reduction in reaction duration (as short as 2 min *vs.* ≥ 12 h), the utilization of a more environmentally benign solvent system (water and ethanol; no high boiling point solvents), and the *in-situ* particle surface functionalization with hydrophilic moieties.[92,104,105]

The development of a microwave-assisted solvothermal approach toward $LiYF_4$:RE^{3+} was accomplished by optimizing a set of important physicochemical reaction parameters: Li^+:RE^{3+} ion ratio, reaction mixture pH, reaction temperature/duration profile, and reaction mixture volume. This chapter details this optimization process and its subsequent application toward the synthesis of $LiYF_4$ microparticles featuring the Yb^{3+}(18%)/Er^{3+}(2%) and Yb^{3+}(25%)/Tm^{3+}(0.5%) dopant systems for upconversion as well as the Ce^{3+}(2%)/Tb^{3+}(2%) and Nd^{3+}(2.5-25%; 2.5%, 5.0%, 7.5%, *etc*.) dopant systems for downshifting luminescence. The mechanism by which $LiYF_4$ microparticles form is also unveiled, and versatility of the approach is highlighted by showcasing how it can be extended beyond $LiYF_4$-based systems, namely toward the synthesis of RE^{3+}-doped $LiYbF_4$ microparticles, β-$NaGdF_4$ and α-$NaYF_4$ nanoparticles. Lastly, a section of this chapter is dedicated to a critical review of potential challenges associated with microwave-assisted synthesis and how they can be mitigated.

3.1. Experimental details

3.1.1. Chemicals

Y_2O_3 (99.999%), Gd_2O_3 (99.999%), Yb_2O_3 (99.998%), Er_2O_3 (99.99%), Tm_2O_3 (99.997%), Nd_2O_3 (99.999%) and $LiOH{\cdot}H_2O$ (98%) were purchased from Alfa Aesar (Ward Hill, USA). $TbCl_3{\cdot}6H_2O$ (99.9%) was purchased form Strem Chemicals Inc. (Newburyport, USA). $CeCl_3{\cdot}7H_2O$ (99.9%), NH_4F (≥ 98%) and NH_4OH (28.0-30.0% NH_3 basis), oleylamine (70%), and oleic acid (90%) were purchased from Sigma Aldrich GmbH (Steinheim, Germany). HCl (36.5-38.0%), glacial acetic acid (AcOH, 99.7%), and bench-grade NaOH were purchased from Fisherbrand (USA). Ethanol (99%) was purchased from Commercial Alcohols (Brampton, Canada). All chemicals were used as received.

3.1.2. Generic procedure for the synthesis of M(RE)F_4 nano/microparticles

A complete overview of all physicochemical reaction parameters (M^+:RE^{3+}, initial reaction mixture pH, reaction temperature and duration, and reaction mixture volume) subjected to investigation and the resulting products is provided in **Table 5** of **Section 3.5**. What follows is a description of the two successful microwave-assisted synthesis routes toward RE^{3+}-doped M(RE)F_4 nano/microparticles.

For a typical synthesis of a particular RE^{3+}-doped (RE – Ce, Nd, Gd, Tb, Er, Tm, and Yb) M(RE)F_4 material (M – Li or Na; RE – Y, Gd, or Yb), 1.0 mmol of a specific $RECl_3$ precursor mixture was prepared by dissolving a total of 0.5 mmol of the corresponding RE_2O_3 constituents in a mixture of concentrated HCl (3 mL) and H_2O (2 mL) at 90 °C (**Equation 1**).[106]

Eq. 1

$$RE_2O_3 + 6HCl \xrightarrow[90\ ^\circ C]{H_2O} 2RECl_3 + 3H_2O$$

An example of how to determine the molar and weight quantities of the initial RE_2O_3 precursor when targeting a particular RE^{3+}-doped M(RE)F_4 material is provided in **Table 2**.

Table 2. Molar and weight quantities of the RE_2O_3 precursors and the resulting molar quantities of the $RECl_3$ precursors used to target an M(RE)F_4 material (*e.g.*, $LiYF_4$) with a specific RE^{3+}-doping rate (*e.g.*, 18% Yb^{3+} and 2% Er^{3+}).

RE_2O_3 (mmol) and (*mg*)	**$RECl_3$ (mmol)**	**RE^{3+} (%)**
Y_2O_3 – (0.4), (*90.3*)	YCl_3 – 0.8	Y^{3+} – 80
Yb_2O_3 – (0.09), (*35.5*)	$YbCl_3$ – 0.18	Yb^{3+} – 18
Er_2O_3 – (0.01), (*3.8*)	$ErCl_3$ – 0.02	Er^{3+} – 2
Total RE_2O_3 – 0.5 mmol	Total $RECl_3$ – 1.0 mmol	Total RE^{3+} – 100%

After complete dissolution of RE_2O_3, the HCl/H_2O mixture was evaporated at 100 °C to obtain a dry white powder of $RECl_3$.[X] Subsequently, a mixture was prepared by

[X] $RECl_3$ reagents are hydroscopic, and it is thus difficult to prepare $RECl_3$ precursor mixtures with exact-known quantities of the RE^{3+} constituents by weighing out commercially available $RECl_3$ reagents. Because obtaining the correct ratio between RE^{3+} constituents in a given M(RE)F_4-based material is of vital importance to its optical performance, non-hydroscopic RE_2O_3 reagents are typically used to prepare the corresponding inhouse $RECl_3$ mixtures. As the only exception to this precaution, purchased $CeCl_3$ and $TbCl_3$ were used directly for the synthesis of $LiYF_4$:Ce^{3+}(2%)/Tb^{3+}(2%) in this project.

combining and vortexing, in the specified order of reagents, 4.3 mmol (180.4 mg) of $LiOH \cdot H_2O$ for $Li(RE)F_4$-based systems or 4.3 mmol (172.0 mg) of NaOH for $Na(RE)F_4$-based systems, 2 mL of deionized H_2O, 2 mL of AcOH, 8 mL of ethanol, and 4.0 mmol (148.2 mg) of NH_4F. The intrinsic pH of the resulting mixture was 5.3.[XI]

The resulting opaque mixture was then added to the dry $RECl_3$ salts, and the new mixture was vigorously stirred at room temperature for approximately 10 min. A particular volume (method №1 – 11 mL; method №2 – 2 mL) of this final reaction mixture was transferred to a 35 mL glass microwave reaction vessel and the vessel was capped. The vessel was then inserted into a CEM Discover SP microwave reactor. All RE^{3+}-doped $M(RE)F_4$ nano/microparticles were grown by subjecting the reaction mixture under constant stirring (low stirring rate) to a dynamic heating profile characterized by three distinct stages: *i*) rapid ramping to target temperature (method №1 – 210 °C, method №2 – 185 °C),[XII] *ii*) rapid cooling to a particular temperature followed by static heating at the same temperature (method №1 – 200 °C for 10 min, method №2 – 180 °C for 2 min), and *iii*) gradual cooling to 50 °C. Static heating duration of method №2 was subject to variation (*vide infra* **Table 3** for details).

The respective chemical equation is presented below (**Equation 2**).

$$RECl_3 + 4.3MOH + 4NH_4F \xrightarrow[\substack{\text{Method №1 – 11 mL, 200 °C, 10 min}\\ \text{Method №2 – 2 mL, 180 °C, 2 min}}]{\substack{H_2O:AcOH:EtOH\\ 1:1:4}} M(RE)F_4 + 3.3MOH + 3NH_4Cl + NH_4OH$$

Eq. 2

Following reaction completion, the obtained particle dispersion was transferred to a centrifuge tube, diluted to 25 mL with ethanol and centrifuged (Allegra X-30R, Beckman Coulter) for 2 min at 3,000 rpm (average RCF = 625) when working-up $Li(RE)F_4$-based microparticles and 5 min at 3,000 rpm when working-up $Na(RE)F_4$-based nanoparticles (a longer or a more vigorous centrifugation is required to separate nanoscale particles from

XI For syntheses involved in the pH-study, the pH of this mixture was adjusted to 2.0 and 7.5 with HCl and NH_4OH, respectively. HCl and NH_4OH were intentionally chosen to reduce the risk of undesired phase formation, since their ionic constituents (Cl^-, NH_4^+ and OH^-) also stem from other precursors ($RECl_3$, NH_4F and Li/NaOH) and are thus common to all reaction mixtures reported herein.

XII Setpoint temperatures of the first (ramping) heating stage were 10 °C (210 °C) and 5 °C (185 °C) higher than the setpoint temperatures (200 and 180 °C) of the second (static) heating stage of the dynamic heating methods developed for methods №1 and 2, respectively. This ensured a faster ramping toward a setpoint temperature of the static heating stage.

the solution). The supernatant liquid was decanted and the remaining white particle pellet was washed twice by means of re-dispersion in a 35 mL 3:7 v/v H_2O:ethanol mixture and subsequent centrifugation. Lastly, the washed product was re-dispersed in 7 mL of ethanol for storage.

Table 3 specifies what materials were obtained *via* the two microwave-assisted solvothermal methods developed and discussed herein.

Table 3. List of all $M(RE)F_4:RE^{3+}$ materials synthesized for the purpose of this thesis and the reaction method by which they were obtained. Reaction conditions for method №1 are: $Li^+:RE^{3+}$ 4.3, pH 5.3, 11 mL, 210 °C (1 s)/200 °C (10 min), and an unknown microwave reactor infrared camera temperature sensor (MRICTS) calibration slope. Reaction conditions for method №2 are: $Li^+:RE^{3+}$ 4.3, pH 5.3, 2 mL, 185 °C (1 s)/180 °C (2 min), and a MRICTS calibration slope of 1.7107. Both methods involved a solvent system composed of H_2O:AcOH:EtOH – 1:1:4 v/v.

Method	Material
№1	$LiYF_4:Yb^{3+}$(18%), Er^{3+}(2%)
	$LiYF_4:Yb^{3+}$(25%), Tm^{3+}(0.5%)
	$LiYF_4:Ce^{3+}$(2%), Tb^{3+}(2%)
	$LiYbF_4$:Er(2%)
	α-$NaYF_4:Yb^{3+}$(18%), Er^{3+}(2%)
	β-$NaGdF_4:Yb^{3+}$(18%), Er^{3+}(2%)
№2	$LiYF_4:Yb^{3+}$(18%), Er^{3+}(2%)
	$LiYF_4:Yb^{3+}$(25%), Tm^{3+}(0.5%)
	$LiYF_4:Nd^{3+}$(2.5%)
	$LiYF_4:Nd^{3+}$(5%)
	$LiYF_4:Nd^{3+}$(7.5%)
	$LiYF_4:Nd^{3+}$(10%)
	$LiYF_4:Nd^{3+}$(12.5%)
	$LiYF_4:Nd^{3+}$(15%)
	$LiYF_4:Nd^{3+}$(17.5%)
	$LiYF_4:Nd^{3+}$(20%)
	$LiYF_4:Nd^{3+}$(22.5%)
	$LiYF_4:Nd^{3+}$(25%)

3.1.3. Microwave infrared temperature sensor calibration

For the synthesis of $LiYF_4:RE^{3+}$ microparticles *via* method №1 ($Li^+:RE^{3+}$ 4.3, pH 5.3, 11 mL, 200 °C, 10 min), the microwave infrared temperature sensor was calibrated at

130 °C by an external thermocouple. The calibration slope is unknown. Ethylene glycol was used as the temperature calibration medium.

For the synthesis of $LiYF_4$:RE^{3+} microparticles *via* method №2 (Li^+:RE^{3+} 4.3, pH 5.3, 2 mL, 180 °C, 2 min), the microwave infrared temperature sensor was re-calibrated at 230 °C by an external thermocouple. A calibration slope of 1.7107 was obtained. A 50:50 v/v mixture of oleylamine and oleic acid was used as the temperature calibration medium.

Despite the nominal temperature setting of Method №1 being 200 °C, the true temperature was lower than 180 °C as a result of an improper calibration strategy (the one described for Method №1 herein). Proper calibration of the microwave infrared temperature sensor is important as it makes known the true temperature conditions inside the reaction vessel. To achieve the highest degree of resemblance between the nominal temperature settings and the true temperature inside the reaction vessel, the infrared temperature sensor of the CEM Discover SP microwave reactor should be calibrated at the temperature value that is required by a particular synthesis. Please refer to **Section 3.4** and the user's manual of the CEM Discover SP microwave reactor for more details.

3.2. Characterization techniques

3.2.1. Characterization of physicochemical material properties

The crystalline phase of the samples was determined by powder X-ray diffraction (XRD) with a Rigaku Ultima IV diffractometer (Cu K_α, λ = 1.5401 Å). For XRD characterization, samples were prepared by drop-casting (and drying) concentrated particle dispersions (opaque; exact concentration is unknown) in ethanol onto glass slides (*ca*. 1 cm^2). For the microscale Li(RE)F_4 systems, this resulted in a white particle film, whereas a translucent particle film was obtained when drop-casting Na(RE)F_4 nanoparticles. A typical range of 15–65 °2θ (sampling width = 0.02 °2θ; scan rate = 4.0 °2θ/min) was employed when obtaining diffraction patterns for the Li(RE)F_4 systems, and a range of 15–70 °2θ (sampling width = 0.02 °2θ; scan rate = 2.0 °2θ) was

employed when obtaining diffraction patterns for the Na(RE)F_4 systems. Maud software was used to simulate a diffraction pattern presented in **Section 3.3.3**.[107]

The morphology and size distribution of the obtained materials were investigated by transmission electron microscopy (TEM, FEI Tecnai^{TM} Spirit) and scanning electron microscopy (SEM, JEOL JSM-7500F FESEM). For TEM observations, samples were dispersed on a formvar/carbon film supported on a 300-mesh copper grid. For characterization by SEM, Li(RE)F_4 microparticles were drop-casted onto a glass slide and sputtered with gold (2 nm Au layer thickness) in a vacuum coater (Leica EM ACE200). For Fourier transform infrared (FTIR) spectroscopy, dried samples were mixed with potassium bromide (KBr, FTIR grade, Alfa Aesar, Ward Hill, USA) and pressed into pellets. Spectra on the respective pellets were recorded using a Shimadzu FTIR-8200S spectrometer. Spectroscopic characterization techniques are discussed in **Section 4.1**.

3.2.2. Size analysis of M(RE)F_4 nano/microparticles

By employing the ImageJ software, SEM and TEM micrographs were used to perform statistical size distribution analysis of all herein presented M(RE)F_4 materials. The diameter of α-$NaYF_4$:RE^{3+} spherical nanoparticles was determined by measuring the two-dimensional cross section of individual nanoparticles from TEM micrographs. Length and width of β-$NaGdF_4$:RE^{3+} nanoparticles with hexagonal prism morphology were also directly determined from TEM micrographs. However, direct height and width measurements of the Li(RE)F_4:RE^{3+} square-based bipyramidal microparticles (measured vertex to vertex in both cases) was impossible due to their orientation in space. Thus, their height and width dimensions were determined by first measuring the dimensions of the triangular facets that are oriented parallel to the substrate (glass slide or carbon film) and then applying the Pythagorean theorem as demonstrated below in **Figure 10** (*vide infra*).

Ideally, SEM micrographs were used for obtaining accurate measurements of the triangular facets (**Figure 10-A**). However, dimensions of $LiYF_4$:Yb^{3+}/Er^{3+} microparticles synthesized *via* method №2 had to be measured from TEM micrographs, which involved inferring the position of the triangular facet contours (**Figure 10-B**).

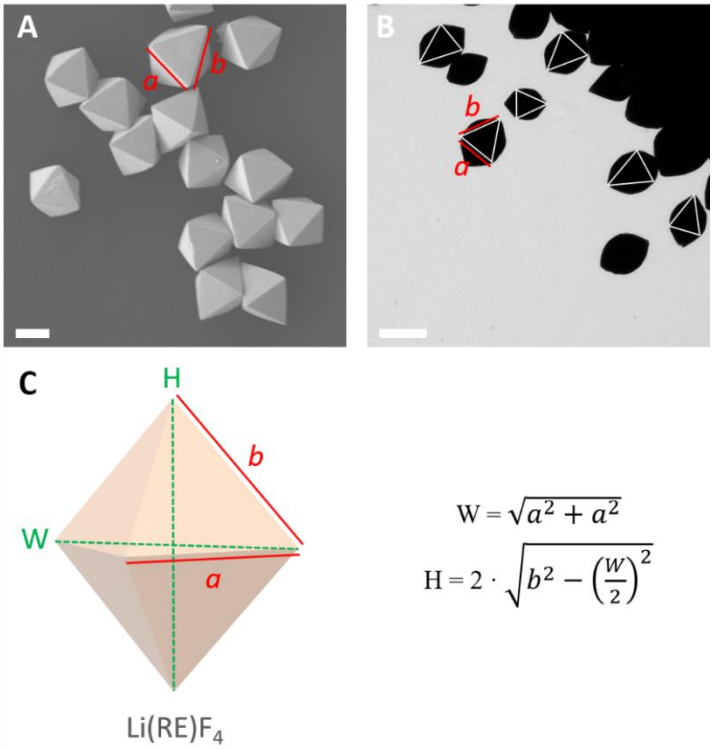

Figure 10. SEM (A) and TEM (B) micrographs of $LiYF_4$:Yb^{3+}(18%)/Er^{3+}(2%) microparticles obtained via methods №1 and №2, respectively. Lengths of the substrate-parallel triangular facet contours are indicated by '*a*' and '*b*'. Scale bars: 2 μm. C) Values for '*a*' and '*b*' are used to determine the height (H) and width (W) of the Li(RE)F_4:RE^{3+} square-base bipyramidal microparticles *via* the Pythagorean theorem.

In the latter case, only 26 microparticles were used for size distribution analysis. However, for all other M(RE)F_4:RE^{3+} systems, dimensions of at least 100 particles were measured to provide an acceptable statistical account of their particle size distribution.

3.3. Results and discussion (Part 1)

3.3.1. Microwave-assisted solvothermal synthesis and characterization of Li(RE)F_4 microparticles

Upconverting $LiYF_4$ microparticles co-doped with Yb^{3+}(18%)/Er^{3+}(2%) and Yb^{3+}(25%)/Tm^{3+}(0.5%), downshifting $LiYF_4$ microparticles co-doped with Ce^{3+}(2%)/Tb^{3+}(2%) and Nd^{3+}(2.5-25%), upconverting $LiYbF_4$ microparticles doped with

Er^{3+}(2%), and non-luminescent $LiYF_4$ microparticles were all synthesized *via* the developed microwave-assisted solvothermal methods №1 and №2. Presented in **Figure 11** are the SEM/TEM micrographs of all aforementioned materials.

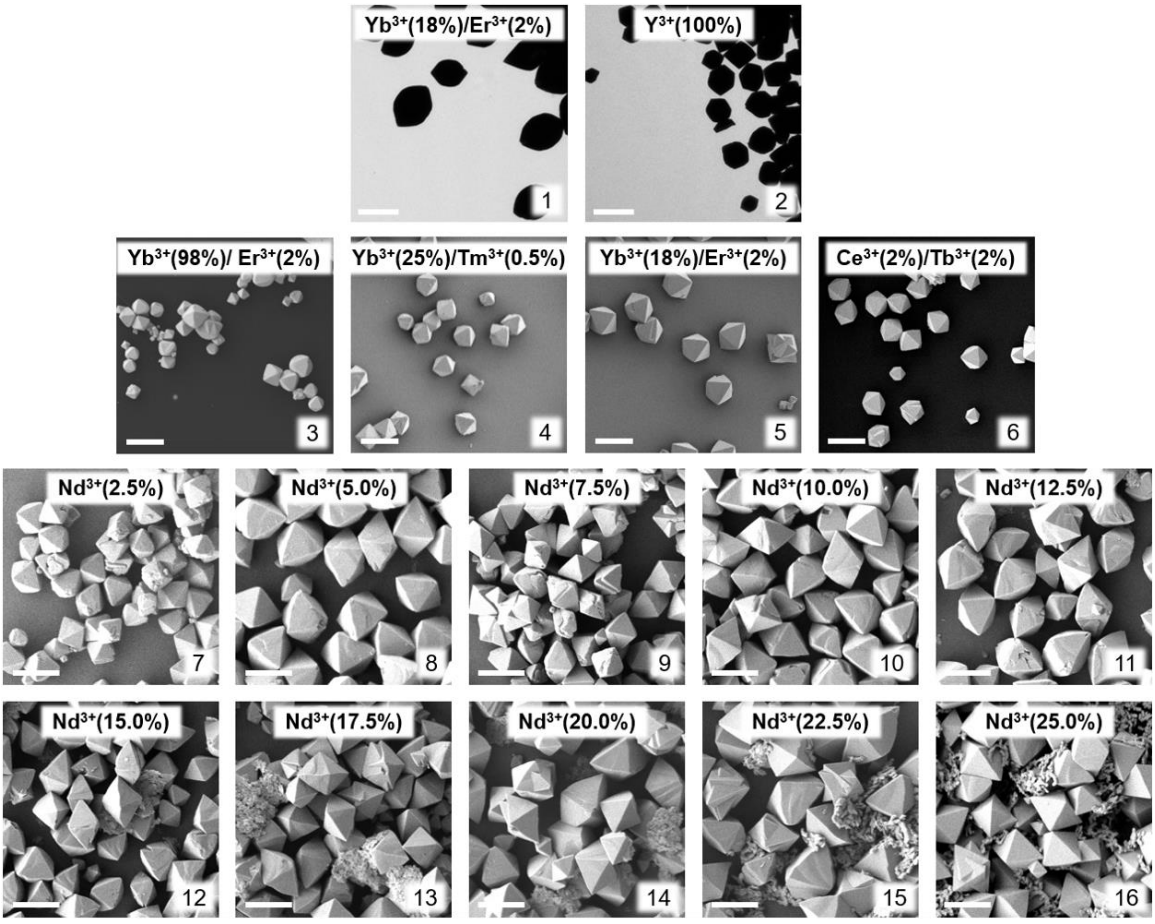

Figure 11. (1,2) TEM micrographs of $LiYF_4$:Yb^{3+}/Er^{3+} and $LiYF_4$ microparticles obtained *via* microwave-assisted solvothermal method №2 (Li^+:RE^{3+} 4.3, pH 5.3, 2 mL, 180 °C, 2 min). Scale bars: 2 μm. (3-6) SEM micrographs of $LiYF_4$:RE^{3+} microparticles obtained *via* method №1 (Li^+:RE^{3+} 4.3, pH 5.3, 11 mL, 200 °C, 10 min). Scale bars: 4 μm. (7-16) SEM micrographs of $LiYF_4$:Nd^{3+}(X%) microparticles obtained *via* method №2 with a modified reaction duration (20 min for X = 2.5–15.0%, 30 min for X = 17.5%, and 60 min for X = 20.0–25.0%). Scale bars: 2 μm.

Regardless of the dopant system, all particles have a uniaxially elongated square-based bipyramidal morphology and are characterized by an AR ranging from 1.1 to 1.3. This morphology can be explained on the basis of $LiYF_4$ crystal structure. $LiYF_4$ crystallizes in a tetragonal crystal system (scheelite structure).[45] The microparticles are faceted by eight equivalent, lowest energy {101} crystallographic planes, which induce the observed

square-based bipyramidal morphology.[108] Because the unit cell of a tetragonal crystal system is defined by the following lattice parameters: $a = b \neq c$ ($\alpha, \beta, \gamma = 90°$), the axis along which the particles are unidirectionally elongated can be identified as the crystallographic *c*-axis.[108]

The exact particle dimensions of all $LiYF_4:RE^{3+}$ systems are listed in **Table 4**.

Table 4. Dimensions of all $LiYF_4:RE^{3+}$ microparticle systems obtained *via* microwave-assisted solvothermal synthesis methods №1 and №2.

	$LiYF_4:RE^{3+}$	**Height (μm)**	**Width (μm)**	**Aspect Ratio**
Method №1	Yb^{3+}(98%)/Er^{3+}(2%)	1.7 ± 0.5	1.6 ± 0.3	1.1
	Yb^{3+}(25%)/Tm^{3+}(0.5%)	3.8 ± 0.4	3.3 ± 0.2	1.2
	Yb^{3+}(18%)/Er^{3+}(2%)	4.4 ± 0.4	4.0 ± 0.2	1.1
	Ce^{3+}(2%)/Tb^{3+}(2%)	3.4 ± 0.6	3.0 ± 0.2	1.1
Method №2	Undoped	1.8 ± 0.3	1.6 ± 0.1	1.1
	Yb^{3+}(18%)/Er^{3+}(2%)	3.1 ± 0.4	2.5 ± 0.2	1.3
	Nd^{3+}(2.5%)	1.7 ± 0.1	1.6 ± 0.1	1.1
	Nd^{3+}(5%)	2.8 ± 0.2	2.4 ± 0.1	1.2
	Nd^{3+}(7.5%)	2.1 ± 0.1	1.7 ± 0.1	1.2
	Nd^{3+}(10%)	2.5 ± 0.2	2.2 ± 0.1	1.2
	Nd^{3+}(12.5%)	2.6 ± 0.2	2.0 ± 0.1	1.3
	Nd^{3+}(15%)	2.1 ± 0.1	1.8 ± 0.1	1.2
	Nd^{3+}(17.5%)	2.3 ± 0.2	1.8 ± 0.1	1.3
	Nd^{3+}(20%)	2.5 ± 0.2	2.0 ± 0.1	1.2
	Nd^{3+}(22.5%)	2.8 ± 0.2	2.4 ± 0.1	1.2
	Nd^{3+}(25%)	2.5 ± 0.1	2.1 ± 0.1	1.2

Particle height and width correspond to the vertex-to-vertex lengths of the elongated and the shorter, perpendicular axes, respectively (as depicted in **Figure 10** of **Section 3.2.2**).

The relative standard deviation of the size distribution for 12 out of the 16 $LiYF_4:RE^{3+}$ systems reported in **Table 4** is within the ± 4–10% range, meaning that most of the time, the herein developed synthesis methods yield particles with an acceptable degree of monodispersity.[XIII]

For the exception of $LiYbF_4:Er^{3+}$ microparticles, all particles obtained *via* method №1 are larger than those obtained *via* method №2. This (almost) systematic difference in size

[XIII] The range of the standard deviation (± X μm) of the microparticles' height and width measurements expressed as a percentage.

may arise from the differences in physicochemical reaction parameters between the two synthesis methods.

Method №2 utilizes a lower reaction mixture volume as compared to method №1 (2 *vs*. 11 mL, respectively) and a higher true reaction temperature (*vide infra* **Section 3.4.2.3**).[XIV] Higher internal reaction vessel pressure fostered by the conditions associated with method №2 (*ca*. 2 bar higher) evidences that a higher fraction of the solvent system is evaporated in the course of a reaction. Consequently, despite the initial concentration of the solubilized precursors being the same in both approaches, reaction conditions in method №2 foster a more rapid supersaturation of the reaction mixture and thus a higher nucleation rate. Since the relative proportion of reagents is equal in both approaches, but the reaction conditions in method №2 result in more particle nucleation sites, particles obtained *via* method №2 are smaller, *i.e.*, the same quantity of precursor is distributed among a higher number of (smaller) particles. This reasoning is in line with the *LaMer* crystallization mechanism.[109] With regard to the observed particle size difference between the various $LiYF_4:RE^{3+}$ systems, although the dopant type and its relative concentration is known to exert influence over particle size, no obvious trend was observed herein.[108]

As for the analysis of crystallographic data, it is evident from **Figure 12-A** (*vide infra*) that diffraction patterns of all $LiYF_4:RE^{3+}$ systems presented are in good agreement with the referenced pattern of $LiYF_4$ (PDF#: 01-081-1940). A more careful analysis of the reflections centered at *ca*. 19° and 30° 2θ, which correspond to the interplanar distances between the (101) and (112) planes, respectively, reveals a slight contraction of the $LiYF_4$ crystal lattice upon doping with lanthanide cations (Ln^{3+}) that are smaller than Y^{3+} (*i.e.*, Er^{3+}, Tm^{3+}, and Yb^{3+}). This is evidenced by the observed rightward shift of the (101) and (112) reflections as a function of increasing Ln^{3+} dopant concentration (from *ca*. 19.1° and 29.6° 2θ in undoped $LiYF_4$ to *ca*. 19.4° and 30.0° 2θ in $LiYbF_4:Er^{3+}$(2%); **Figure 12-B1**). This observation is congruent with the Bragg's law and previously published work.[75]

[XIV] The true reaction temperature in method №2 is higher than the true reaction temperature in method №1, despite the nominal temperature setting (180 °C) in method №1 being lower than the nominal temperature setting (200 °C) in method №2.

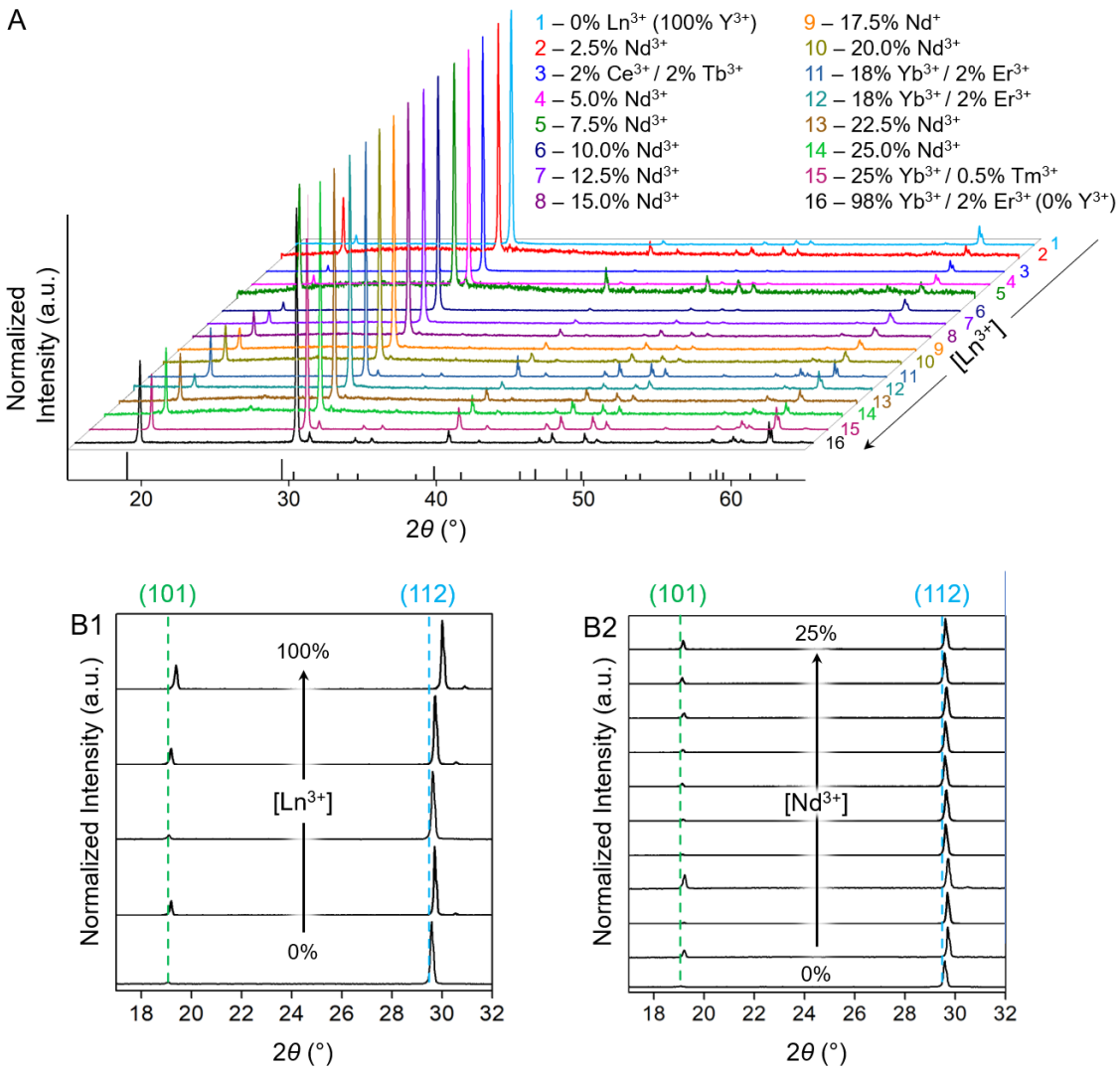

Figure 12. A) XRD patterns of all Li(RE)F_4 systems obtained *via* the developed microwave-assisted synthesis methods. Each pattern was normalized to the intensity of the respective 100% reflection centered at *ca*. 30 °2θ, which is assigned to the (112) crystallographic plane in $LiYF_4$. $LiYF_4$ reference pattern was obtained from PDF#: 01-081-1940. B1) XRD patterns of Li(RE)F_4 systems featuring a range of Ln^{3+} dopant concentrations. Listed from the bottom to the top: undoped $LiYF_4$ (Method №1), $LiYF_4$:Yb^{3+}(18%)/Er^{3+}(2%) (Method №1), $LiYF_4$:Yb^{3+}(18%)/Er^{3+}(2%) (Method №2), $LiYF_4$:Yb^{3+}(25%)/Tm^{3+}(0.5%) (Method №1), and $LiYbF_4$:Er^{3+}(2%) (Method №1). B2) XRD patterns of $LiYF_4$:Nd^{3+} (0-25%; 2.5% increments) systems obtained via Method №2 with modified reaction durations. Positions of the referenced (101) and (112) reflections were obtained from PDF#: 01-081-1940.

Surprisingly, an expected $LiYF_4$ lattice expansion (as would be evidenced by a leftward shift of the (101) and (112) reflections) upon increased doping with Nd^{3+}, which is larger than Y^{3+}, was not observed (**Figure 12-B2**). Lastly, the observed variability of the relative reflection intensities between the normalized diffraction patterns is most likely a

consequence of a sub-optimal sample preparation technique for analysis *via* powder X-ray diffraction.[XV, 110]

Most importantly, characterization results provided above demonstrate adequate synthesis reproducibility and the capacity to yield $Li(RE)F_4$ microparticles with a well-defined bipyramidal morphology and an acceptable monodispersity across the various dopant systems. However, it should be noted that phase-pure $LiYF_4:Nd^{3+}$ could not be obtained beyond a Nd^{3+} dopant concentration of 12.5% (as evidenced by the presence of a low-crystallinity co-phase responsible for the second morphology observed in the SEM micrographs of **Figure 11 (12–16)** and the low resolution reflection at *ca*. 25° 2θ in **Figure 12 (8–14)**; *vide infra* the results of a time-dependent study presented in **Section 3.4.3**, which suggest this phase to be $Y_X(NH_4)_YF_Z:Nd^{3+}$).

The next section of the discussion details the development of the microwave-assisted solvothermal synthesis approaches used to obtain all of the aforementioned $Li(RE)F_4$ microparticle (as well as $Na(RE)F_4$ nanoparticle) systems.

3.3.2. First synthesis attempt

In a first attempt to synthesize monodisperse $LiYF_4$ microparticles (co-doped with Yb^{3+}(25%)/Tm^{3+}(0.5%) *via* the microwave-assisted solvothermal approach, a method for the synthesis of $NaYF_4$ nanoparticles reported by Reddy *et al.* was initially adopted (M^+:RE^{3+} ratio 7.5, pH 5.3, 150 °C, 3 h).[92] However, simply substituting Na^+ for Li^+ in the $M(RE)F_4$ structure of the targeted material did not yield phase-pure $LiYF_4:Yb^{3+}/Tm^{3+}$. Instead, a small fraction of tetragonal-phase, submicron-scale $LiYF_4:Yb^{3+}/Tm^{3+}$ particles with a square-based bipyramidal morphology and LiF were obtained along with hexagonal-phase $Y(OH)_XF_Y$ nanorods constituting the major product (*vide infra* **Figure 13**).

[XV] Drop casting a concentrated microparticle dispersion onto a glass substrate yielded microparticle films (often monolayers), in which some particles (crystallites) exhibited a preferred spatial orientation and thus a preferred crystallographic direction normal to the substrate's surface. This is supported by the SEM micrographs reported in **Figure 11**. The varying fractions of microparticles exhibiting the preferential spatial alignment in the different samples thus resulted in the relative peak intensity variance.

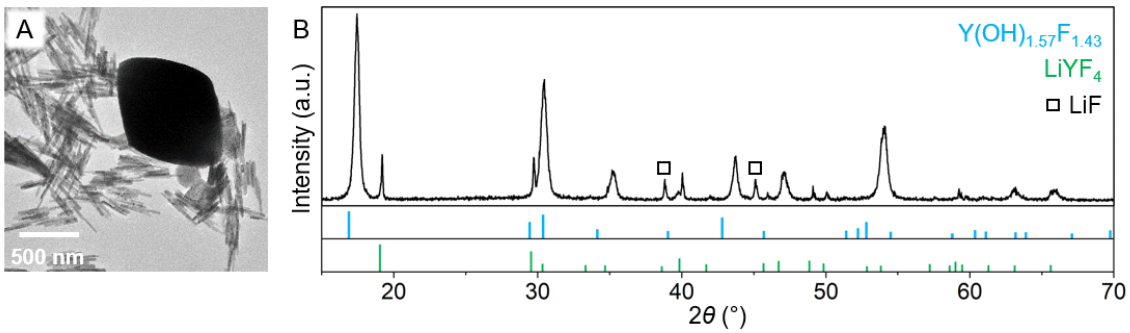

Figure 13. A) TEM micrograph depicting $LiYF_4$ microparticles and $Y(OH)_XF_Y$ nanorods obtained under the following reaction conditions: Li^+:RE^{3+} ratio 7.5, pH 5.3, 150 °C, 3 h. B) Respective XRD pattern. References: $Y(OH)_XF_Y$ (PDF#: 01-080-2008), $LiYF_4$ (PDF#: 01-081-1940), LiF (PDF#: 00-004-0857).

This observation demonstrates the complexity of the synthesis approach and highlights the importance of understanding its underlying materials chemistry. Therefore, to gain access to $LiYF_4$ microparticles featuring various RE^{3+} dopant systems, a deeper understanding of the parameters governing material formation and growth in the Li-RE-F system under microwave-induced solvothermal conditions had to be obtained. This was accomplished by investigating the effects of the Li^+:RE^{3+} ratio, reaction temperature, reaction duration, and the initial reaction mixture pH on the synthesis outcome. A detailed discussion of this investigation and the consequent development of synthesis method №1 is presented in the following sections. It should be noted that although the following discussion on method №1 development mentions $LiYF_4$:RE^{3+} as the target material, the actual target material was $LiYF_4$:Yb^{3+}(25%)/Tm^{3+}(0.5%). Nevertheless, after having established the optimal synthesis conditions that constitute method №1, a range of other $Li(RE)F_4$ microparticle systems (those reported in **Section 3.3.1**) was obtained.

3.3.3. Effect of Li^+:RE^{3+} ratio

In the context of $M(RE)F_4$ material synthesis, the M^+:RE^{3+} ratio has a significant influence on the phase, size and morphology of the targeted material and depends on the chemical nature of the metal ion constituents as well as the accompanying reaction parameters.[92,94] In this regard, it is not surprising that a mere substitution of the M^+ from

Na^+ to Li^+ in an attempt to synthesize $LiYF_4$ over $NaYF_4$ *via* the initially adopted approach did not yield phase-pure $LiYF_4$.[92]

To identify a suitable Li^+:RE^{3+} ratio for the microwave-assisted formation of RE^{3+}-doped $LiYF_4$, the effect of varying this reaction parameter was first investigated under the intrinsic pH conditions of the reaction mixture (pH 5.3) as well as the original reaction temperature and duration conditions (150 °C and 3 h). Because the initially adopted approach required a high stoichiometric excess of M^+ *vs.* RE^{3+} (7.5), the amount of $LiOH{\cdot}H_2O$ was lowered to achieve a Li^+:RE^{3+} ratio of 4.3 and 2.0.

As reported in **Section 3.3.2**, $LiYF_4$ submicron-scale particles with a square-based bipyramidal morphology were obtained as a minor product in a mixture with $Y(OH)_XF_Y$ nanorods and LiF in the reaction carried out with the original Li^+:RE^{3+} ratio of 7.5 (*vide infra* **Figure 14-A/B-3**). Lowering the Li^+:RE^{3+} ratio to 2.0 also yielded $LiYF_4$ as a minor product, but the resulting particles were in the microscale realm (**Figure 14-A/B-1**). The dominant phase obtained under these conditions, however, was attributed to $Y_3(NH_4)F_{10}$.

In addition, formation of nanoparticles of an unidentified phase was observed under this Li^+:RE^{3+} ratio (denoted as NPs in **Figure 14-B-1** and other subsequent, relevant figures). Most importantly, $LiYF_4$ microparticles were obtained as a greater fraction of the overall product at a Li^+:RE^{3+} ratio of 4.3, with the secondary phase being once again attributed to $Y(OH)_XF_Y$ (**Figure 14-A/B-2**). In all cases, the relative abundance of phases was judged by comparing the relative intensities of their respective XRD reflections and the relative abundance of each morphology as observed from the TEM micrographs.

These results indicate that formation of $LiYF_4$ is feasible at all three Li^+ to RE^{3+} ratios; however, a ratio of 4.3 may be more optimal for targeting $LiYF_4$ under solvothermal conditions. Thus, a Li^+:RE^{3+} ratio of 4.3 was used in subsequent optimization of the other reaction parameters: reaction temperature, duration, and pH.

It is important to note that the different $LiOH{\cdot}H_2O$ amounts used in this investigation fell within the buffering regime of acetic acid/acetate (buffer produced *in-situ* by reaction of acetic acid with LiOH), and thus did not significantly alter the pH of the system. Therefore, the results obtained by varying the amount of $LiOH{\cdot}H_2O$ can be attributed to the Li^+:RE^{3+} ratio itself and not to the pH of the system.

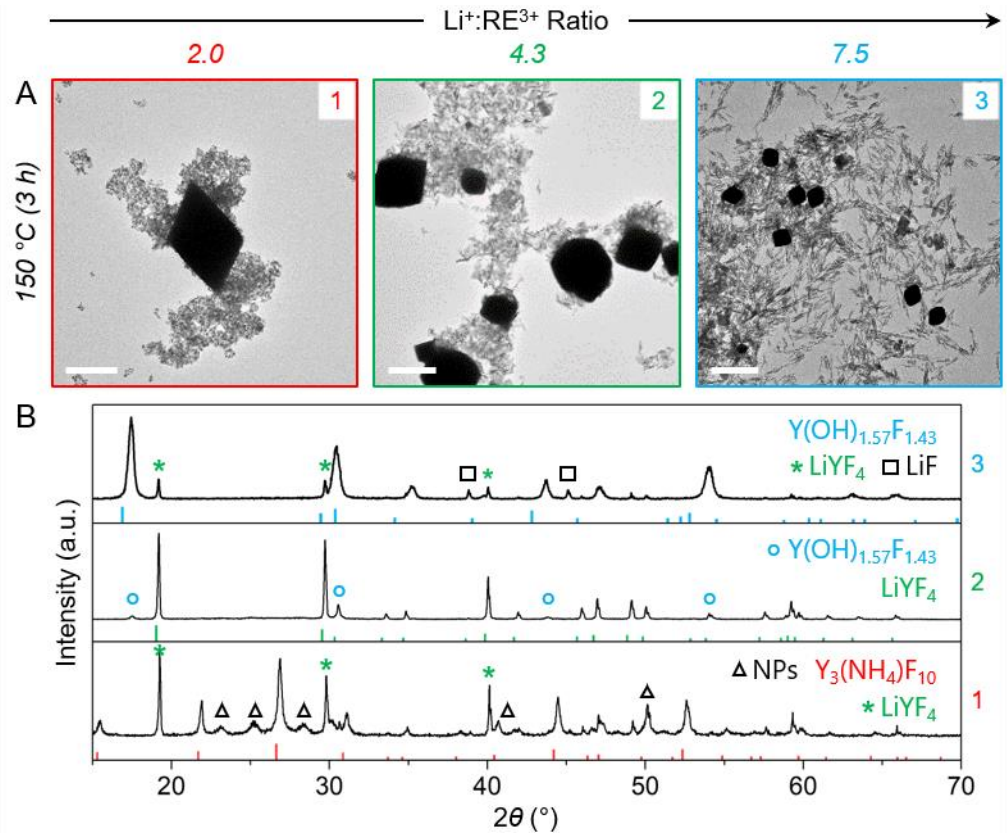

Figure 14. A) TEM micrographs of materials obtained under the initially adopted reaction temperature/duration/pH conditions (150 °C, 3 h, pH 5.3) and various Li^+:RE^{3+} ratios (2.0, 4.3, and 7.5). Scale bars: 2 µm. B) XRD patterns of materials presented in A. References: $Y(OH)_{1.57}F_{1.43}$ (PDF#: 01-080-2008), $LiYF_4$ (PDF#: 01-081-1940), $Y_3(NH_4)F_{10}$ (PDF#: 01-074-2889), LiF (PDF#: 00-004-0857).

Lastly, it may be observed that reflections in the XRD patterns attributed to $Y(OH)_XF_Y$ nanorods obtained under reaction conditions employing Li^+:RE^{3+} ratios of 4.3 and 7.5 (**Figure 14-B-2/3**) appear to be shifted rightward when compared to the reflections of the reference phase – $Y(OH)_{1.57}F_{1.43}$ (PDF#: 01-080-2008). Nevertheless, the here obtained XRD pattern is in good agreement with those reported for numerous $Y(OH)_XF_Y$ systems with varying OH:F ratios.[111–113] To provide further phase confirmation, Maud[107] software was used to simulate the effect of varying a single unit cell lattice parameter of the referenced $Y(OH)_{1.57}F_{1.43}$ nanorods on the resulting shift of the reflections. A perfect match with the shift of the obtained $Y(OH)_XF_Y$ nanorods was obtained when the crystallographic *a*-axis of the unit cell was shortened from 6.08 to 5.88 Å, while keeping the *b* and *c* unit cell parameters constant at 6.08 and 3.55 Å, respectively (*vide infra* **Figure 15**).

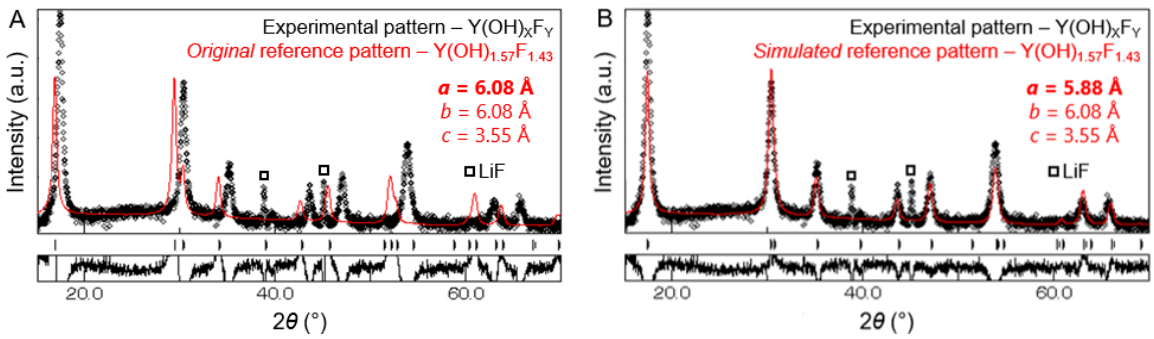

Figure 15. Simulation of unit cell lattice parameters for $Y(OH)_{1.53}F_{1.47}$ to reconcile an inadequate match with the reflections of the obtained material – $Y(OH)_XF_Y$. A) XRD patterns of as-obtained $Y(OH)_XF_Y$ nanorods and the reference material prior to adjustment of unit cell parameters (a = 6.08 Å). B) XRD patterns of as-obtained $Y(OH)_XF_Y$ nanorods and the reference material after adjustment of unit cell parameters (a = 5.88 Å).

To provide additional support for the attribution of this phase, $Y(OH)_XF_Y$ nanorods obtained in a mixture with $LiYF_4$ (Li^+:RE^{3+} ratio of 7.5) were annealed at 600 °C for 2 h in air, and YOF was obtained as evidenced by the XRD pattern presented in **Figure 16**.

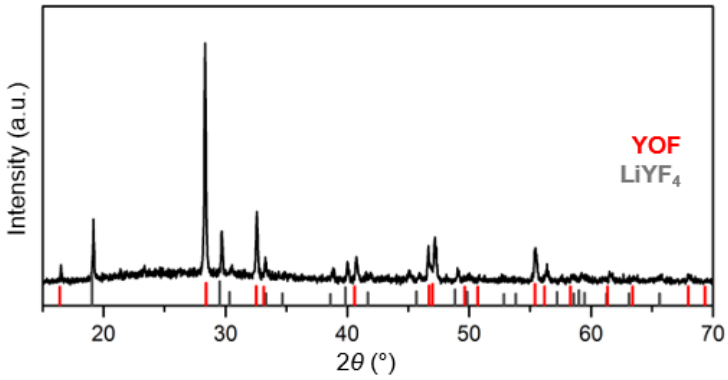

Figure 16. XRD of YOF obtained after annealing $Y(OH)_XF_Y$ nanorods at 600 °C for 2 h in air. References: YOF (PDF#: 00-006-0347), $LiYF_4$ (PDF#: 01-081-1940).

Such phase transformation is in accordance with what is reported in the literature for analogous RE^{3+}-doped YOF systems.[113]

3.3.4. Effect of elevated reaction temperature

Having determined the most promising Li^+:RE^{3+} ratio allowing for the synthesis of $LiYF_4$ microparticles under the intrinsic pH conditions of the reaction mixture (pH 5.3) and the original reaction temperature/duration conditions (150 °C, 3 h), the reaction temperature/duration profile of the microwave-assisted solvothermal method was the next parameter subject to investigation.

Taking advantage of the tunable temperature settings of the microwave reactor, a dynamic, three-stage temperature profile was implemented in place of the initially adopted static heating at 150 °C for 3 h. The new dynamic heating method is characterized by a rapid increase in temperature to 210 °C, which is then immediately followed by rapid cooling to the set temperature of 200 °C. Such a dynamic temperature profile was expected to yield a more homogeneous particle size distribution of the final product by separating the particle nucleation event (rapid increase to 210 °C) from the particle growth stage (static heating at 200 °C).[114] It was hypothesized that a higher temperature regime would promote the formation of the major phase from the mixture of phases obtained at all Li^+:RE^{3+} ratios and original reaction temperature/duration conditions (150 °C, 3 h).

Furthermore, it was also hypothesized that an elevated reaction temperature would accelerate the reaction kinetics, and thus a decrease in overall reaction duration from 3 h to 10 min was investigated simultaneously. The 10 min reaction duration was chosen on the basis that similar timeframes were previously employed to target $M(RE)F_4$ particles *via* microwave-assisted synthesis.[90,94]

At a pH value of 5.3 and a Li^+:RE^{3+} ratio of 4.3, this new method fostered preferential synthesis of RE^{3+}-doped $LiYF_4$, the dominant phase of the corresponding reaction conducted at 150 °C for 3 h (*vide infra* **Figure 17-A/B-2**). Similarly, this newly developed heating method also fostered preferential synthesis of $Y_3(NH_4)F_{10}$ and $Y(OH)_XF_Y$ at Li^+:RE^{3+} ratios of 2.0 (**Figure 17-A/B-1**) and 7.5 (**Figure 17-A/B-3**), respectively, out of the mixture of phases obtained at the original temperature/duration regime (150 °C for 3 h). Whereas formation of phase-pure $LiYF_4$ and $Y(OH)_XF_Y$ was observed at Li^+:RE^{3+} ratios of 4.3 and 7.5, respectively, $Y_3(NH_4)F_{10}$ was once again accompanied by the formation of nanoparticles of an unidentified phase at a Li^+:RE^{3+} ratio of 2.0.

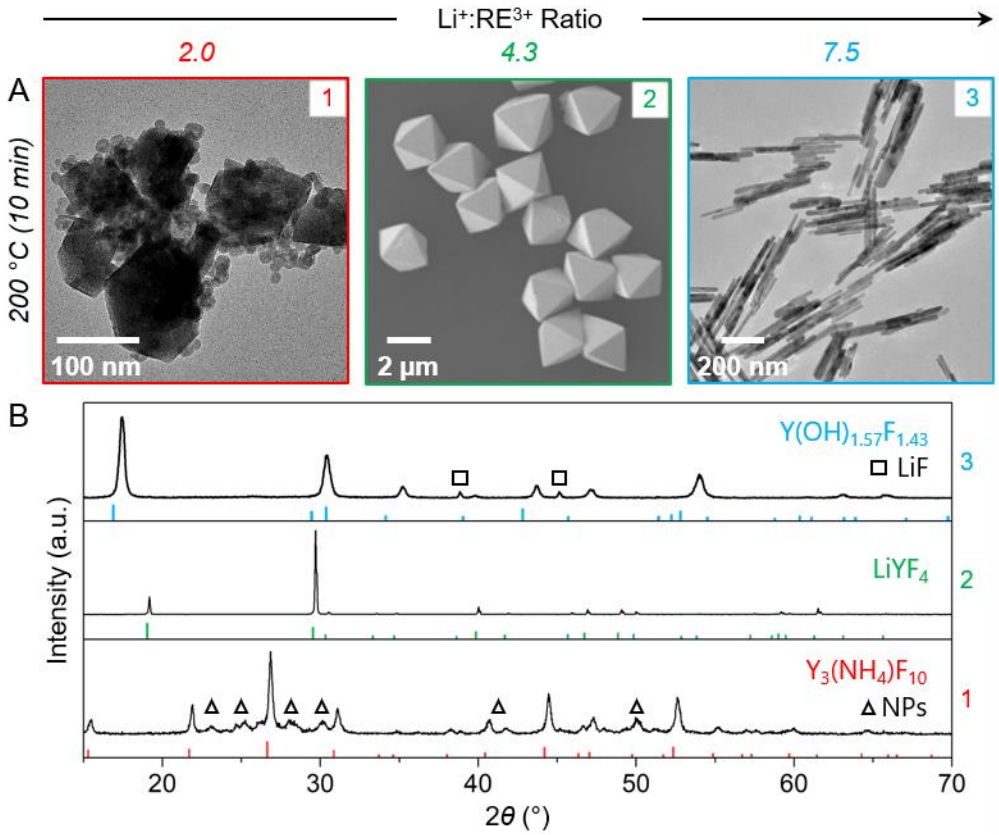

Figure 17. A) 1, 3) TEM and 2) SEM micrograph(s) of materials obtained under modified reaction temperature/duration conditions (200 °C, 10 min), adopted pH conditions (5.3) and various Li^+:RE^{3+} ratios (2.0, 4.3, and 7.5). B) XRD patterns of materials presented in A. References: $Y(OH)_{1.57}F_{1.43}$ (PDF#: 01-080-2008), $LiYF_4$ (PDF#: 01-081-1940), $Y_3(NH_4)F_{10}$ (PDF#: 01-074-2889), LiF (PDF#: 00-004-0857).

From the TEM micrograph presented in **Figure 17-A-1** it is evident that $Y_3(NH_4)F_{10}$ crystallizes in a plate-like morphology. Further confirmation of phase-to-morphology assignment with regard to $Y_3(NH_4)F_{10}$ and the unidentified phase is provided in the following section.

Aforementioned results confirm the hypothesis that a higher temperature regime (200 °C) has the effect of promoting the formation of the major phase out of the mixture of phases obtained at a lower temperature (150 °C) and shortening the reaction duration (10 min *vs*. 3 h). Most importantly, it was determined that phase-pure $LiYF_4$ microparticles could be obtained *via* microwave-assisted solvothermal synthesis under the following reaction conditions: Li^+:RE^{3+} ratio of 4.3, reaction temperature of 200 °C, a reaction duration of 10 min, and an initial reaction mixture pH of 5.3

3.3.5. Further support for the established temperature/duration reaction dynamics

To provide further support for the herein established hypothesis that a higher temperature (200 °C) promotes the formation of the major phase out of the mixture of phases obtained at a lower temperature (150 °C) in a shorter timeframe (10 min *vs*. 3 h), a control experiment was conducted at all Li^+:RE^{3+} ratios, a static heating temperature of 150 °C and a reaction duration of 10 min.

Only one of these three experiments yielded the same material that was obtained at the elevated temperature. More specifically, $Y(OH)_XF_Y$ nanorods were obtained at a Li^+:RE^{3+} ratio of 7.5 (*vide infra* **Figure 18-A/B-3**). However, at a Li^+:RE^{3+} ratio of 2.0, the product is constituted of a single morphology equivalent to the nanoparticles of unidentified phase that were previously observed during all experiments employing this ratio (**Figure 18-A/B-1**). The same nanoparticles were obtained together with $Y_3(NH_4)F_{10}$ at a Li^+:RE^{3+} ratio of 4.3 (**Figure 18-A/B-2**). Results presented in **Figure 18-A/B-1/2** provide unequivocal support for the attribution of the nanoparticle morphology to the unidentified phase and the irregular plate structures to $Y_3(NH_4)F_{10}$. In addition to all of the aforementioned products, formation of LiF was observed at all three Li^+:RE^{3+} ratios as evidenced by the XRD patterns in **Figure 18-B-1/2/3**.

As evident from **Figure 18**, formation of $LiYF_4$ was not observed after a 10 min heat treatment at 150 °C irrespective of the chosen Li^+ to RE^{3+} ratio. Conversely, a 10 min heat treatment at 200 °C fostered phase-pure $LiYF_4$ formation at a Li^+:RE^{3+} ratio 4.3 and a 3 h heat treatment at 150 °C fostered partial $LiYF_4$ formation (phase mix) at all three Li^+ to RE^{3+} ratios. From this it is evident that a lower reaction temperature has the effect of retarding the kinetics of $LiYF_4$ formation and hinders a complete phase transformation even when the reaction duration is prolonged to 3 h. Ultimately, it can be concluded that temperature (over time) plays a pivotal role in the synthesis of $LiYF_4$, as it supplies the adequate threshold energy required for rapid $LiYF_4$ formation under the optimal Li^+:RE^{3+} ratio conditions (4.3) and the intrinsic reaction mixture pH (5.3).

In other words, reaction temperature-duration dynamics of this solvothermal approach are characterized by an inverse relationship – a more rapid synthesis of phase-pure $LiYF_4$ may be achieved by appropriately increasing the reaction temperature.

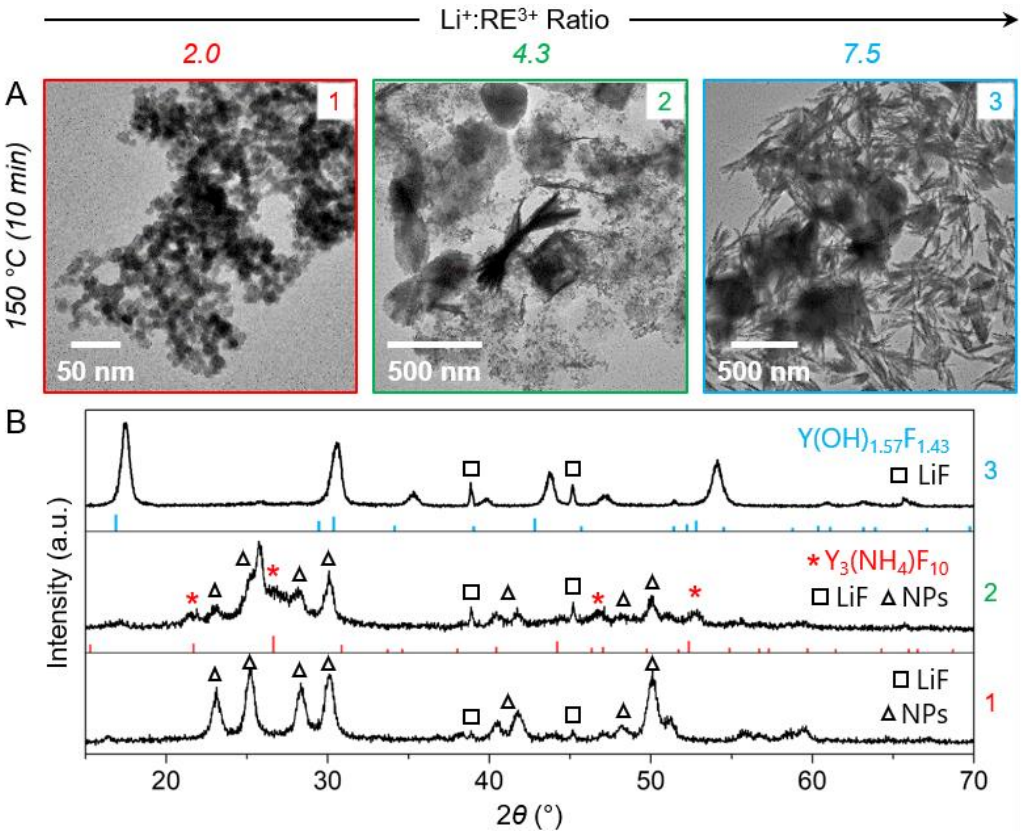

Figure 18. A) TEM micrographs of materials obtained under modified reaction duration conditions (10 min), adopted reaction temperature/pH conditions (150 °C, 5.3) and various Li^+:RE^{3+} ratios (2.0, 4.3, and 7.5). B) XRD patterns of materials presented in A. References: $Y(OH)_XF_Y$ (PDF#: 01-080-2008), $Y_3(NH_4)F_{10}$ (PDF#: 01-074-2889), LiF (PDF#: 00-004-0857).

3.3.6. Proposed growth mechanism of the $LiYF_4$ microparticles under microwave-induced solvothermal conditions

In order to propose a growth mechanism by which the RE^{3+}-doped $LiYF_4$ microparticles are formed under the optimal Li^+:RE^{3+} ratio (4.3), intrinsic reaction mixture pH (5.3), and reaction temperature/duration conditions (200 °C for 10 min), the particle growth stage (static heating at 200 °C) was systematically increased from 1 to 5, 7.5, and 10 min (*vide infra* **Figure 19**).

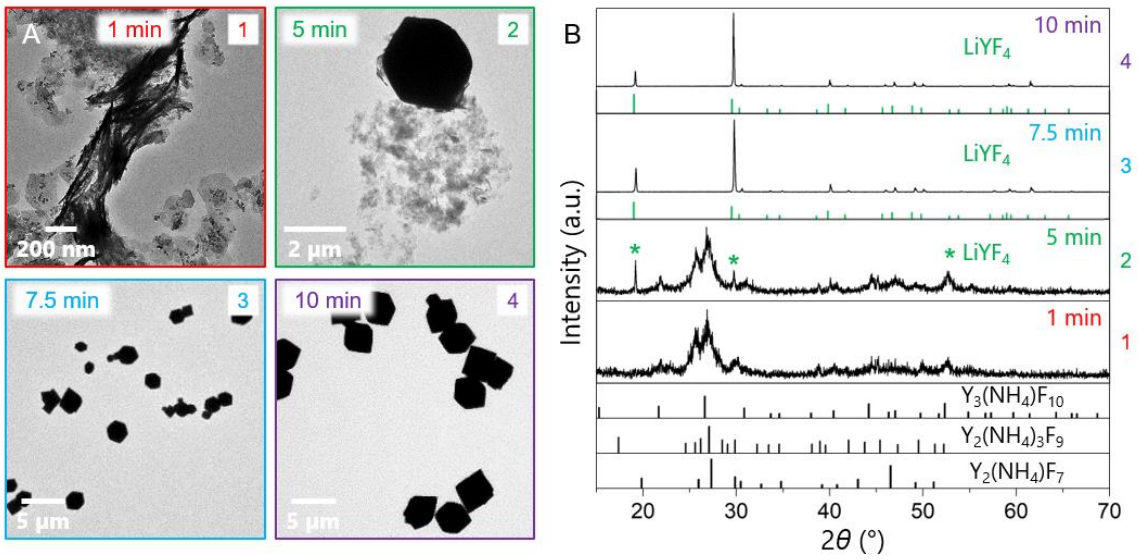

Figure 19. A) TEM micrographs of materials obtained by microwave-assisted heating at 200 °C for 1 (A1), 5 (A2), 7.5 (A3), and 10 (A4) min (Li^+:RE^{3+} 4.3, pH 5.3). B) XRD patterns of materials presented in A. References: $LiYF_4$ (PDF#: 01-081-1940), $Y_3(NH_4)F_{10}$ (PDF#: 01-074-2889), $Y_2(NH_4)_3F_9$ (PDF#: 00-043-0840), $Y_2(NH_4)F_7$ (PDF#: 00-043-0847).

As demonstrated by the TEM and XRD results presented in **Figure 19-A/B-1**, formation of $LiYF_4$ is preceded by a set of $Y_X(NH_4)_YF_Z$ phases after 1 min.[115] In fact, the beginning of $LiYF_4$ formation is first observed after 5 min as evidenced by the emerging XRD reflections characteristic of this phase and supported by the appearance of a second, microscale morphology (**Figure 19-A/B-2**). After 7.5 min, complete disappearance of the XRD reflections attributed to the intermediary $Y_X(NH_4)_YF_Z$ phases and the consequent formation of $LiYF_4$ as the sole reaction product is observed (**Figure 19-A/B-3**). These observations suggest that the $Y_X(NH_4)_YF_Z$ phases serve as an yttrium and fluoride reservoir for $LiYF_4$ during a phase transformation period that takes place between 1 and 7.5 min of the synthesis. Furthermore, from the TEM micrographs presented in **Figure 19-A**, a clear size evolution of the $LiYF_4$ particles from approximately 2 µm (5 min) to 2.5 µm (7.5 min) and finally 4 µm (10 min) *via* ripening is evident. More important, however, is the obvious increase in particle size homogeneity between 5 and 10 min, a particle growth period by the end of which monodisperse $LiYF_4$ microparticles are obtained.

This time-dependent study reveals that a 10 min heat treatment at 200 °C is the shortest possible reaction duration during which $LiYF_4$ microparticles with good size monodispersity can be obtained under the following reaction conditions: Li^+:RE^{3+} ratio of

4.3, reaction temperature of 200 °C and an intrinsic reaction mixture pH of 5.3. On this basis, it is also demonstrated that the growth mechanism of $LiYF_4$ *micro*particles does not involve the initial formation of $LiYF_4$ *nano*particles that subsequently grow in size. Rather, the initial formation of a sacrificial phase has been identified as an intermediate step towards $LiYF_4$ microparticle formation.

3.3.7. Effect of initial reaction mixture pH

To gain control over the phase, size and morphology of the target product, pH-sensitive ligands with a selective affinity for particular facets of the developing crystalline material are often utilized in the synthesis of $M(RE)F_4$-based materials.[103,116,117] Thus, the pH-dependent abundance of such growth-guiding ligands, their intrinsic chemical nature and solvent compatibility are important physicochemical reaction parameters to consider when developing a new synthesis method.[74] For this study, the acetic acid (CH_3COOH) / acetate (CH_3COO^-) system was selected on the basis of its excellent H_2O/ethanol solvent compatibility and successful application as a particle capping ligand in a previously reported microwave-assisted solvothermal $M(RE)F_4$ material synthesis.[92] The effect of the pH-dependent abundance of the *in-situ* generated acetate molecules on the structural and morphological characteristics of $LiYF_4$ was demonstrated by adjusting the intrinsic acetate ion fraction in the reaction solution (pH 5.3 yielding approximately 77% acetate) to 0% and 100%. These two extremes of relative acetate abundance were induced by adjusting the pH to 2.0 and 7.5 with HCl and NH_4OH, respectively (*vide infra* **Figure 20**).

Employing the optimal Li^+:RE^{3+} ratio and reaction temperature/duration profile while minimizing acetate abundance (pH 2.0) resulted in the formation of YF_3 (*vide infra* **Figure 21-A/B-1**), whereas maximizing acetate abundance (pH 7.5) resulted in the formation of a phase, identity of which could not be discerned (**Figure 21-A/B-3**).

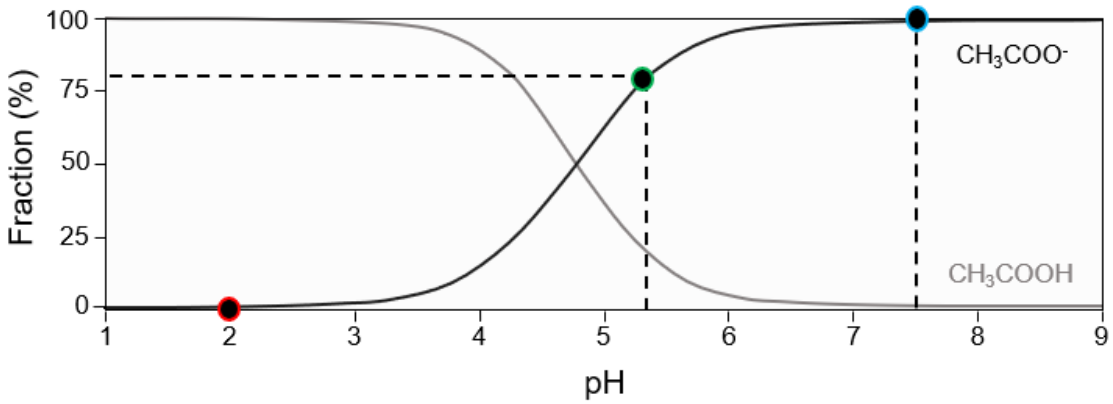

Figure 20. pH-dependent acetic acid (CH_3COOH) / acetate (CH_3COO^-) speciation curves. pH values subjected to investigation and the corresponding acetate fractions (%) are indicated by the • symbols. Accordingly, pH 2.0 corresponds to 0% CH_3COO^-, pH 5.3 to 77% CH_3COO^- and pH 7.5 to 100% CH_3COO^-.
(Figure redrawn from https://www.shimadzu.com/an/hplc/support/lib/lctalk/29/29intro.html, accessed on September 14, 2018.)

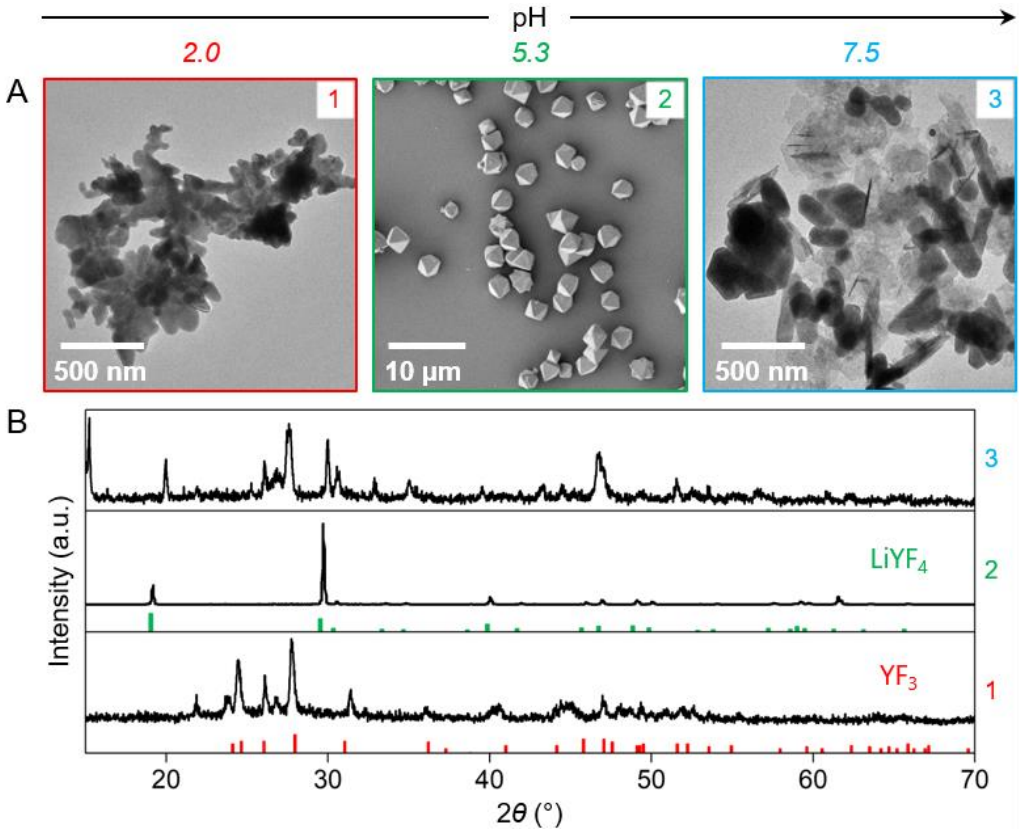

Figure 21. A) TEM micrographs of materials obtained under optimal Li^+:RE^{3+} ratio and reaction temperature/duration conditions (4.3, 200 °C, 10 min) and various reaction mixture pH conditions (2.0, 5.3 and 7.5). B) XRD patterns of materials presented in A. References: $LiYF_4$ (PDF#: 01-081-1940), YF_3 (PDF#: 00-005-0547).

Preferential formation of YF_3 over $LiYF_4$ in the lower pH regime has been previously observed.[103,117] Ye *et al.* ascribed the formation of YF_3 at pH 2 to the increased solubility of LiF nuclei that, at higher pH, were reported to transform into $LiYF_4$ upon inward Y^{3+} and F^- transport.[117] The absence of the nuclei thus hindered $LiYF_4$ formation, ultimately yielding YF_3. Hence, an increased solubility of nuclei of intermediate phases at the lower pH regime of the herein presented system is also suggested to prevent the incorporation of Li^+ into the matrix, ultimately resulting in the formation of YF_3.

With regards to morphology of the obtained products, it can be further noted that the materials obtained at pH values of 2.0 and 7.5 display highly irregular morphologies, indicating that the functional capacity of acetate as a growth-guiding ligand is disrupted at both extremes of the pH-dependent acetic acid/acetate speciation curve. Conversely, the importance of fine-tuning the surface-capping ligand concentration to suit the needs of a particular system is evident from **Figure 21-A/B-2**, which displays the formation of phase-pure $LiYF_4$ microparticles with a well-defined bipyramidal morphology. In order to confirm the *in-situ* surface functionalization of these materials with acetate ligands, FTIR analysis was performed (*vide infra* **Figure 22**).

The presence of acetate on the surface of all three samples (**Figure 22-A/B/C**) was confirmed by a signature C=O stretch at 1532 cm^{-1} and a C–O stretch at 1414 cm^{-1} that agree with the respective bands observed in the sodium acetate reference (**Figure 22-D**).

Minor presence of acetate on the surface of YF_3 is surprising (**Figure 22-A**), since the initial pH conditions under which this material was synthesized were adjusted to achieve an acetate-free environment (pH 2.0). This observation suggests that although initial pH conditions have a crucial influence on the phase, size and morphology of the reaction product, they may be subjected to subtle changes in the course of the reaction. Alternatively, it is possible that acetic acid itself binds to the positively charged surface of the obtained materials *via* its partially negative carboxyl moiety and thus contributes to the observed C=O and C–O stretches. However, this scenario is less probable due to the weaker binding affinity of acetic acid (absence of negative charge), which is likely washed away by the repetitive redispersion of the obtained materials in a water/ethanol mixture upon workup.

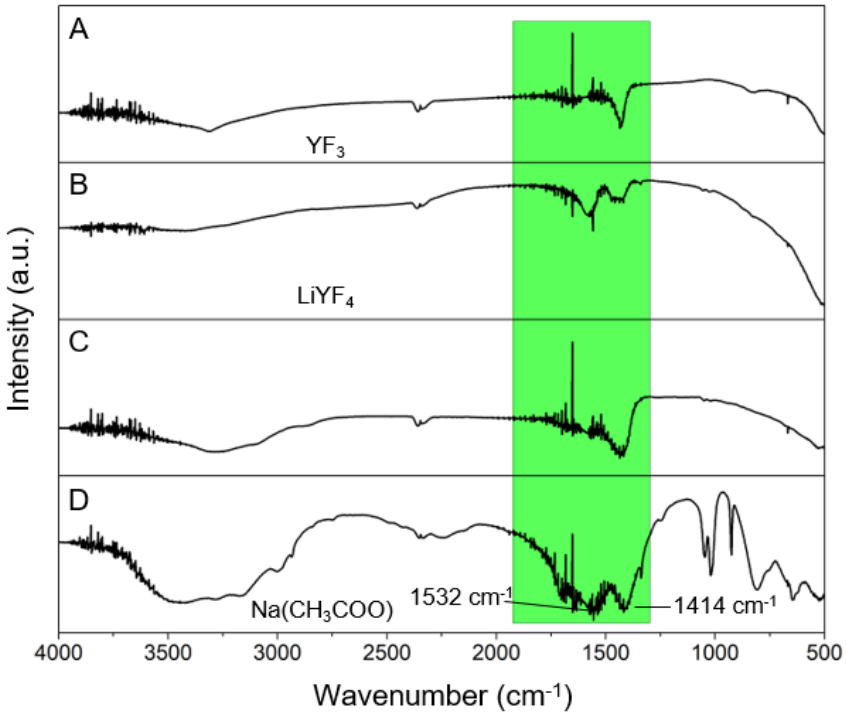

Figure 22. FTIR spectra of (A) YF_3 (pH 2.0 - 0% acetate), (B) acetate-capped $LiYF_4$ microparticles (pH 5.3 - 77% acetate), (C) acetate-capped material of unidentified phase (pH 7.5 - 100% acetate), and (D) sodium acetate [$Na(CH_3COO)$] used as a reference. C=O stretching at 1532 cm^{-1} and C–O stretching at 1414 cm^{-1} of acetate (CH_3COO^-) are highlighted. Materials presented in A to C were synthesized under optimal Li^+:RE^{3+} ratio and reaction temperature/duration conditions (4.3, 200 °C, 10 min).

In summary, optimal physicochemical conditions for the synthesis of $LiYF_4$ microparticles featuring various RE^{3+} dopant systems *via* microwave-assisted solvothermal synthesis were determined to be: a pH of 5.3, a Li^+:RE^{3+} ratio of 4.3, and a dynamic heating method, the particle growth stage of which involves heating at 200 °C for as short as 10 min. Together, these conditions comprise synthesis method №1.

3.3.8. Synthesis of $Na(RE)F_4$:Yb^{3+}/Er^{3+} systems

Addressing the great attention $Na(RE)F_4$ host materials are receiving, the developed microwave-assisted solvothermal method №1 was also extended toward Yb^{3+}/Er^{3+} co-doped β-$NaGdF_4$ and α-$NaYF_4$ (*vide infra* **Figure 23**).

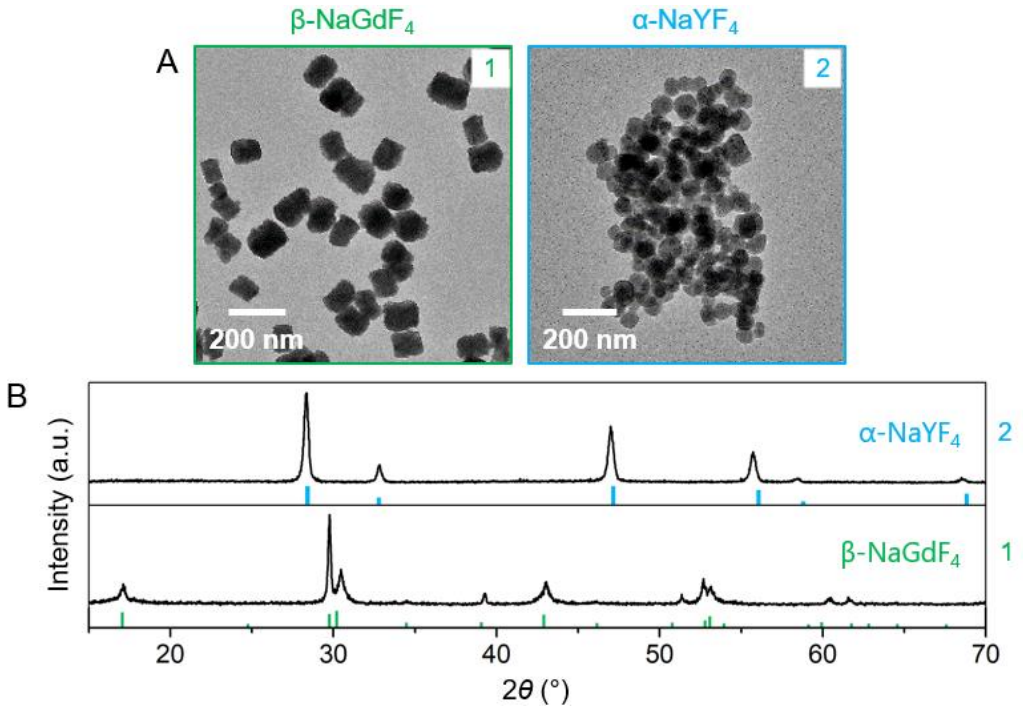

Figure 23. A) TEM micrographs of Yb^{3+}/Er^{3+} co-doped (1) β-$NaGdF_4$ nanoparticles and (2) α-$NaYF_4$ nanoparticles. B) XRD patterns of materials presented in A. References: β-$NaGdF_4$ (PDF#: 01-082-4232) and α-$NaYF_4$ (PDF#: 00-006-0342).

Unlike the Li(RE)F_4 systems reported earlier, both β-$NaGdF_4$ and α-$NaYF_4$ fall into the nanometer size range. The $NaGdF_4$:Yb^{3+}/Er^{3+} nanoparticles are 107 ± 21 nm in length and 83 ± 20 nm in width (AR = 1.3; **Figure 23-A/B-1**), and the $NaYF_4$:Yb^{3+}/Er^{3+} nanoparticles are 32 ± 7 nm in diameter (**Figure 23-A/B-2**).

To date, only a few other microwave-assisted solvothermal approaches toward β-$NaGdF_4$ have been reported to my knowledge.[79,94,118,119] The crystalline phase of the obtained $NaGdF_4$ nanoparticles constitutes an important aspect since between the two possible crystalline phases of $NaGdF_4$, α and β, the latter is generally considered as the superior host material in the context of upconversion.[120] Consequently, addition of the herein presented solvothermal approach to the limited arsenal of rapid microwave-assisted syntheses by which β-$NaGdF_4$ can be attained is highly beneficial. Furthermore, gaining significantly faster access to α-$NaYF_4$ nanoparticles in comparison to the originally adopted microwave-assisted solvothermal method requiring 3 h heat treatment at 150 °C is another merit of the developed synthesis mehtod.[92]

It is clear that the nature of the M^+ and RE^{3+} ions in the crystal lattice structure of the $M(RE)F_4$ host material has a significant effect on the overall size and morphology of the resultant particles despite being synthesized under the same reaction conditions. Most importantly, these results demonstrate that by systematic tuning of the physicochemical reaction parameters, not only does a broad range of materials become accessible, but that it is possible to significantly reduce the time required for the synthesis of a particular material.

3.4. Results and discussion (Part 2)

3.4.1. Microwave-assisted synthesis: possible challenges and solutions

Inadequate nano/microscale materials synthesis reproducibility is an implicit challenge in materials science. It has been argued that transitioning from synthesis approaches reliant on convectional heating toward those featuring microwave-induced heating can address this challenge, as microwave irradiation allows for a more homogeneous distribution of thermal energy within a reaction vessel and the accompanying computer software systems enable close monitoring of predetermined reaction parameters such as power input, reaction temperature, pressure, and duration.[77] This argument was put to test in the course of this project, and despite encountering various challenges, the results are optimistic.

In the context of this thesis, the challenges associated with solvothermal microwave-assisted synthesis became apparent only after publication of the synthesis method №1. However, as in any scientific endeavor, working past unsuspected problems revealed knowledge, which was then applied toward the development of a more reliable and rapid synthesis method (method №2). The following sections of this chapter provide insight into the potential experimental challenges associated with microwave-assisted syntheses, how they can be overcome, and how the results presented in this thesis benefited from these experimental challenges.

3.4.1.1. *Microwave reactor cavity lining and infrared temperature sensor lens: the importance of proper maintenance*

A CEM Discover SP microwave reactor was used for the synthesis of materials reported herein (**Figure 24**). This instrument has a cavity into which the reaction vessels are inserted for heat treatment. The cavity is lined with a protective material herein referred to as the cavity lining.

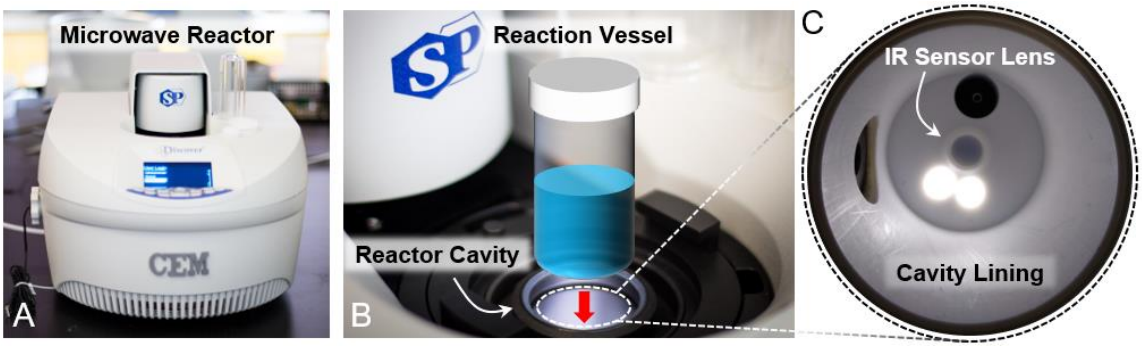

Figure 24. A) CEM Discover SP microwave reactor. B) Reactor cavity into which reaction vessels are inserted for heat treatment. C) Cavity lining (Teflon) and its infrared camera sensor lens.

The primary function of the cavity lining is to protect the interior of the reactor including the infrared (IR) camera temperature sensor from the hot contents of a reaction vessel and glass shrapnel in case of a rupturing vessel. For the reactor model used in this project, this cavity lining comes in the form of polypropylene (PP) and a more durable Teflon option.

A PP lining is suitable for relatively low operating temperatures, whereas a Teflon lining provides better cavity and IR sensor protection in the high temperature regime (above 225 °C). However, because these recommendations are optional, users often opt for the much cheaper PP option ($95 CAD) *vs.* the Teflon one ($560 CAD), regardless of their operating temperatures. As a consequence, when the respective IR sensor lenses (through which the IR sensor infers the temperature of the reaction medium) of either lining are exposed to hot reaction mixture contents (up to 300 °C) and broken glass in an event of a reaction vessel explosion, the structural integrity of the PP lens is weakened to a greater extent in comparison to the more durable Teflon lens. Nevertheless, lenses of both linings undergo structural deformation overtime, which leads to inaccurate temperature readings by the IR sensor (*vide infra* **Figure 25**). Therefore, to ensure better synthesis

reproducibility and to avoid experimental uncertainties with respect to temperature, it is necessary to use a cavity lining that is in accordance with the operating temperature conditions and to regularly inspect the structural integrity of its IR sensor lens.

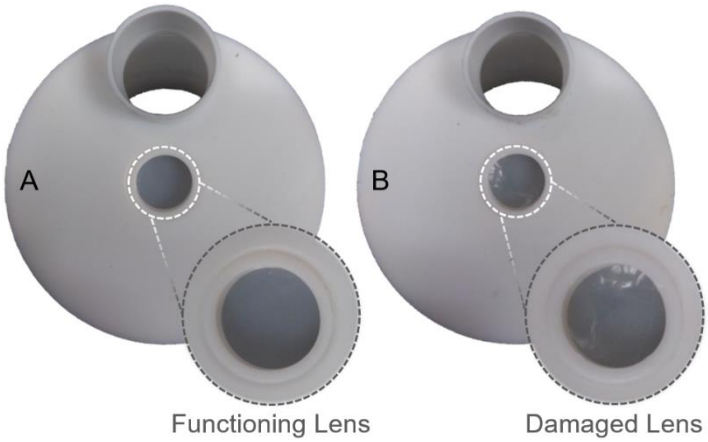

Figure 25. A) New Teflon cavity lining and IR temperature sensor lens. B) The same Teflon cavity lining and IR temperature sensor lens after sustaining repetitive damage as a result of reaction vessel explosions.

3.4.1.2. *Importance of appropriate infrared temperature sensor calibration*

In addition to a compromised IR sensor lens on a cavity lining, another factor that can introduce an element of experimental uncertainty with respect to reaction temperature conditions is an improper calibration of the reactor's IR temperature sensor.

The microwave reactor used for the synthesis of materials reported herein relies upon a one-point temperature calibration, meaning that the true temperature inside the reaction vessel is subject to increasing deviation from the temperature reading obtained by the IR sensor as the microwave temperature settings are set increasingly higher or lower than the single-point calibration temperature, respectively. Thus, the IR sensor should be calibrated in accordance with the temperature requirements of a particular synthesis method. For example, if a target temperature of 200 °C is required for a particular synthesis, the IR temperature sensor should be calibrated at or close to 200 °C.

The CEM Discover software allows for multiple calibration settings (calibration "slopes") to be saved, thus allowing the user to choose appropriate calibration settings

depending on the temperature regime required by the reaction conditions. Temperature calibrations under 100 °C can be performed with a concentrated solution of aqueous NaCl; however, oleylamine was found to be a suitable high-boiling point solvent with adequate absorption capacity of microwave radiation for temperature calibrations between 100 and 230 °C (a 50:50 v/v mixture of oleylamine and oleic acid was used as the temperature calibration medium).[XVI]

3.4.2. Synthesis method re-optimization: method №2 development

Both of the aforementioned challenges were encountered in the context of this work. More specifically, all of the physicochemical reaction parameters associated with method №1 (Li^+:RE^{3+} ratio, pH, reaction heating profile, and reaction mixture volume) were initially optimized in relationship to *i*) a PP cavity lining/IR sensor lens with a sub-optimal structural integrity and *ii*) an IR temperature sensor calibrated to 130 °C.

Firstly, the temperature calibration strategy was inadequate with respect to the temperature requirements of method №1 (210 and 200 °C in the dynamic heating method), which led to uncertainty with respect to establishing the true temperature inside the reaction vessel.[XVII] Secondly, the already poor structural integrity of the PP IR sensor lens continued to decline post-publication of method №1, eventually leading to a greater degree of temperature-reading inaccuracy and the consequent synthesis reproducibility issues. However, I am pleased to state herein that not only were these problems reconciled, but that encountering them in the first place served as an impetus toward the development of a better synthesis approach.

The significance of the new microwave-assisted method (№2) is an even shorter reaction duration – 2 min (as compared to 10 min in method №1 and ≥ 12 h in traditional

XVI Technically, 250 °C is the highest temperature at which the IR sensor can be calibrated on the CEM Discover SP reactor. However, in practice, this temperature is typically *ca*. 230 °C. This is because once the temperature of the calibrating solvent reaches 250 °C, the reactor stops supplying power. By the time the external thermocouple equilibrates to the temperature inside the reaction vessel, the temperature of the calibrating solvent has decreased to 230 °C.

XVII It was later determined that the true temperature inside the reaction vessel was lower by *ca*. 40 °C than the nominal temperature setting (*vide infra* **Section 3.4.2.3**).

autoclave-based methods). Discussed below is the step-by-step approach toward the reconciliation of the aforementioned challenges and the development of method №2. It should be noted that all experiments involved in the development of the new synthesis method were performed with undoped $LiYF_4$ as the target product. The synthesis of $LiYF_4$ microparticles with a range of RE^{3+} dopant systems *via* method №2 is presented in **Section 3.4.3**.

3.4.2.1. *Effect of infrared temperature sensor lens quality on the intra-reaction vessel temperature conditions*

The first step toward method redevelopment was to substitute the degraded PP microwave cavity lining with a more durable Teflon lining, which is better suited for the temperature range utilized in the developed synthesis method in case of repeated vessel rupture events. The effects of an improved IR camera lens quality on the temperature dynamics inside the reaction vessel were quickly realized – under the same conditions with respect to all physicochemical reaction parameters, the temperature inside the reaction vessel was not able to reach the target ramping temperature (210 °C) during the first stage of the dynamic heating method due to an excessive pressure buildup in the reaction vessel (20 bar). In such a case, when there seems to be a discrepancy between the nominal temperature setting and the true temperature inside a reaction vessel, the respective pressure reading can be used to infer the true temperature status because the temperature and pressure sensors in the utilized microwave reactor are decoupled.[XVIII]

In the case of the degraded PP lining/IR sensor lens, the pressure inside the reaction vessel was, on average, 14.6 bar at a nominal temperature value of 200 °C and 11 mL of reaction mixture (4:1:1 v/v of EtOH:H_2O:AcOH and dissolved precursors) as evident in **Figure 26-A-1/2/3** (*vide infra*).

XVIII Whereas temperature inside the reaction vessel is measured by an IR camera positioned underneath the vessel, the pressure is measured by a sensor located above the vessel, which detects the deflection of the Teflon cap.

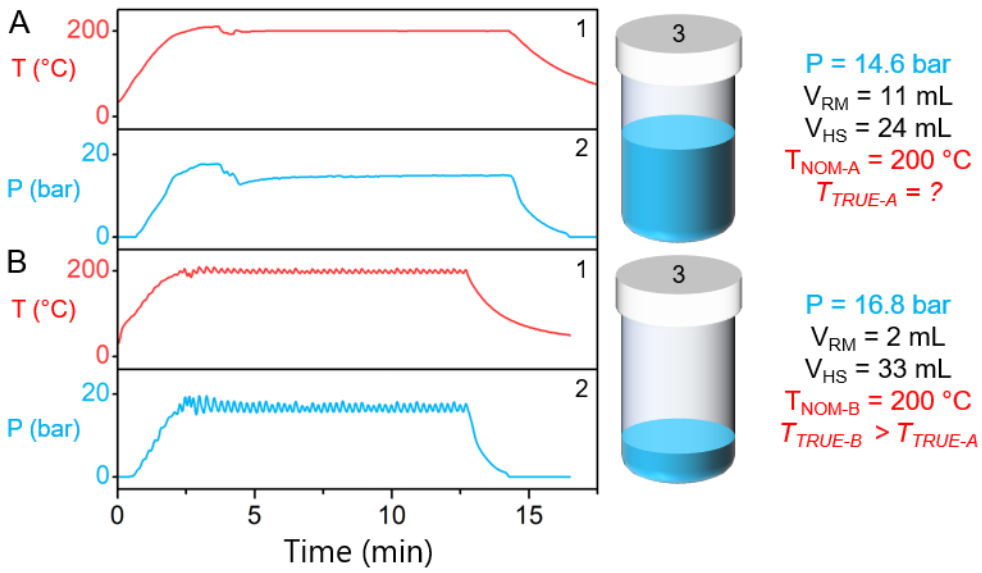

Figure 26. Temperature (1) and pressure (2) profiles of microwave-assisted syntheses performed with a degraded PP (A) and Teflon (B) reactor cavity linings/IR temperature sensors. A/B-3) Summary of physical reaction conditions. T_{NOM} – Nominal temperature settings (200 °C); T_{TRUE} – Actual temperature inside the reaction vessel; V_{RM} – Reaction mixture volume; V_{HS} – Headspace volume.

However, the volume of the same reaction mixture had to be decreased to a mere 2 mL when using a new (Teflon) cavity lining/IR sensor lens in order to allow for the same nominal temperature (200 °C) to be achieved in the reaction vessel, which was accompanied by a pressure of 16.8 bar, respectively (**Figure 26-B-1/2/3**). It should be noted that decreasing the volume of the reaction mixture from 11 to 2 mL also resulted in oscillating temperature and pressure profiles.

Because vapour pressure of a solvent in a closed system in directly proportional to its temperature (*Clausius-Clapeyron relation* – **Equation 3**, where P is the vapour pressure, ΔH is the enthalpy of vapourization, R is the ideal gas constant, T is the temperature, and C is constant),[121] results presented in **Figure 26** can only make sense if one assumes that the true temperature in the second scenario (method №2) is higher than in the first. In other words, a higher vapour pressure (16.8 *vs*. 14.6 bar) in a higher volume of empty reaction vessel headspace (33 *vs*. 24 mL; total vessel volume is 35 mL) must be associated with a higher temperature ($T_{TRUE-B} > T_{TRUE-A}$).

Eq. 3

$$\ln(P) = \frac{RT}{\Delta H} + C$$

Having clarified the change in temperature conditions, it is necessary to assess the outcome of the two syntheses. XRD patterns and SEM/TEM micrographs of the $LiYF_4$ microparticles obtained *via* the two aforementioned approaches are presented in **Figure 27** (*vide infra*). The undoped $LiYF_4$ microparticles obtained *via* the lower volume/higher temperature approach were also phase pure and within the expected size-range (*ca*. 4 µm along the longest axis) as evidenced by the XRD reflections and the TEM micrograph presented in **Figure 27-A/B-2**, respectively.

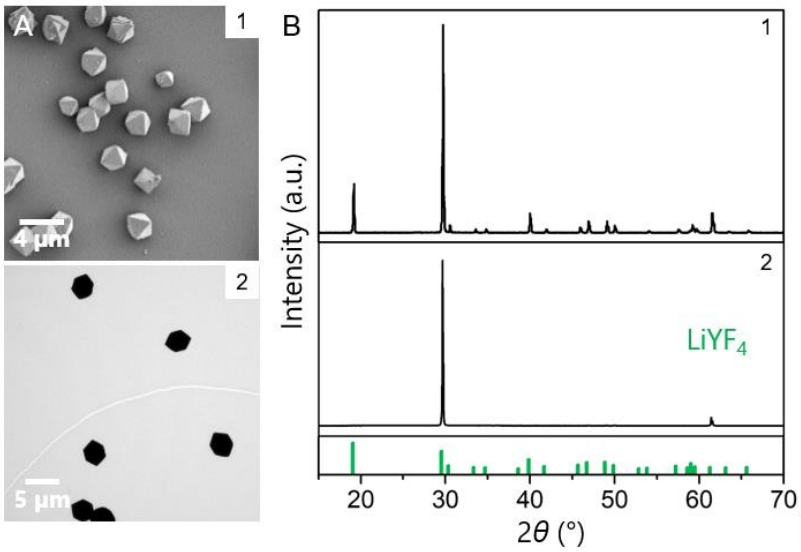

Figure 27. A/B-1) SEM micrograph and XRD pattern of Yb^{3+}(25%)/Tm^{3+}(0.5%) co-doped $LiYF_4$ microparticles obtained via method №1 and employing a damaged infrared camera sensor lens (Li^+:RE^{3+} 4.3, pH 5.3, 11 mL, 10 min, $T_{NOM\text{-}A}$ = 200 °C, $T_{TRUE\text{-}A}$ is uncertain). A/B-2) TEM micrograph and XRD pattern of undoped $LiYF_4$ microparticles obtained via a modified synthesis method employing a new Teflon infrared camera sensor (Li^+:RE^{3+} 4.3, pH 5.3, 2 mL, 10 min, $T_{NOM\text{-}B}$ = 200 °C, $T_{TRUE\text{-}B} > T_{TRUE\text{-}A}$). Reference: $LiYF_4$ (PDF#: 01-081-1940).

Overall, the observations presented in this section reveal the extent to which true temperature conditions inside a reaction vessel are influenced by the structural integrity of the IR sensor lens. In the context of this project, employing a new (not damaged) IR sensor lens allowed for a more accurate temperature reading by the IR camera sensor, thus limiting the remaining source of nominal *vs*. true temperature discrepancy to the temperature calibration approach. Furthermore, it was determined that by decreasing the reaction volume, a higher temperature regime can be targeted without surpassing the upper pressure limit (20 bar) of the instrument.

The next section delves into how such an approach can be used to further decrease the reaction duration of $LiYF_4$ microparticle synthesis.

3.4.2.2. *Shortening reaction duration from 10 to 2 min*

In **Sections 3.3.4** and **3.3.5** of this chapter, it is discussed how one can facilitate a more rapid synthesis of $LiYF_4:RE^{3+}$ microparticles by increasing the reaction temperature. More specifically, it was concluded that under the optimal $Li^+:RE^{3+}$ (4.3) and pH (5.3) conditions, a nominal reaction temperature of 200 °C and a reaction duration of 10 min was necessary to obtain phase-pure $LiYF_4:RE^{3+}$. When the temperature was lowered to a nominal value of 150 °C, the reaction duration had to be prolonged to 3 h in order to obtain $LiYF_4:RE^{3+}$ as the major phase product. The reason why the reaction temperature-duration dynamics were investigated by lowering the temperature of the static heating stage from a nominal value of 200 °C to 150 °C and prolonging the reaction duration, respectively, is because the intra-vessel pressure (stage 1 – 17 bar; stage 2 – 14.6 bar) associated with the former dynamic heating profile was already close to the upper pressure limit of the microwave reactor (20 bar) (*vide supra* **Figure 26**). Alternatively, it was demonstrated in the previous section (**Section 3.4.2.1**) that higher temperature regimes can be targeted without exceeding the upper pressure limit by lowering the reaction mixture volume. Based on the inverse reaction temperature-duration relationship established earlier, it was hypothesized that this lower volume/higher reaction temperature approach could shorten the synthesis of $LiYF_4:RE^{3+}$ microparticles beyond 10 min.

Indeed, by substituting the damaged PP cavity lining/IR sensor lens with a new Teflon cavity lining/IR sensor lens and lowering the reaction mixture volume to accommodate the resulting higher pressure/temperature regime, it was determined that the synthesis of phase-pure $LiYF_4$ microparticles can be reduced from 10 to 2 min (*vide infra* **Figure 28-C**).

Furthermore, it is evident from the XRD patterns presented in **Figure 28-A/B** that the microparticle growth mechanism likely proceeds through the same intermediary set of $Y_X(NH_4)_YF_Z$ species as described in **Section 3.3.6**, but is simply accelerated.

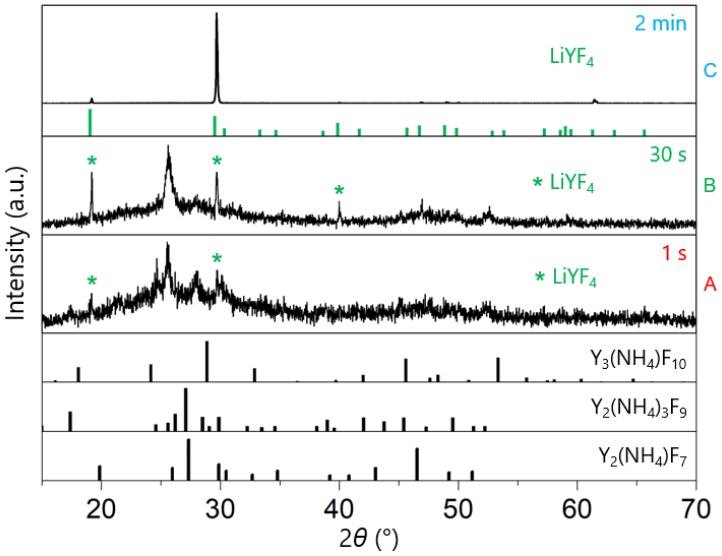

Figure 28. XRD patterns of materials obtained by microwave-assisted heating at a nominal temperature value of 200 °C for 1 s (A), 30 s (B), and 2 min (C) (pH 5.3, Li^{+}:RE^{3+} 4.3, 2 mL). A new Teflon cavity lining/IR sensor lens was employed. References: $LiYF_4$ (PDF#: 01-081-1940), $Y_3(NH_4)F_{10}$ (PDF#: 01-074-2889), $Y_2(NH_4)_3F_9$ (PDF#: 00-043-0840), $Y_2(NH_4)F_7$ (PDF#: 00-043-0847).

However, the relative intensity of the reflections attributed to the possible set of $Y_X(NH_4)_YF_Z$ phases observed in **Figure 28-A/B** differs from that observed in the previously reported mechanistic study employing a lower true reaction temperature and a longer reaction duration. This may be attributed to the difference in relative abundance of the possible $Y_X(NH_4)_YF_Z$ phases and the difference in their individual degree of crystallinity at the two different temperature regimes.

Whereas at the lower temperature regime (*vide supra* **Section 3.3.6**) $LiYF_4$ presence was observed after 5 min of heat treatment, here $LiYF_4$ formation is already detected immediately after the ramping stage toward 210 °C (duration of the following 200 °C static heating stage being only 1 s, in this case) (**Figure 28-A**). After an additional 30 s of heat treatment, reflections attributed to $LiYF_4$ become more prominent (**Figure 28-B**), and phase-pure $LiYF_4$ microparticles are obtained after 2 min, as indicated by the complete absence of reflections attributed to the set of possible $Y_X(NH_4)_YF_Z$ phases (**Figure 28-C**).

Having gained an even greater insight into the dynamic reaction temperature-duration relationship, determining the exact value of the true temperature responsible for facilitating this rapid transformation from $Y_X(NH_4)_YF_Z$ to $LiYF_4$ was necessary. The next section of

this chapter details how an appropriate calibration of the IR temperature sensor made establishing a more rigorous synthesis method with a minimal degree of uncertainty with respect to the true reaction temperature conditions possible.

3.4.2.3. *Temperature calibration*

In addition to the observed discrepancy between the nominal and true temperature conditions that occurred as a result of utilizing a damaged PP IR sensor lens, method №1 employed a nominal temperature setting (200 °C) that was established based on an incorrect IR temperature sensor calibration procedure. More specifically, the one-point temperature calibration was performed at 130 °C using ethylene glycol as the solvent, which means that the discrepancy between the true temperature inside the reaction vessel and the temperature reading provided by the IR sensor was relatively high at the operating temperature (nominal value of 200 °C). To determine the extent of this discrepancy, but more importantly to pinpoint the true, *i.e.*, more accurate, temperature value that is responsible for facilitating the 2-min synthesis of $LiYF_4$ microparticles, the following experiment was conducted.

To eliminate the discrepancy associated with a damaged PP IR sensor lens, the experiment employed the new (Teflon) cavity lining/IR sensor lens. First, the IR temperature sensor was re-calibrated at 130 °C with ethylene glycol (calibration slope – 2.2311), and at 230 °C with a 50:50 v/v mixture of oleic acid and oleylamine (calibration slope – 1.7107).[XIX] Then, multiple 2-min reactions with increasing temperature profiles were conducted under each of the two calibration settings (all other variables kept constant). Temperature settings of the static heating stage that facilitated a timely phase transformation from $Y_X(NH_4)_YF_Z$ to $LiYF_4$ were determined to be 220 °C and 180 °C for the 2.2311 (calibrated at 130 °C) and 1.7107 (calibrated at 230 °C) calibration slopes, respectively. Remarkably, these results exemplify the extent to which the nominal temperature value can differ from the true, *i.e.*, more accurate, temperature inside the

[XIX] Oleylamine absorbs microwave radiation more readily as compared to ethylene glycol and oleic acid. Thus, it is a better solvent choice for temperature calibrations in the 200-300 °C range.

reaction vessel based on the calibration strategy. In this case, both settings yielded phase-pure $LiYF_4$ microparticles in the same amount of time, meaning that although the nominal temperature values differed by 40 °C (220 *vs*. 180 °C), the true temperature conditions were similar (*ca*. 180 °C). The similarity between the two true temperature conditions (*ca*. 180 °C) fostered by the two different nominal temperature settings (220 *vs*. 180 °C) is evidenced by the fact that the accompanying pressure profiles are quite similar – 14 bar for the nominal temperature value of 220 °C and 16 bar for the nominal temperature value of 180 °C (*vide infra* **Figure 29**). The validity of this conclusion is grounded in the fact that the temperature and pressure sensors of the microwave reactor are decoupled. This allows one to infer the true temperature conditions inside the reaction vessel *via* the respective pressure output. It should be noted that the reaction conditions involving Li^+:RE^{3+} 4.3, pH 5.3, 2 mL, 2 min, and 180 °C comprise method №2.

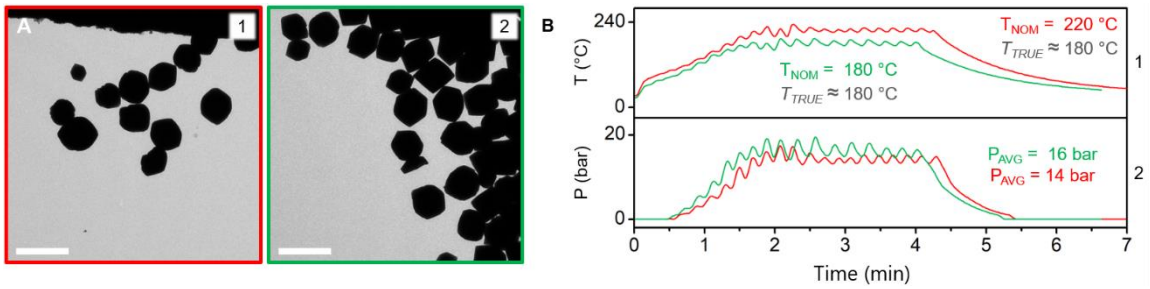

Figure 29. A) TEM micrographs of $LiYF_4$ microparticles synthesized at nominal temperature values of (1) 220 °C and (2) 180 °C (Li^+:RE^{3+} 4.3, pH 5.3, 2 mL, 2 min). Scale bars: 2 μm. B) Respective reaction 1) temperature and 2) pressure profiles. Nominal temperature settings of 220 °C (calibration slope – 1.7107; calibrated at 130 °C) and 180 °C (calibration slope – 2.2311; calibrated at 230 °C) both correspond to a "true" temperature value of *ca*. 180 °C. Reaction conditions involving Li^+:RE^{3+} 4.3, pH 5.3, 2 mL, 2 min, and 180 °C comprise method №2.

3.4.3. Extending method №2 toward $LiYF_4$:RE^{3+} microparticles

As already mentioned in **Section 3.3.1**, method №2 was also extended toward $LiYF_4$:Yb^{3+}(18%)/Er^{3+}(2%) (*vide supra* **Figures 11** and **12**). Furthermore, a series of $LiYF_4$ microparticle systems featuring a range of Nd^{3+} concentrations (2.5-25%, 2.5% increments) was also obtained *via* this lower volume/higher temperature approach. However, a longer reaction duration was necessary to foster the phase transformation of

the *in-situ* generated intermediary $Y_X(NH_4)_YF_Z:Nd^{3+}$ species into $LiYF_4:Nd^{3+}$. More specifically, an increase in reaction duration from 2 to 20 min was necessary to achieve the synthesis of phase-pure $LiYF_4$ microparticles with a Nd^{3+} doping concentration between 2.5 and 12.5%. Interestingly, a further increase in reaction duration from 20 to 30 and 60 min in an attempt to target phase-pure $LiYF_4$ with a Nd^{3+} doping concentration of 17.5% and 20-25%, respectively, was not effective.

Presence of the $Y_X(NH_4)_YF_Z:Nd^{3+}$ co-phase alongside $LiYF_4:Nd^{3+}$ was detected *via* SEM (*vide supra* **Figure 11**) in all samples featuring a nominal Nd^{3+} doping concentration ranging from 15 to 25%. Furthermore, XRD patterns (*vide supra* **Figure 12-13/14**) corresponding to $LiYF_4$ microparticles doped with a nominal Nd^{3+} concentration ranging from 20 to 25% feature a low resolution, and very low intensity reflection centered at *ca*. 25 ° 2θ that is characteristic of $Y_X(NH_4)_YF_Z$. Presence of Nd^{3+} in $Y_X(NH_4)_YF_Z$ was confirmed by means of EDS (*vide infra* **Figure 30**).

These results suggest that thermal stability of the intermediary $Y_X(NH_4)_YF_Z:Nd^{3+}$ species increases as a function of Nd^{3+} content. It is possible that a further increase in reaction temperature may facilitate the complete phase transformation from $Y_X(NH_4)_YF_Z:Nd^{3+}$ to $LiYF_4:Nd^{3+}$. However, targeting an even higher temperature regime by means of further decreasing the reaction mixture volume is not advisable since a reaction mixture volume below 2 mL would create a safety hazard when utilizing a 35 mL reaction vessel. More importantly, presence of Nd^{3+} in $Y_X(NH_4)_YF_Z$ indicates that the true doping concentration of Nd^{3+} in $LiYF_4$ microparticles with nominal Nd^{3+} doping concentration between 15% and 25% may be lower. However, this can be only confirmed if the respective microparticles can be separated from the $Y_X(NH_4)_YF_Z$ phase and subjected to elemental analysis *via* ICP-MS. Until then, the established synthesis method should be limited to targeting $LiYF_4:Nd^{3+}$ systems with a Nd^{3+} concentration equal or lower than 12.5% (out of all the $LiYF_4:Nd^{3+}$(X%) reported herein).

Only 5, 15, and 25% Nd^{3+}-doped $LiYF_4$ samples were subjected to single-particle luminescence characterization (*vide infra* **Section 4.3.2.1**). For this, very dilute microparticle dispersions (*ca*. 0.025 mg/mL) were drop-casted onto glass slides and dried. Thus, any presence of the $Y_X(NH_4)_YF_Z:Nd^{3+}$ phase was considered to be negligible.

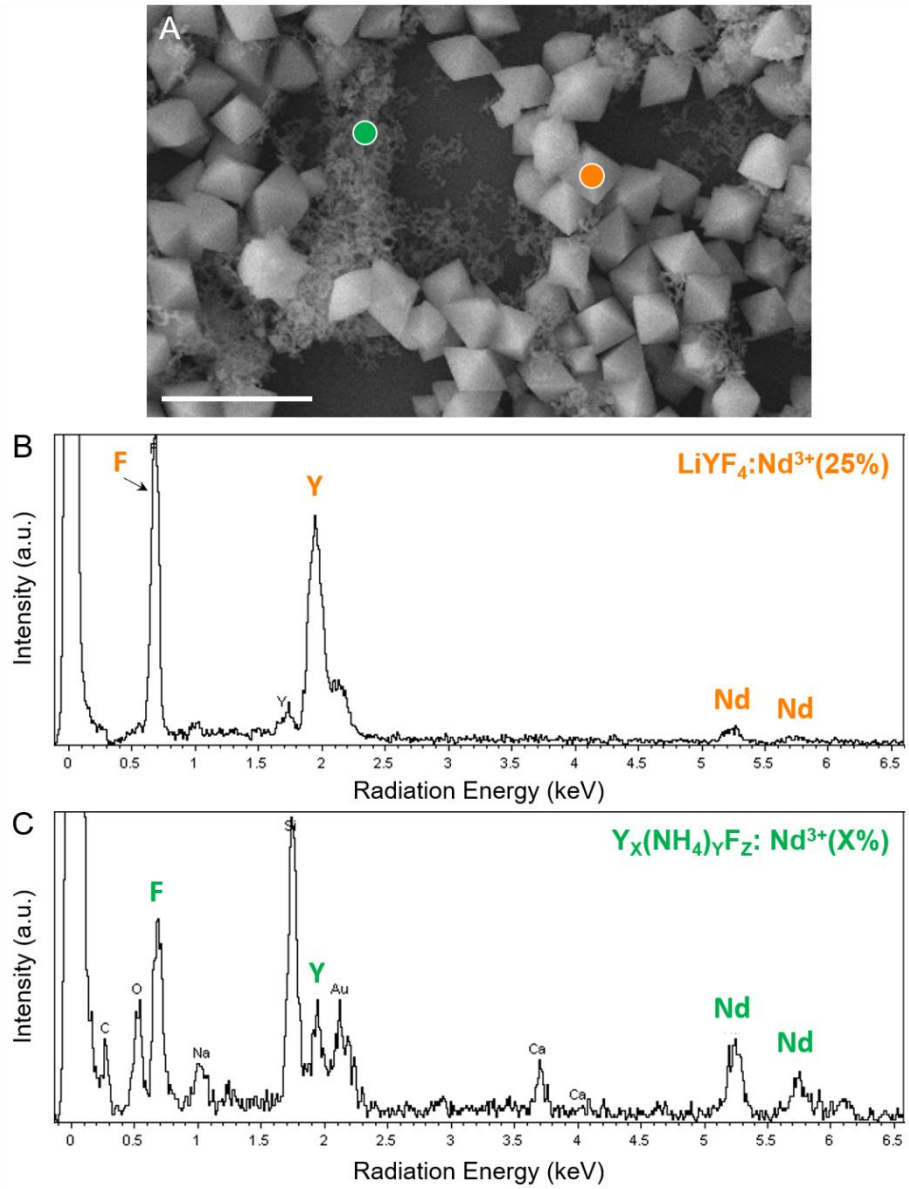

Figure 30. A) SEM micrograph of a sample containing $LiYF_4$ microparticles (orange) with a nominal Nd^{3+} doping concentration of 25% and $Y_X(NH_4)_YF_Z:Nd^{3+}$ as the secondary phase (green) with an unknown Nd^{3+} doping concentration. Areas of the sample subjected to EDS are indicated by the coloured circles. Scale bar: 5 µm. B/C) EDS spectra of a $LiYF_4:Nd^{3+}$ microparticle and $Y_X(NH_4)_YF_Z:Nd^{3+}$, respectively. Main elemental constituents of both materials are indicated. The glass substrate is likely the source of the detected elements such as C, O, Na, and Ca; whereas Au arises from the Au-sputtered sample.

Furthermore, the respective luminescence characterization study merely required $LiYF_4$ microparticles with different Nd^{3+} doping concentrations, and knowing the exact Nd^{3+} concentration was not a prerequisite.

3.5. Summary of Chapter 3

Chapter 3 detailed the development of a microwave-assisted solvothermal approach toward $LiYF_4:RE^{3+}$ microparticles by means of optimizing a set of important physicochemical reaction parameters: $Li^+:RE^{3+}$ ion ratio, reaction mixture pH, reaction temperature/duration profile, and reaction mixture volume. **Table 5** provides a summary of all physicochemical reaction parameters subjected to the initial investigation as well as the resulting materials.

Table 5. Overview of all reaction parameters subjected to investigation (reaction mixture (RM) volume), pH, temperature, $Li^+:RE^{3+}$ ratio, and reaction duration) as well as the phase and morphology of the resulting products. Optimal reaction conditions yielding $LiYF_4$ microparticles are highlighted (method №1 – Red, method №2 – Green). Phase identification of materials denoted by "Nanoparticles" and "-" was not possible.

RM Volume (mL)	pH	Temp. (° C)	$Li^+:RE^{3+}$ Ratio	Duration (min) | (h)	Phase	Morphology
11	2.0	200	4.3	10	YF_3	Irregular
	5.3	150	2.0	10	"Nanoparticles"	Spherical
				3	$Y_3(NH_4)F_{10}$ $LiYF_4$	- Bipyramidal
			4.3	10	"Nanoparticles"	Spherical
				3	$LiYF_4$ $Y(OH)_XF_Y$	Bipyramidal Rods
			7.5	10	$Y(OH)_XF_Y$ LiF	Rods -
				3	$Y(OH)_XF_Y$ $LiYF_4$ LiF	Rods Bipyramidal -
		200	2.0	10	$Y_3(NH_4)F_{10}$ "Nanoparticles"	- Spherical
			4.3	10	$LiYF_4$	Bipyramidal
			7.5	10	$Y(OH)_XF_Y$ LiF	Rods -
	7.5	200	4.3	10	-	-
2	5.3	180	4.3	2	$LiYF_4$	Bipyramidal

Method №1 ($Li^+:RE^{3+}$ 4.3, pH 5.3, 11 mL, 200 °C, 10 min) was developed to target $LiYF_4$ microparticles featuring the Yb^{3+}(18%)/Er^{3+}(2%) and Yb^{3+}(25%)/Tm^{3+}(0.5%)

dopant systems for upconversion as well as the Ce^{3+}(2%)/Tb^{3+}(2%) dopant system for downshifting luminescence. Method №1 was also extended toward the synthesis of upconverting $LiYbF_4$:Er^{3+}(2%) microparticles as well as α-$NaYF_4$ and β-$NaGdF_4$ nanoparticles co-doped with Yb^{3+}(18%)/Er^{3+}(2%).

Further optimization of method №1 led to the development of a shorter synthesis route (method №2 – Li^+:RE^{3+} 4.3, pH 5.3, 2 mL, 180 °C, 2 min) toward undoped $LiYF_4$ microparticles and those featuring the Yb^{3+}(18%)/Er^{3+}(2%) dopant system. Subsequently, increasing the reaction duration of method №2 from 2 to 20, 30, and 60 min allowed for the synthesis of downshifting $LiYF_4$ microparticles doped with 2.5-15% Nd^{3+}, 17.5% Nd^{3+}, and 20.0-25% Nd^{3+}, respectively.

Figure 31 (*vide infra*) provides a visual summary of the information presented in **Table 5** and also identifies the reaction conditions used to obtain all of the M(RE)F_4:RE^{3+} (M; Li and Na; RE: Y, Ce, Nd, Gd, Tb, Er, Tm, and Yb) materials discussed in this thesis.

Lastly, the mechanism by which $LiYF_4$:RE^{3+} microparticles form was unveiled, and a critical review of potential challenges associated with microwave-assisted synthesis was provided along with possible solutions. The next chapter of this thesis details a thorough optical characterization of the herein discussed materials, and special attention is devoted to single-particle optical characterization of the $LiYF_4$:RE^{3+} systems.

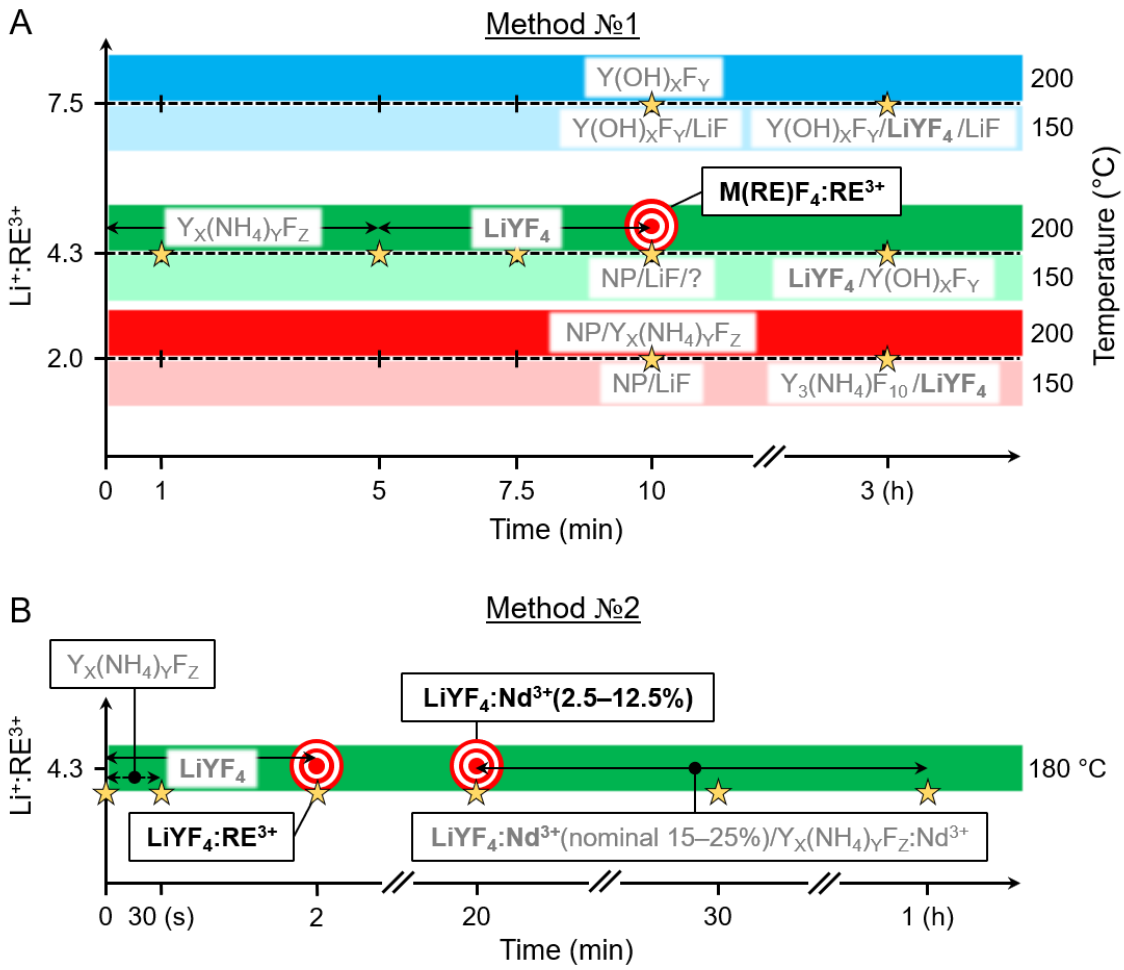

Figure 31. A) Schematic representation of method №1 development. The optimal set of reaction parameters for targeting $LiYF_4:RE^{3+}$ (RE combinations: Yb^{3+}/Er^{3+}, Yb^{3+}/Tm^{3+}, and Ce^{3+}/Tb^{3+}), $LiYbF_4:Er^{3+}$, α-$NaYF_4:RE^{3+}$ and β-$NaGdF_4:RE^{3+}$ (RE: Yb^{3+}/Er^{3+}) is indicated by the bullseye. B) Schematic representation of method №2 development. The optimal sets of reaction parameters for targeting $LiYF_4:RE^{3+}$ (RE combinations: undoped and Yb^{3+}/Er^{3+}) and phase-pure $LiYF_4:Nd^{3+}$(2.5–12.5%, 2.5% increments) are indicated by the bullseyes, respectively. All of the indicated reaction conditions were investigated under the initial reaction mixture pH of 5.3. Stars denote reaction conditions that were subjected to investigation.

Chapter 4. Luminescence characterization of the RE^{3+}-doped (RE^{3+}: Yb^{3+}/Tm^{3+}, Yb^{3+}/Er^{3+}, Ce^{3+}/Tb^{3+}, and Nd^{3+}) $LiYF_4$ and Er^{3+}-doped $LiYbF_4$ microparticles, as well as the Yb^{3+}/Er^{3+}-doped $Na(RE)F_4$ (RE: Y, Gd) nanoparticles

4.0. Introduction

Having gained access to a set of $M(RE)F_4:RE^{3+}$ materials featuring both upconverting and downshifting dopant systems, their luminescence was assessed either *via* a fluorescence microscopy setup equipped with a hyperspectral imaging system or a UV/Vis fluorometer, respectively. Characteristic upconverted emission was analyzed by probing the average emission stemming from many particles in drop-casted samples of $LiYF_4:Yb^{3+}/Tm^{3+}$, $LiYF_4:Yb^{3+}/Er^{3+}$, and $LiYbF_4:Er^{3+}$ microparticles, as well as α-$NaYF_4:Yb^{3+}/Er^{3+}$ and β-$NaGdF_4:Yb^{3+}/Er^{3+}$ nanoparticles. Characteristic downshifting luminescence of the $LiYF_4:Ce^{3+}/Tb^{3+}$ microparticles was analyzed by probing the average emission stemming from many particles suspended in dispersion. Upconversion luminescence of the $LiYF_4$ microparticles featuring the Yb^{3+}/Er^{3+} and Yb^{3+}/Tm^{3+} dopant systems was also analyzed at a single-particle level *via* hyperspectral imaging. Lastly, drop-casted samples of the upconverting $LiYF_4:Yb^{3+}/Er^{3+}$ and $LiYF_4:Yb^{3+}/Tm^{3+}$, as well as the downshifting $LiYF_4:Nd^{3+}$(5%, 15%, 25%) microparticles were subjected to a single-particle polarized emission study, while a single $LiYF_4:Yb^{3+}/Er^{3+}$ microparticle was also subjected to a single-particle polarized emission study inside an optical trap.

The first objective of this chapter is to provide a general overview of the characteristic luminescence properties of the synthesized $M(RE)F_4:RE^{3+}$ systems. The second objective is to provide a plausible explanation for the non-uniform spatial distribution of emission intensity stemming from individual $LiYF_4:RE^{3+}$ microparticles.

4.1. Experimental details and characterization techniques

4.1.1. Optical characterization of the upconverting Yb^{3+}/Er^{3+} and Yb^{3+}/Tm^{3+} co-doped $M(RE)F_4$ systems

Spectroscopic analysis was performed using a custom-built hyperspectral microscope (IMA Upconversion™ by PhotonEtc, Montreal, Canada; **Figure 32**).

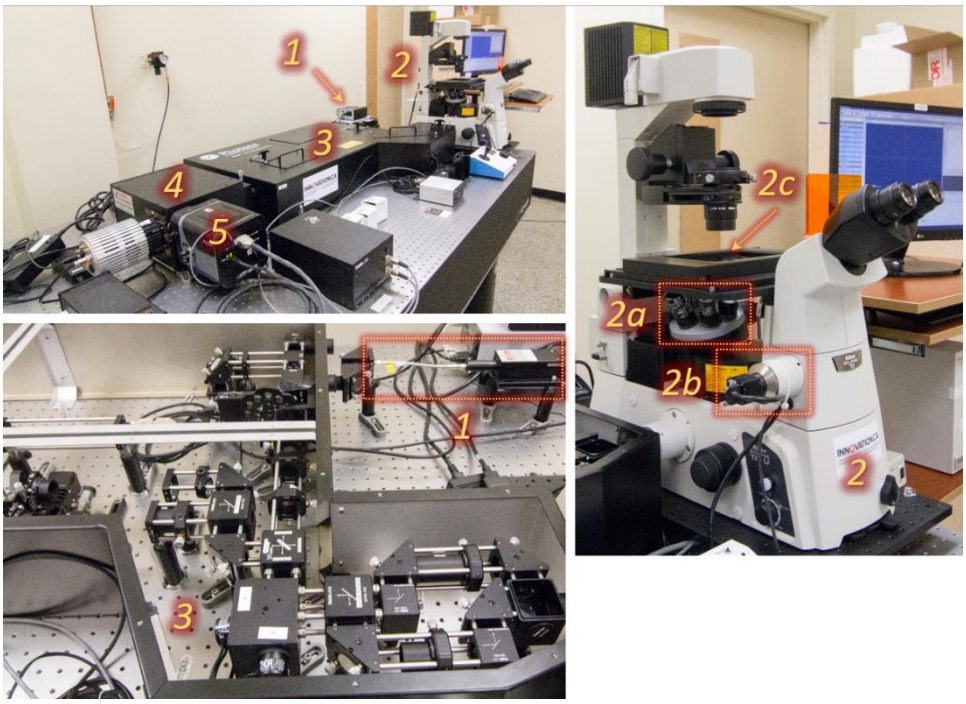

Figure 32. Custom-built fluorescence microscope (capable of hyperspectral imaging) used for the optical characterization of the $M(RE)F_4:RE^{3+}$ systems. (1) 980 nm diode laser, (2) inverted optical microscope, (2a) microscope objectives, (2b) broadband camera, (2c) microscope stage, (3) confocal/hyperspectral module (galvanometer mirrors), (4) monochromator, (5) EMCCD camera.

As depicted in **Figure 32**, the microscope is equipped with (*1*) a 980 nm diode laser, (*2*) an inverted optical microscope (Nikon Eclipse Ti-U) with (*2a*) microscope objectives (*e.g.*, 20×, 0.40 NA and 60×, 0.85 NA, Nikon), (*2b*) a broadband camera for colour imaging of samples at (*2c*) the microscope stage, (*3*) a set of galvanometer mirrors, (*4*) a Princeton Instruments SP-2360 monochromator, and (*5*) a Princeton Instruments ProEM EMCCD camera for detection of visible emission.

Upconversion emission spectra were obtained on dried particle films drop-casted[XX] onto glass slides. Optical characterization of $M(RE)F_4:RE^{3+}$ nano/microparticles not involved in hyperspectral imaging studies was performed on relatively thick particles films (glass substrate not visible), and a 20× (0.40 NA) microscope objective was utilized. Hyperspectral imaging was performed on monolayers of the Yb^{3+}/Er^{3+} and Yb^{3+}/Tm^{3+} co-doped $LiYF_4$ microparticles obtained by drop casting a more dilute particle dispersion. Mapping of the upconverted visible emission was accomplished by scanning a selected area (*ca*. 30 μm × 30 μm) of the respective glass slide, and the emission stemming from individual particles was probed by selecting an area of interest of the hyperspectral cube generated by the PHySpecV2 software. For the $LiYF_4:Yb^{3+}/Er^{3+}$ system, the green (510–570 nm) and red (627–682 nm) emission bands were probed. For the $LiYF_4:Yb^{3+}/Tm^{3+}$ system, the blue (440–500 nm), red (622–677 nm), and NIR (754–805 nm) emission bands were probed.

For the hyperspectral imaging study, a microscope objective with a higher magnification (60×) and numerical aperture (0.85 NA) was used to better visualize individual microparticles and to ensure that the resulting laser spot size (*ca*. 1.45 μm in diameter) was smaller than the probed microparticles ($LiYF_4:Yb^{3+}/Er^{3+}$ – 4.4 ± 0.4 μm × 4.0 ± 0.2 μm, $LiYF_4:Yb^{3+}/Tm^{3+}$ – 3.8 ± 0.4 μm × 3.3 ± 0.2 μm). Under these conditions, power density at the sample was in the range of 4.0–4.7 × 10^8 mW/cm^2 during mapping. Data analysis and plotting were performed with the microscope's PHySpecV2 software and OriginPro.

4.1.2. Optical characterization of the downshifting $LiYF_4:Ce^{3+}/Tb^{3+}$ system

Optical properties of the Ce^{3+}/Tb^{3+} co-doped $LiYF_4$ microparticles, dispersed in ethanol (mass concentration *ca*. 0.2 mg/mL) and transferred into a quartz cuvette, were investigated using a Photon Technology International fluorimeter equipped with a xenon lamp. The excitation spectrum of Ce^{3+} in the $LiYF_4$ host matrix was retrieved by plotting the intensity of the Tb^{3+} emission signal centered at 490 nm ($^5D_4 \rightarrow {}^7F_6$ Tb^{3+} transition) against the

[XX] In the context of this work, drop-casting was always followed by drying of the respective solvent in order to obtain a dry film of particles (or a monolayer, depending on the concentration of the particle dispersion).

respective excitation wavelength (275-315 nm in 5 nm intervals). Based on the results of excitation spectroscopy, 295 nm was then used as the excitation wavelength to obtain the downshifting emission spectrum of Ce^{3+}/Tb^{3+} co-doped $LiYF_4$ microparticles. A photograph of the green-emitting sample under illumination with UV irradiation (280-400 nm) produced by a Luzchem LZC 4V photoreactor equipped with eight UV lamps was obtained by inserting a Chroma AT560/40× band-pass filter (541-583 nm) between the sample and the camera. Data analysis and plotting were performed with the fluorometer's PTI FeliX32 software and OriginPro.

4.1.3. Optical trapping

Optical trapping and all other optical studies enabled by optical trapping of single $LiYF_4:Yb^{3+}(18\%)/Er^{3+}(2\%)$ microparticles were performed using a custom-built microscope provided by the Fluorescence Imaging Group of the Universidad Autónoma de Madrid (*vide infra* **Figure 33**).

For sample preparation, an aqueous dispersion of the $LiYF_4:Yb^{3+}(18\%)/Er^{3+}(2\%)$ microparticles (*ca*. 0.025 mg/mL) was deposited into a microchamber created by adhering a secure seal spacer (height – 120 μm, diameter – 13 mm; Electron Microscopy Sciences, Cat. #70327-13S) between a microscope slide and a cover glass slide. The microchamber was placed onto the (*1*) microscope stage. (*2*) A linearly polarized laser beam stemming from a fiber-coupled, continuous-wave, single-mode 975 nm diode laser (Lumics, LU0975M500) was tightly focused into the microchamber by (*3*) a high numerical aperture, oil-immersion microscope objective (100×, 1.40 NA; Olympus). The Brownian motion of microparticles inside the microchamber was monitored with (*4*) a CMOS camera (Thorlabs) coupled to the microscope setup, and trapping of a single particle was achieved by moving the microscope stage in the *xy* plane in a way that brings the particle in close proximity to the laser's focal point. Radiation stemming from the laser source was first collimated by (*5*) a mounted fiber-port (Thorlabs, PAF-X-7-B) and then expanded to a beam *ca*. 2 mm in diameter by a 2× beam expander (Thorlabs, BE02M).

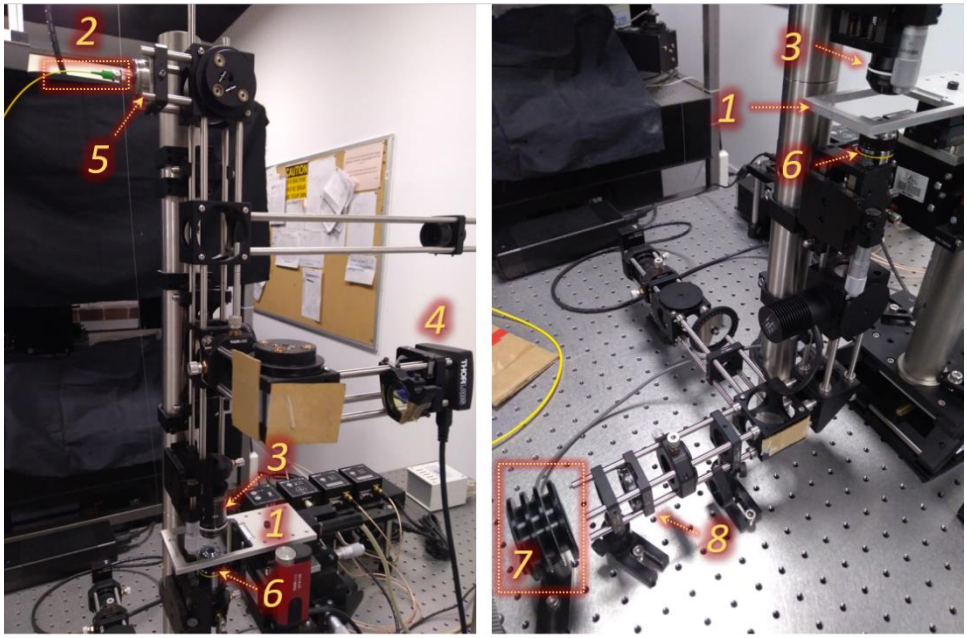

Figure 33. Custom-built microscope used to conduct the single-particle polarized emission spectroscopy study with a $LiYF_4:Yb^{3+}/Er^{3+}$ microparticle inside an optical trap. (1) Microscope stage and microchamber, (2) fiber-coupled 790 or 975 nm diode laser, (3) 100×, 1.40 NA microscope objective for focusing laser, (4) CMOS camera, (5) collimator and beam expander, (6) 0.25 NA microscope objective for collecting emission, (7) power meter (for spectroscopic studies, a monochromator/CCD was coupled in this position), (8) linear polarizer.

Considering the numerical aperture of the microscope objective utilized, the resulting wavelength-dependent laser spot diameter at the focal point inside the microchamber was calculated to be 836 nm. Laser power at the stage was measured to be 165 mW by a Coherent, Lasercheck (ROHS) power meter. Changes in particle orientation inside the optical trap with respect to the propagation direction of the incident laser were induced by manipulating the laser focus. With appropriate modifications (*vide infra*), this setup was used to conduct single-particle polarized emission spectroscopy experiments involving individual microparticles optically trapped in various spatial orientations.

4.1.4. Single-particle polarized emission spectroscopy

Single-particle polarized emission spectroscopy studies were performed on optically trapped microparticles as well as those drop-casted onto a glass substrate. For the former

approach, after optically trapping, properly orienting and exciting individual $LiYF_4:Yb^{3+}(18\%)/Er^{3+}(2\%)$ microparticles with 975 nm laser radiation, their emission was collected by (*6*) a 0.25 NA microscope objective and guided to (*7*) a portable monochromator (Ocean Optics, QE65000) through (*8*) a linear polarizer (Thorlabs, LPNIR050-MP2) positioned in 36 radial orientations (0° to 350°; 10° intervals). Four spatial particle orientations inside the optical trap were analyzed, and a total of three particles were investigated. In total, 36 spectra were obtained per particle orientation (one spectrum for each radial linear polarizer orientation). To assess the degree of polarization of the emission stemming in a particular direction relative to the optic axis of a single $LiYF_4:Yb^{3+}/Er^{3+}$ microparticle (*i.e.*, emission stemming in a particular direction from a microparticle optically trapped in one of the four spatial orientations), a polar plot depicting the intensity ratio between two specific Er^{3+} emission bands as a function of the linear polarizer angle was constructed. A polar plot was constructed for each of the four spatial particle orientations. This was done for three different particles, and the respective polar plots (each corresponding to one particular spatial particle orientation) were averaged. Data analysis and plotting were performed with OceanView 1.6.3 (Lite) software and OriginPro.

The single-particle polarized emission spectroscopy study of the drop-casted samples was performed with a different (confocal) microscope (also provided by the Fluorescence Imaging Group). This confocal microscope was equipped with the same components as the microscope used for optical trapping, with some exceptions. A 790 nm diode laser (Lumics, SN0704476) was used for the excitation of $LiYF_4:Nd^{3+}(X\%)$ microparticles and a high-resolution monochromator (iH320, Horiba) coupled to a CCD camera (Synapse, Horiba) was used for detection of visible and NIR emission. In this approach, individual microparticles out of the following samples: $LiYF_4:Yb^{3+}(18\%)/Er^{3+}(2\%)$, $LiYF_4:Yb^{3+}(25\%)/Tm^{3+}(0.5\%)$, and $LiYF_4:Nd^{3+}$(5, 15, and 25%) were probed. Because these particles were drop-casted onto a flat glass substrate, only one out of the four possible particle orientations was studied (top triangular facet parallel to the substrate; orientation 1, as reported in **Section 4.3.2.2**). In total, 36 spectra were recorded per particle, corresponding to the 36 radial orientations of the linear polarizer. A total of three particles were investigated for each dopant system. The same approach to data analysis was undertaken as in the case of single-particle polarized emission spectroscopy performed on

optically trapped particles. Data analysis and plotting were performed with the microscope's LabSpec6 software and OriginPro.

4.2. Results and discussion (Part 1)

4.2.1. Optical characterization of the downshifting $LiYF_4$ Ce^{3+}/Tb^{3+} microparticles

Excitation and emission spectra of the Ce^{3+}/Tb^{3+} co-doped $LiYF_4$ microparticles are presented in **Figure 34-A** (*vide infra*), and the energy level diagram of the respective Ce^{3+}/Tb^{3+} downshifting dopant system is presented in **Figure 34-C** (electronic transitions responsible for the observed emission bands are indicated).

From **Figure 34-A** it is evident that the best sensitization of Tb^{3+} emission is achieved under 295 nm excitation. Indeed, upon UV excitation, Ce^{3+} undergoes a Laporte-allowed 4f → 5d electronic transition, and an energy transfer then follows from the 5d excited state of Ce^{3+} to the ^5H_J states of Tb^{3+}.[32,33] Non-radiative relaxation down to the Tb^{3+} $^5D_4$ emitting level is then facilitated, from which radiative relaxation down to the $^7F_6$ (490 nm), $^7F_5$ (545 nm), $^7F_4$ (580 nm), and $^7F_3$ (621 nm) energy levels takes place, producing four characteristic Tb^{3+} emission bands.[29]

In order to provide some experimental evidence for the existence of an energy transfer from Ce^{3+} to Tb^{3+} in $LiYF_4$:Ce^{3+}/Tb^{3+}, $LiYF_4$ microparticles singly doped with 2 mol% Tb^{3+} were also synthesized *via* method №1, and their luminescence was compared to that of $LiYF_4$:Ce^{3+}/Tb^{3+} (*vide infra* **Figure 35**). **Figure 35-C/D** shows the emission spectra obtained on both particle dispersions (concentration: 0.2 mg/mL) under 295 nm excitation. It is evident that under identical experimental conditions, emission intensity generated by $LiYF_4$:Tb^{3+} is much weaker as compared to that of $LiYF_4$:Ce^{3+}/Tb^{3+}. These results corroborate that Ce^{3+} facilitates efficient sensitization of Tb^{3+} emission.[32]

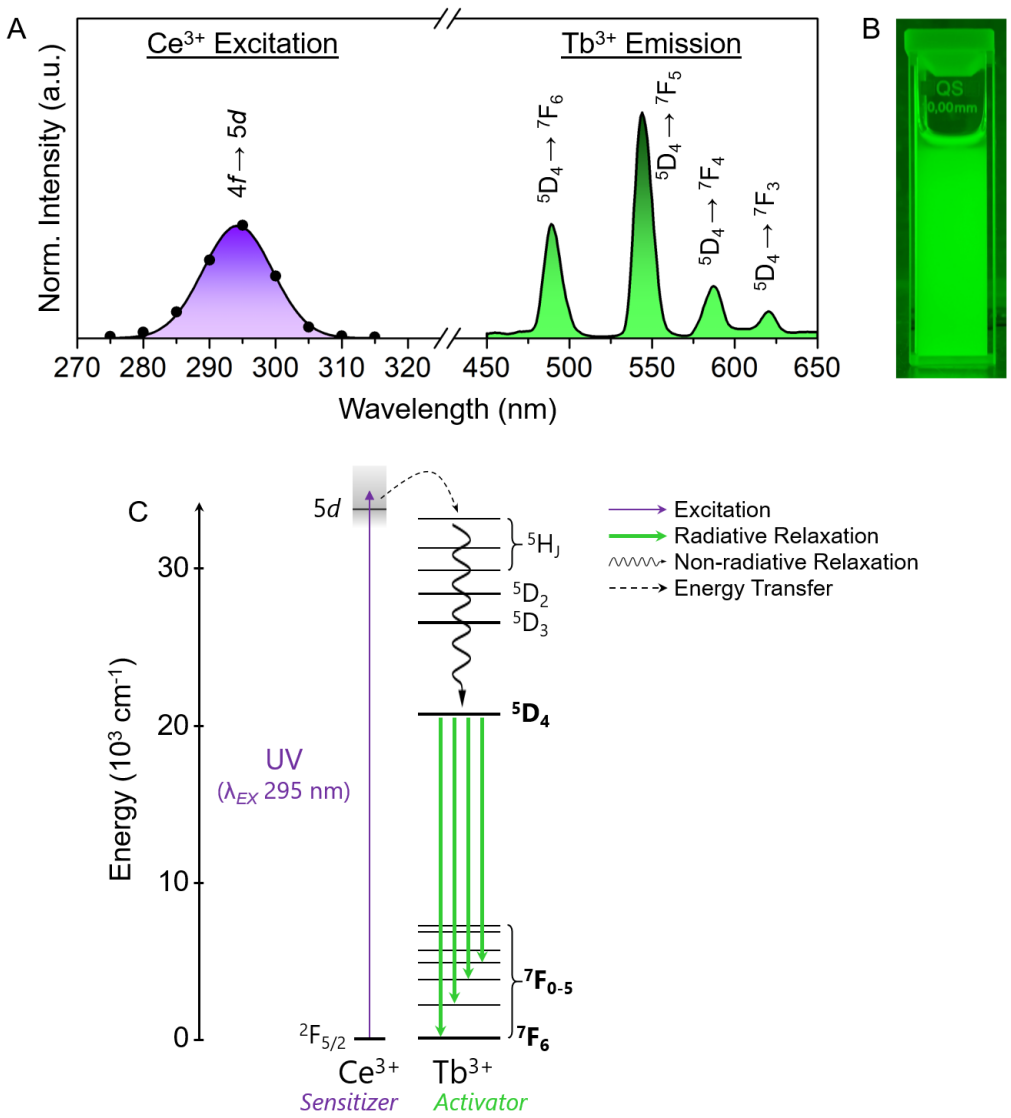

Figure 34. A) An excitation spectrum of Ce^{3+} in the $LiYF_4$ host matrix and a downshifting emission spectrum of the Ce^{3+}/Tb^{3+} co-doped $LiYF_4$ microparticles under 295 nm excitation. B) Photograph showing the green downshifted emission of the Ce^{3+}/Tb^{3+} co-doped $LiYF_4$ microparticles under broad-band UV excitation (280-400 nm). A band pass filter (541-583 nm) was used to acquire the photograph. C) Energy level diagram of the Ce^{3+}/Tb^{3+} downshifting dopant system depicting the electronic transitions that are responsible for the observed emission (relevant energy levels and their respective term symbols are in bold).

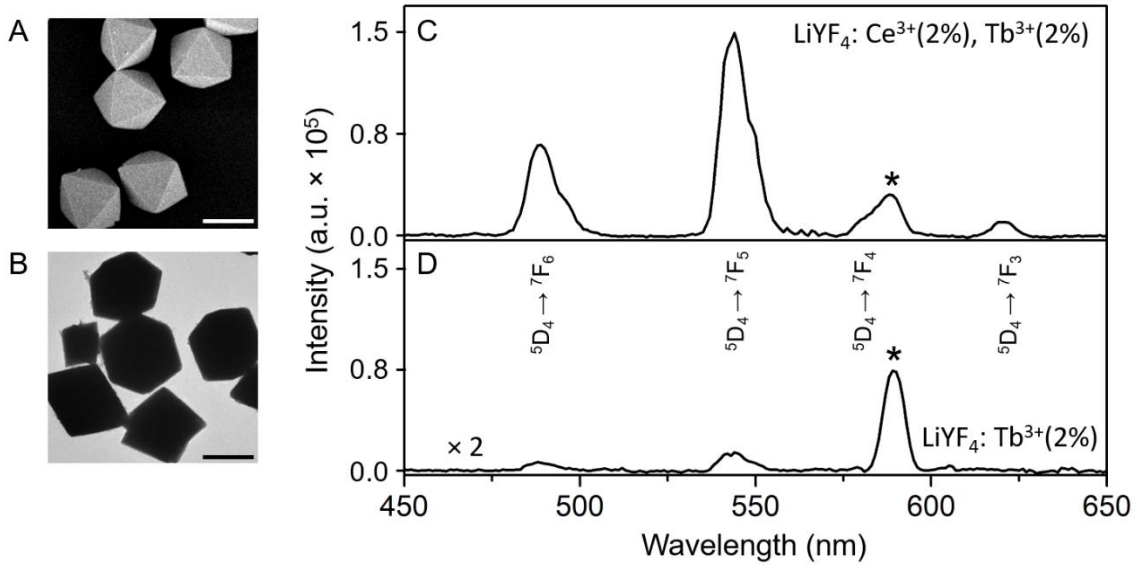

Figure 35. A/B) SEM and TEM micrographs of $LiYF_4$:Ce^{3+}(2%)/Tb^{3+}(2%) and $LiYF_4$:Tb^{3+}(2%) microparticles, respectively. Scale bar: 2 µm. C/D) Downshifting emission spectra of the Ce^{3+}/Tb^{3+} co-doped and Tb^{3+} doped $LiYF_4$ microparticles (concentration: 0.2 mg/mL in ethanol) under 295 nm UV excitation. Intensity of the Tb^{3+} emission presented in (D) was multiplied by two for better visualization of the emission bands. The second harmonic oscillation signal observed at 590 nm and attributed to the excitation source is denoted with (*).

4.2.2. Optical characterization of the upconverting Yb^{3+}/Er^{3+} and Yb^{3+}/Tm^{3+} co-doped M(RE)F_4 nano/microparticles

Spectra of the upconverted emission stemming from the Yb^{3+}/Er^{3+} co-doped $LiYF_4$ microparticles, Yb^{3+}/Tm^{3+} co-doped $LiYF_4$ microparticles, Er^{3+}-doped $LiYbF_4$ microparticles, Yb^{3+}/Er^{3+} co-doped β-$NaGdF_4$ and α-$NaYF_4$ nanoparticles are presented in **Figure 36-A** (*vide infra*). Energy level diagrams of the respective Yb^{3+}/Er^{3+} and Yb^{3+}/Tm^{3+} upconverting dopant systems are presented in **Figure 36-B**, and electronic transitions responsible for the observed emission bands are indicated.

Emission spectra of the Yb^{3+}/Er^{3+} co-doped M(RE)F_4 particles depict characteristic Er^{3+} emission bands – two green bands centered at 523 nm ($^2H_{11/2} \rightarrow {}^4I_{15/2}$) and 553 nm ($^4S_{3/2} \rightarrow {}^4I_{15/2}$), and a red band centered at 660 nm ($^4F_{9/2} \rightarrow {}^4I_{15/2}$) (**Figure 36-B-1**).[39] Traces of the blue emission centered at 410 nm ($^2H_{9/2} \rightarrow {}^4I_{15/2}$) were also detected.

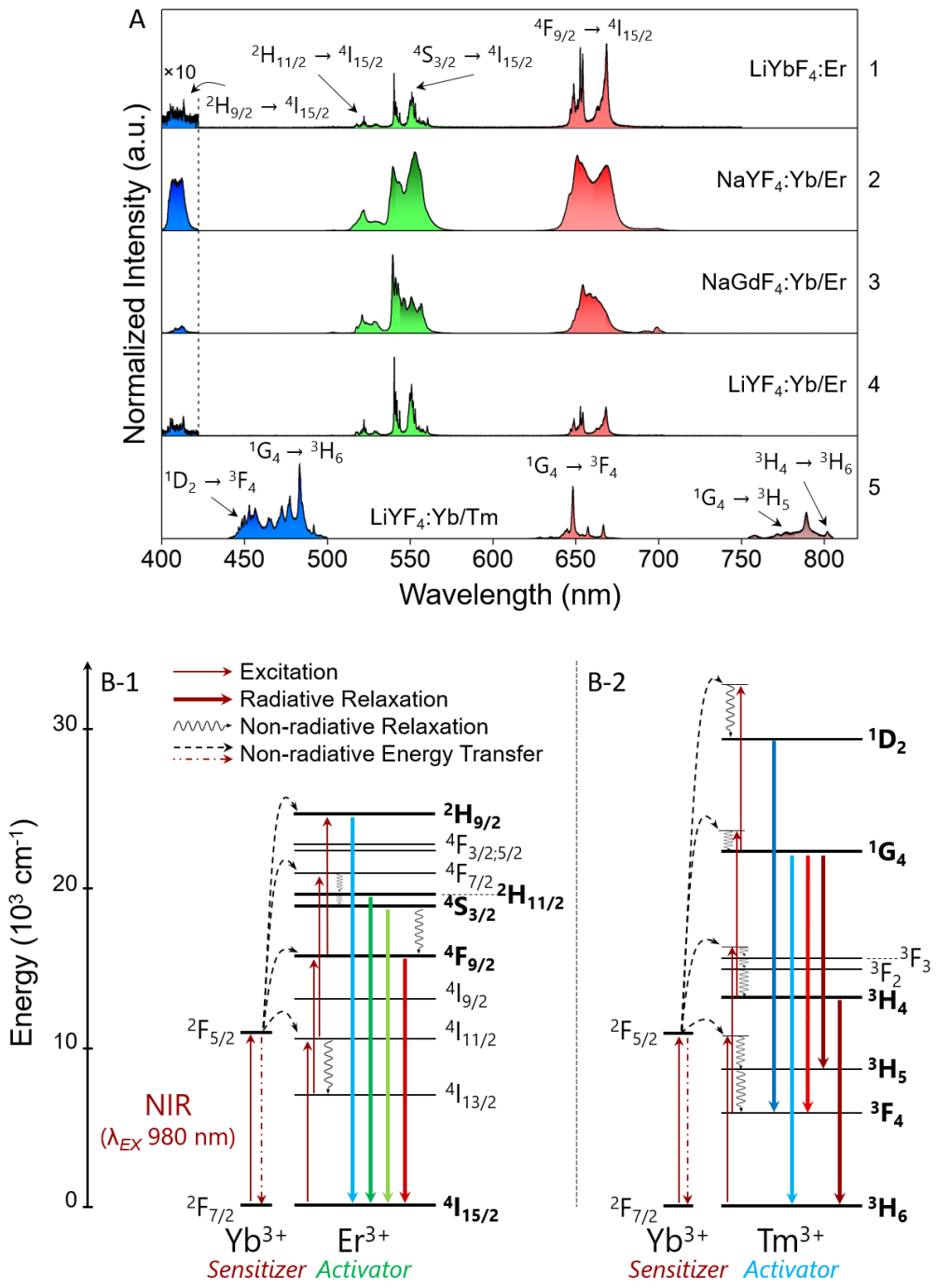

Figure 36. A) Normalized emission spectra of the Er^{3+}-doped $LiYbF_4$, Yb^{3+}/Er^{3+} co-doped α-$NaYF_4$, β-$NaGdF_4$, and $LiYF_4$, as well as Yb^{3+}/Tm^{3+} co-doped $LiYF_4$ under 980 nm NIR excitation. B) Energy level diagrams of the Yb^{3+}/Er^{3+} and Yb^{3+}/Tm^{3+} upconverting dopant systems depicting the electronic transitions that are responsible for the observed emission (relevant energy levels and their respective term symbols are in bold).

Similarly, the emission spectrum of the Yb^{3+}/Tm^{3+} co-doped $LiYF_4$ microparticles depicts characteristic Tm^{3+} emission bands – two blue bands centered at 455 ($^1D_2 \rightarrow {}^3F_4$) and 480 nm ($^1G_4 \rightarrow {}^3H_6$), a red band centered at 650 nm ($^1G_4 \rightarrow {}^3F_4$), and two bands in the NIR region centered at 790 nm ($^1G_4 \rightarrow {}^3H_5$) and 801 nm ($^3H_4 \rightarrow {}^3H_6$) (**Figure 36-B-2**).[22] It is noteworthy that the blue emission stemming from $LiYF_4:Yb^{3+}/Tm^{3+}$ is stronger than both the red and NIR emissions, as judged by the relative differences in integrated area of the respective bands. It is also evident from the five spectra presented in **Figure 36-A** that in comparison to α-$NaYF_4$, $Li(RE)F_4$ and β-$NaGdF_4$ hosts foster more resolved emission bands, irrespective of the dopant system. This is a consequence of the higher degree of crystal-field splitting of the $4f^n$ configurations in Er^{3+} and Tm^{3+} by the lower-symmetry crystalline environment provided by the tetragonal phase $Li(RE)F_4$ and β-$NaGdF_4$, as previously discussed in **Section 1.1.3** of the introduction.[22]

Additional insight can be gained into the optical behavior of the four different $M(RE)F_4$ host materials by comparing the relative intensities of the green and red emission bands stemming from the respective Yb^{3+}/Er^{3+} co-doped systems. From this comparison one can infer which levels – the higher emitting ones responsible for the green emissions ($^2H_{11/2} \rightarrow {}^4I_{15/2}$, $^4S_{3/2} \rightarrow {}^4I_{15/2}$) or the lower energy level feeding the red emission ($^4F_{9/2} \rightarrow {}^4I_{15/2}$) – are more likely to be populated in each system under the same experimental conditions. The green-to-red intensity ratios have been determined to be 0.4, 0.8, 1.1, and 1.6 for $LiYbF_4$, $NaYF_4$, $NaGdF_4$, and $LiYF_4$, respectively. Narrowing the focus on the lithium-based materials, it is interesting to note that $LiYF_4$ fosters stronger green emission, while $LiYbF_4$ favors the red upconversion emission. This behavior is in accordance with previously reported observations that increasing the sensitizer (Yb^{3+}) concentration in the Yb^{3+}/Er^{3+} co-doped $Li(RE)F_4$ and $Na(RE)F_4$ systems yields stronger red emission.[122,123] Specifically, increasing the relative concentration of Yb^{3+} in the host lattice decreases the interatomic distance between the Yb^{3+} and Er^{3+} dopants and facilitates cross-relaxation energy transfers from Er^{3+} to Yb^{3+}.[123] Ultimately, this decreases the population of the Er^{3+} excited states responsible for yielding the green ($^2H_{11/2}$ and $^4S_{3/2}$) and blue ($^2H_{9/2}$) emissions, thus increasing the relative intensity of the red emission, *i.e.*, $^4F_{9/2} \rightarrow {}^4I_{15/2}$ transition.[123] Overall, these results may be of interest in fields where colour tuning is an important requisite, *i.e.* for potential display or lighting applications.

4.3. Results and discussion (Part 2)

4.3.1. Hyperspectral imaging of the Yb^{3+}/Er^{3+} and Yb^{3+}/Tm^{3+} co-doped $LiYF_4$ microparticles

As previously shown in **Figure 36-A-4/5**, Yb^{3+}/Er^{3+} and Yb^{3+}/Tm^{3+} co-doped $LiYF_4$ microparticles synthesized *via* method №1 exhibited characteristic upconverted emission upon 980 nm excitation. Further investigation of their optical properties by means of single-particle hyperspectral imaging revealed spatial variability in upconverted emission between individual particles. More specifically, probing single particles by scanning of the excitation beam over a region of interest containing several $LiYF_4$ microparticles yielded a spectral map, which displays the spatial distribution of the blue Tm^{3+} (440–500 nm) and green Er^{3+} (510–570 nm) upconverted emissions (**Figure 37-A/B-1**).

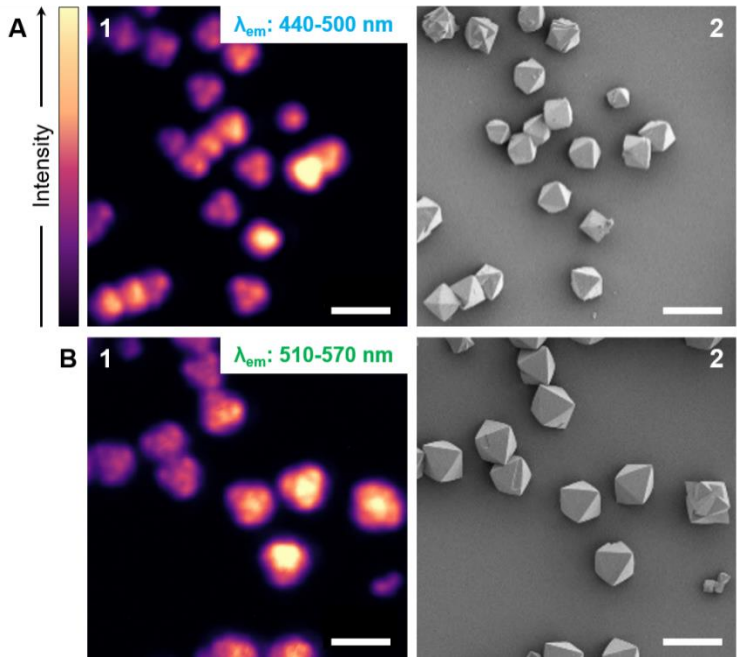

Figure 37. Single-particle hyperspectral imaging study on (A) Yb^{3+}/Er^{3+} and (B) Yb^{3+}/Tm^{3+} co-doped $LiYF_4$ microparticles. 1) False-colour hyperspectral images of the characteristic blue Tm^{3+} (440–500 nm) and green Er^{3+} (510–570 nm) emissions. 2) SEM micrographs of the respective microparticles. Scale bars: 5 μm.

In combination with SEM imaging of the same region of interest, this allowed for illustration of interparticle differences in intensity of the dominant emission bands for both upconverting systems (**Figure 37-A/B-2**).[XXI]

A closer examination of the hyperspectral image cubes and the respective SEM micrographs of both upconverting systems revealed a close link between the observed spatial distribution of the upconverted emission and spatial particle orientation, *i.e.*, the emission direction being probed.

This link became especially evident when comparing two groups of the Yb^{3+}/Tm^{3+} co-doped $LiYF_4$ microparticles: microparticles numbered 1–4 and 5–8 in **Figure 38-A-1/2/3** (*vide infra*). From the top-view hyperspectral images and the SEM micrograph A1–3 in **Figure 38** it is apparent that particles №5–8 are lying flat on one of their triangular facets, whereas particles №1–4 are not.

From here on, the former particle orientation will be referred to as neutral and the latter as non-neutral.[XXII] As illustrated in **Figure 39** (*vide infra*), the principal axis (axis with the highest rotational symmetry; also the crystallographic *c*-axis; also the optic axis; *vide infra* **Section 4.3.2**) of a $LiYF_4$ microparticle makes a *ca*. 33° angle (β) with the substrate when it is oriented neutrally.[XXIII] Consequently, during the hyperspectral imaging study, the emission of such particles was probed at a *ca*. 56° angle (θ) relative to the principal axis.

In the two extremes of the non-neutral particle orientation, the principal axis of the microparticle is either parallel (β = 0°) or perpendicular (β = 90°) to the substrate. Any other non-neutral orientation would result in an angle β that is between 0 and 33° or between 33 and 90°. Consequently, during the hyperspectral imaging study, the emission of such particles was probed at an angle θ that was anywhere between 0 and 90°, with the exception of 56°.

XXI The hyperspectral and SEM imaging of the same region of interest were performed separately, *i.e.*, after obtaining the hyperspectral image, the same region of interest was found and imaged *via* SEM.

XXII A neutral spatial orientation implies that the particle is oriented such that it has the lowest potential energy in physical space. This particle orientation is more common. Conversely, a particle that is oriented non-neutrally will have a higher potential energy in physical space. A non-neutral orientation can thus be achieved only when the respective particle is propped-up by another one.

XXIII It should be noted that the angle between the principal axis of a particle defined by a square-based bipyramidal morphology and the substrate is inversely proportional to the particle's AR. The angle of *ca*. 33° was calculated for a microparticle with an AR of 1.1.

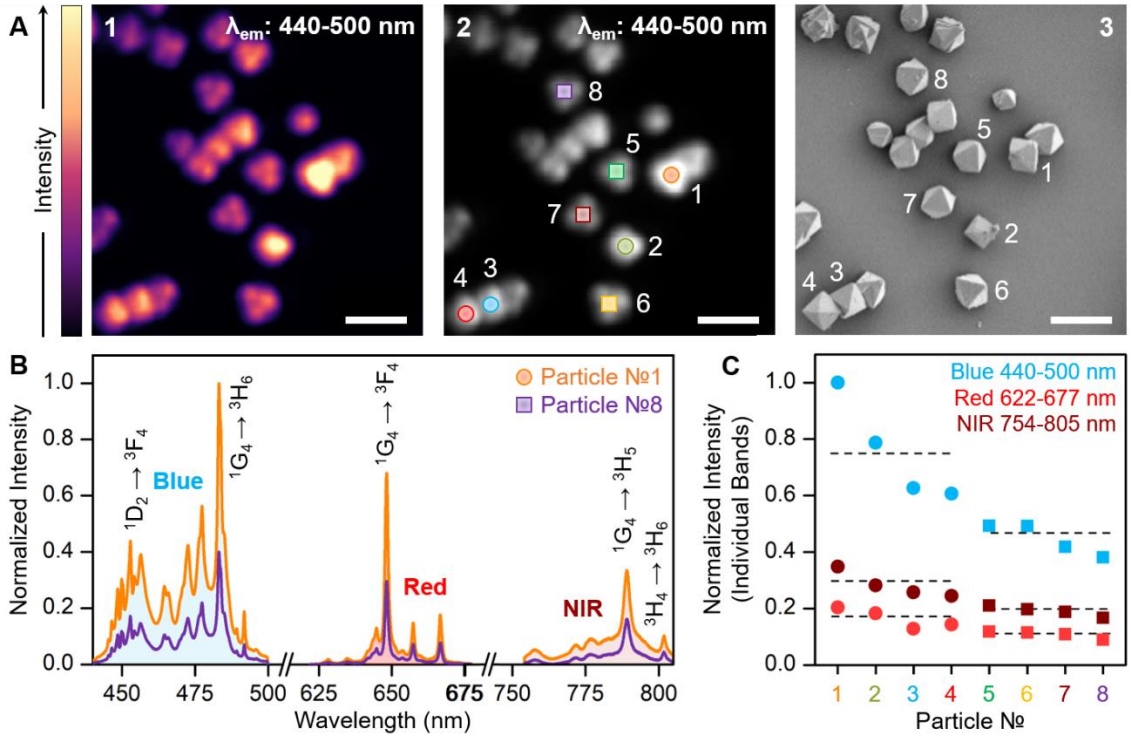

Figure 38. A1,2) False-colour and greyscale hyperspectral images of the blue (440–500 nm) emission stemming from Yb^{3+}/Tm^{3+} co-doped $LiYF_4$ microparticles. A3) SEM micrograph displaying the morphology and spatial orientation of the respective microparticles. Scale bars: 5 µm. B) Normalized spectra of the upconverted emission stemming from the strongest and weakest emitting microparticles №1 and 8, respectively. C) Plot of the integrated intensities of the blue (440–500 nm), red (622–677 nm), and NIR (754–805 nm) emission bands (normalized to the highest-intensity emission band) stemming from particles №1–8, plotted in the order of decreasing intensity. Particles are grouped by their spatial orientation – non-neutral (1–4) and neutral (5–8). Average emission intensities (a.u.) for the two particle groups are indicated as dashed lines.

It is evident from the false-colour and greyscale hyperspectral images A1 and A2 in **Figure 38** that the non-neutrally oriented $LiYF_4$:Yb^{3+}/Tm^{3+} microparticles №1–4 exhibit stronger blue emission (440–500 nm) as compared to the neutrally oriented microparticles №5–8 (hyperspectral images depicting the spatial distribution of the red (622–677 nm) and NIR (754–805 nm) emission bands revealed the same trend).

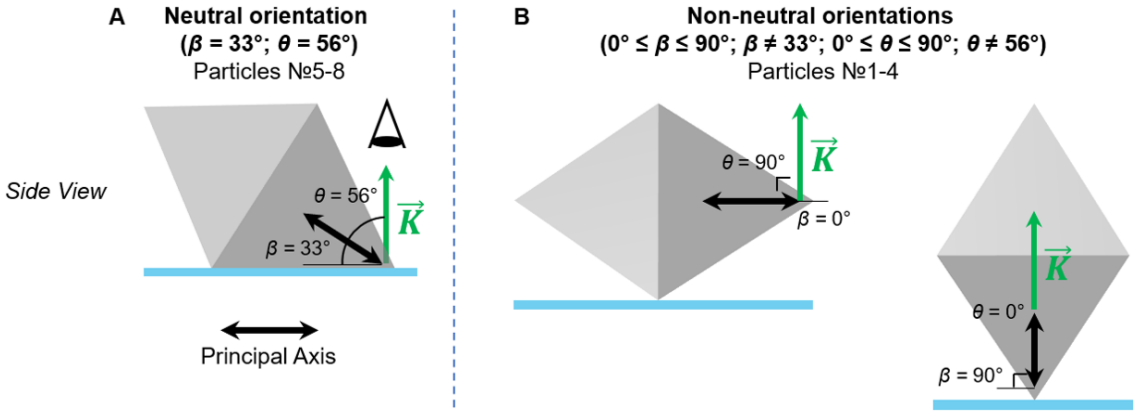

Figure 39. Side-view illustration of A) the neutral $LiYF_4$ microparticle orientation and B) the two extreme non-neutral microparticle orientations. Any other orientation in which $0° < \beta < 33°$ or $33° < \beta < 90°$ would fall in the non-neutral particle orientation category. β defines the angle between the principle axis (*i.e.*, crystallographic *c*-axis/optic axis) of a square-based bipyramidal $LiYF_4$ microparticle and the substrate. θ defines the angle between the emission vector $\vec{K}$ and the principle axis.

For comparison, **Figure 38-B** depicts the normalized spectra of the upconverted emission stemming from the strongest and weakest emitting particles №1 and 8, respectively.[XXIV]

The observed difference in spatial emission intensity distribution between the neutrally and non-neutrally oriented microparticles was confirmed by carrying out a more comprehensive spectral analysis. More specifically, the emission spectra of every particle was normalized relative to the maximum intensity signal of the brightest particle (№1); then, the blue (440–500 nm), red (622–677), and NIR (754–805 nm) emission bands were individually integrated and the resulting normalized band intensities were subsequently plotted for each particle (**Figure 38-C**).

These results reveal that when the upconverted emission is probed perpendicularly to the substrate, the average blue (0.75 a.u. ± 21%), red (0.16 a.u. ± 19%), and NIR (0.28 a.u. ± 14%) emissions stemming from the non-neutrally oriented particles №1-4 ($0° \leq \theta \leq 90°$; $\theta \neq 56°$) are stronger than the average blue (0.45 a.u. ± 11%), red

[XXIV] Every pixel of the hyperspectral image carries spectral information over a specified wavelength range. All of the emission spectra (and spectra-related data) presented herein were constructed by averaging the spectra extracted from many pixels inside a circular area that falls within the contours of the imaged microparticles (area of *ca.* 2 and 3 μm^2 for Yb^{3+}/Tm^{3+} and Yb^{3+}/Er^{3+} co-doped $LiYF_4$ microparticles, respectively).

(0.11 a.u. ± 9%), and NIR (0.19 a.u. ± 11%) emissions stemming from the neutrally oriented particles №5–8 (θ = 56°). This suggests that the emission generated by a $LiYF_4:Yb^{3+}/Tm^{3+}$ microparticle is not isotropic in the spectral range analyzed herein and that the individual emission bands do not exhibit the same degree of direction-dependence (it appears that the intensity of the blue emission exhibits greater dependence on emission direction as compared to the red and NIR emissions). Hence, it is postulated that the observed interparticle variation in spatial emission intensity distribution is a product of the intrinsic intraparticle direction-dependent emission (*vide infra* **Section 4.3.2**).

It should be noted that the origin of the higher relative standard deviation associated with the average direction-dependent emission band intensities of the non-neutrally oriented particles №1–4 is likely related with the fact that the angle β between their principal axis and the substrate, and consequently the angle θ at which the emission was probed relative to their principle axis, are subject to a greater degree of variation as compared to the angles characterizing the spatial orientation and emission direction of the neutrally oriented particles №5–8, which were exclusively 33° (β) and 56° (θ), respectively.

To corroborate the dependence of the emission intensity on the emission direction relative to the principal axis of a tetragonal-phase $LiYF_4:RE^{3+}$ microparticle, $LiYF_4:Yb^{3+}/Er^{3+}$ co-doped microparticles were also subjected to the hyperspectral imaging analysis (*vide infra* **Figure 40**).

From the false-colour and greyscale hyperspectral images A1 and A2 in **Figure 40** it is evident that the intensity of the green emission (510–570 nm) generated by Yb^{3+}/Er^{3+} co-doped $LiYF_4$ microparticles also varies particle-to-particle (the hyperspectral image depicting the spatial distribution of the red (627–682 nm) emission band revealed the same trend). However, the corresponding SEM micrograph A3 reveals that every particle is oriented neutrally. This observation is unexpected in the context of the previously established relationship between spatial emission intensity distribution and particle orientation, but may be explained on the basis of particle size-related effects on emission intensity. More specifically, it is well established that in comparison to larger particles, emission stemming from smaller particles is weaker because the relative increase in the surface-to-volume ratio fosters more surface-induced emission quenching.[49,50]

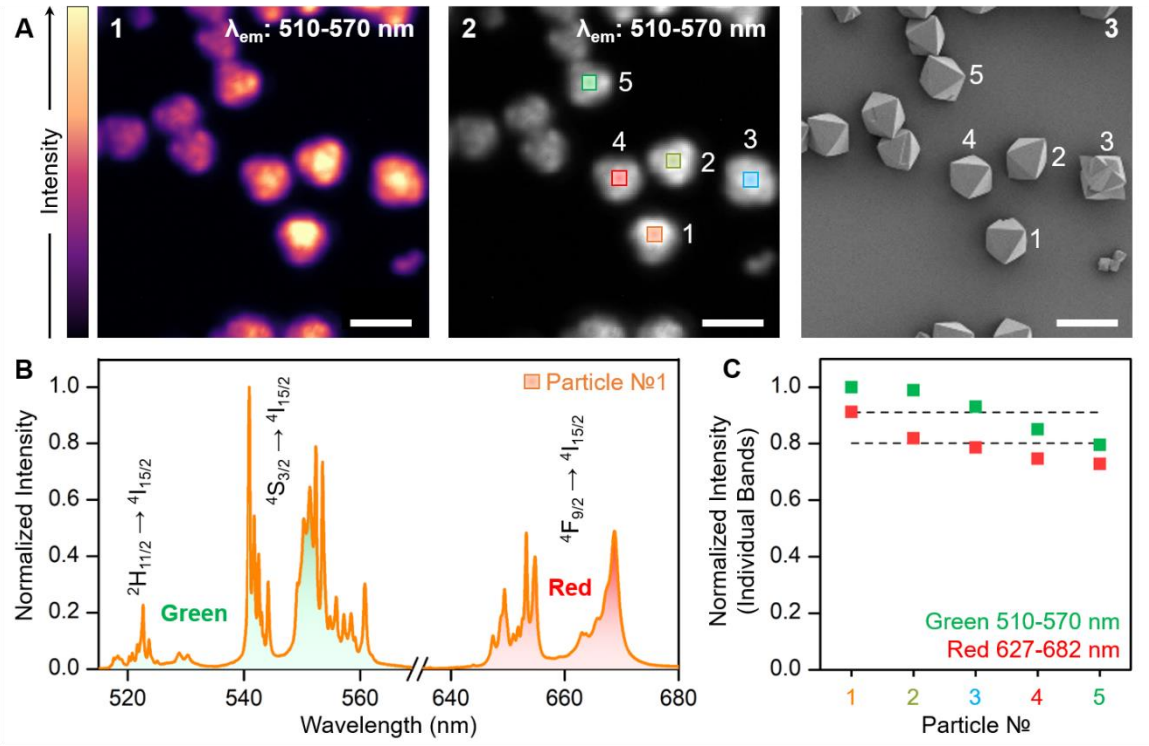

Figure 40. A1,2) False-colour and greyscale hyperspectral images of the green (510–570 nm) emission stemming from Yb^{3+}/Er^{3+} co-doped $LiYF_4$ microparticles. A3) SEM micrograph displaying the morphology and spatial orientation of the respective microparticles. Scale bars: 5 µm. B) Normalized spectrum of the upconverted emission stemming from the strongest emitting microparticle №1. C) Plot of the integrated intensities of the green (510–570 nm) and red (627–682 nm) emission bands (normalized to the highest-intensity emission band) stemming from particles №1–5, plotted in the order of decreasing intensity. All particles are oriented neutrally. Average emission intensities (a.u.) are indicated as dashed lines.

Indeed, for the exception of one particle (leftmost) in **Figure 40-A-1/2/3**, $LiYF_4$:Yb^{3+}/Er^{3+} microparticles exhibiting weaker green emission intensity than particles №1-5 are *ca*. 6% smaller (compared by equatorial edge length). It is thus conceivable that a 6% difference in particle size is responsible for the observed difference in emission intensity. However, taking into account that this particle size difference is not very significant and that one of the probed microparticles doesn't fit the provided explanation, it is possible that the observed difference in emission intensity between neutrally oriented microparticles is caused by (an)other, unaccounted-for variable(s). Nevertheless, to avoid possible particle size-related effects on emission intensity, comparative analysis of the interparticle emission intensity was conducted on particles №1–5.

The average interparticle intensities of the green (510–570 nm) and red (627–682 nm) emission bands were determined to be 0.91 a.u. ± 9% and 0.80 a.u. ± 8%, respectively. Because all probed particles were neutrally oriented, the relative standard deviation range (8–9%) associated with their average interparticle emission band intensities is comparable to the respective relative standard deviation range (9–11%) associated with the average emission intensities of the neutrally oriented $LiYF_4:Yb^{3+}/Tm^{3+}$ microparticles. Ultimately, these results provide further support for the observed relationship between upconverted emission intensity and emission direction relative to the principal axis of a single tetragonal-phase $LiYF_4$ microparticle.

Previously published works have provided the following tentative explanations for the observed intraparticle[XXV] emission intensity variation: inhomogeneous RE^{3+} dopant distribution, a difference in the crystal-field strength experienced by dopant ions occupying crystallographic sites that are located in the interior of the $LiYF_4$ particle *vs*. its apex or face, as well as uneven surface-ligand coverage.[76,124] The purpose of the next section of the discussion is not to disprove these plausible reasons. Rather, the aim is to provide a plausible explanation for the observed optical phenomenon by taking into consideration the fact that $LiYF_4$ is a uniaxial crystalline material, and that the consequent non-centrosymmetric crystalline environment around the RE^{3+} dopants fosters direction-dependent polarized emission.

4.3.2. Probing polarized emission from $LiYF_4:RE^{3+}$

Tetragonal-phase $LiYF_4$ is uniaxially anisotropic, and thus exhibits polarized emission when doped with luminescent RE^{3+}.[82] The emission probability in a particular direction is in part determined by the degree to which the respective electronic transition satisfies the polarization-dependent selection rules (*vide supra* **Table 1**). More specifically, the probability of emission, *i.e.*, emission intensity, with a particular polarization state, changes

[xxv] In order to prevent any confusion regarding the use of "intra-" *vs.* "interparticle" terminology, it is important to reiterate that it is herein postulated that the *inter*particle variation in spatial emission distribution revealed by the hyperspectral imaging studies is a product of the intrinsic *intra*particle variation in emission intensity, *i.e.*, direction-dependent emission.

as a function of emission direction relative to the optic axis, because the orientation of any constant emission polarization (electric/magnetic field vectors) relative to the optic axis also changes as a function of emission direction relative to the optic axis.[58,60,69,125] Furthermore, the relative intensity of specific emission bands may also change as a function of emission direction relative to the optic axis, because probabilities of the respective electronic transitions may be governed by different selection rules with respect to polarization, *i.e.*, emission of a photon with a particular polarization state relative to the optic axis may be allowed for one electronic transition, but not for another.[59]

Thus, in theory, the observation revealed by hyperspectral imaging that the intensities of the blue, red, and NIR emission bands stemming from a single $LiYF_4:Yb^{3+}/Tm^{3+}$ microparticle are unequally direction-specific could be associated with that the probabilities of the respective electronic transitions exhibit different degrees of dependence on the orientation of the emission polarization, and hence emission direction, relative to the optic axis.[59] To provide experimental evidence in support of this plausible explanation, it was necessary to verify that *i*) emission stemming from $LiYF_4:RE^{3+}$ microparticles was polarized in at least one direction, and if it was, that *ii*) the degree of its polarization changed as a function of the emission direction relative to the optic axis, and lastly, that *iii*) the change in the degree of polarization was accompanied by a respective change in emission intensity as a function of emission direction relative to the optic axis.

Knowing the exact orientation of the optic axis in the microparticle that is being probed for polarized emission would be key for a properly conducted single-particle polarized emission investigation. By definition, a unit cell of a tetragonal crystal system is defined by the lattice parameters $a = b \neq c$ (α, β, $\gamma = 90°$), and the crystallographic *c*-axis is the optic axis.[82] Previously published crystallographic and morphologic analysis of square-based bipyramidal $Li(RE)F_4$ particles revealed that the particles are bound by {101} crystallographic planes, meaning that the crystallographic *c*-axis coincides with the morphologic principle axis, *i.e.*, axis of highest symmetry; axis along which the particles are elongated.[108] Thus, it follows that the morphologic principle axis in a tetragonal-phase $LiYF_4$ particle defined by a square-based bipyramidal morphology is the optic axis.

With this information at hand, $LiYF_4$ microparticles featuring various dopant systems were subjected to a polarized emission spectroscopy study. Specifically, single-particle

polarized emission spectroscopy was performed on dry $LiYF_4$ microparticles featuring the Yb^{3+}/Tm^{3+}, Yb^{3+}/Er^{3+}, and Nd^{3+} (5, 15, and 25%) dopant systems, as well as a $LiYF_4$:Yb^{3+}/Er^{3+} microparticle (from an aqueous dispersion) optically trapped in various spatial orientations.

4.3.2.1. *Single-particle polarized emission spectroscopy study of $LiYF_4$:RE^{3+} (Dry samples)*

In order to confirm that the $LiYF_4$ host matrix fosters polarized emission in at least one direction, irrespective of the RE^{3+} dopant system and/or doping concentration, single $LiYF_4$ microparticles featuring the upconverting (Yb^{3+}/Tm^{3+} and Yb^{3+}/Er^{3+}) and downshifting (Nd^{3+} – 5, 15, and 25%) dopant systems were subjected to a polarized emission spectroscopy study.

To probe for polarized emission, dilute dispersions of $LiYF_4$:RE^{3+} microparticles were drop-casted onto glass slides. Due to their square-based bipyramidal morphology and an AR of *ca*. 1.1–1.2, the microparticles oriented neutrally (*vide supra* **Section 4.3.1**), such that their optic axis made a *ca*. 33° angle (β) with the substrate.

Emission emerging in the direction *ca*. 56° (θ) relative to the optic axis of a stationary microparticle ($\vec{K} \parallel z$-axis) was probed for polarization by being passed through a linear polarizer positioned in various radial orientations before being detected (*vide infra* **Figure 41**). Please refer to **Section 4.1** for further experimental details.

For each dopant system, an emission spectrum was recorded for every 10° interval of the linear polarizer angle (ω) in the range of 0 to 360°, *i.e.*, the upconverted or downshifted emission stemming from a respective $LiYF_4$:RE^{3+} microparticle in the direction 56° (θ) relative to the optic axis was sliced into 36 equally distributed radial segments, each depicting a respective linear polarization state.

As an example, **Figure 42** (*vide infra*) depicts the polarized emission spectra obtained from a single $LiYF_4$:Yb^{3+}/Tm^{3+} microparticle for all 36 intervals of ω. Indeed, it is evident that the intensity of individual emission bands and their relative intensity to each other changes cyclically as a function of ω with a period of 180°.

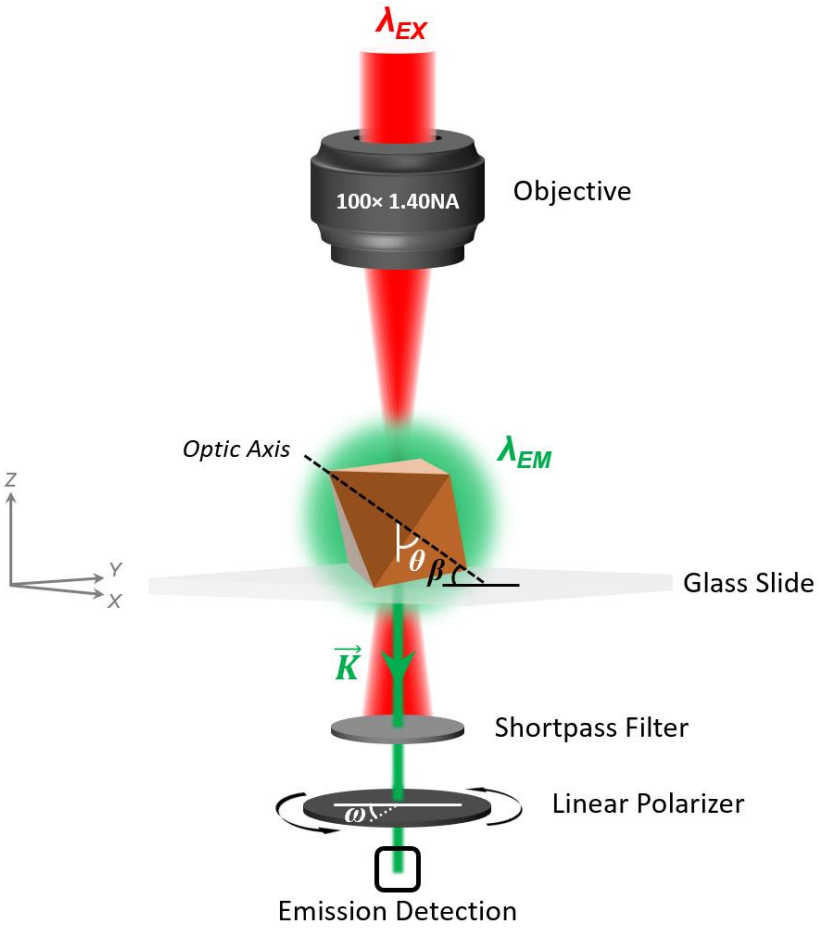

Figure 41. Single-particle polarized emission spectroscopy setup. Dry $LiYF_4$:RE^{3+} microparticles were excited by 790 or 975 nm laser radiation (for the Nd^{3+}- and Yb^{3+}-containing dopant systems, respectively) and their polarized emission ($\vec{K}$) was probed ‖ to *z*-axis (θ = 56°). Probed particles were oriented neutrally (β = 33°). Polarized emission spectra were recorded at 10° intervals of ω from 0 to 360°.

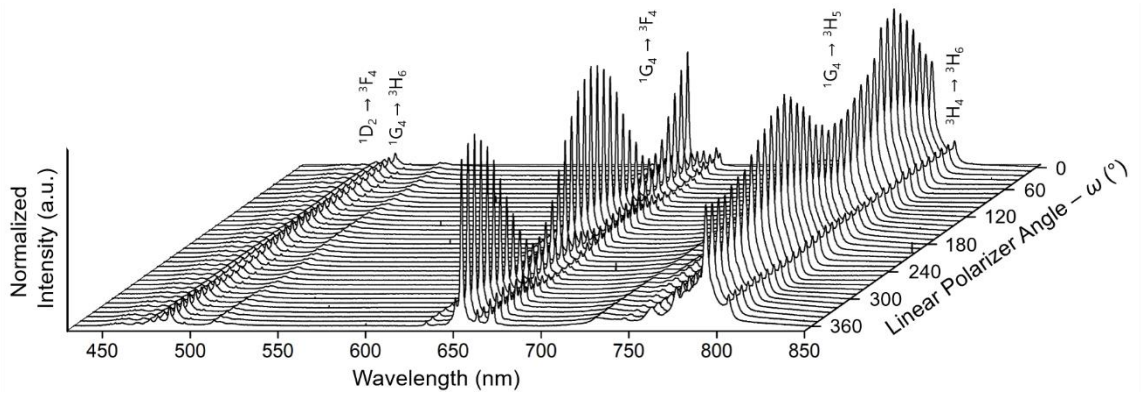

Figure 42. Polarized emission spectra recorded for every 10° interval of the linear polarizer angle (ω) in the range of 0 to 360°. Emission was generated by a single, neutrally oriented (β = 33°) $LiYF_4$:Yb^{3+}(25%)/Tm^{3+}(0.5%) microparticle and was probed ‖ to *z*-axis (θ = 56°).

Thus, it may be unequivocally stated that emission generated by a $LiYF_4:Yb^{3+}/Tm^{3+}$ microparticle is polarized when emitted along $\vec{K}$ such that $\theta = 56°$. The same observation was made for all other $LiYF_4:RE^{3+}$ systems subjected to the single-particle polarized emission investigation in the dry state. As proof, **Figure 43** depicts the average polarized emission spectra (obtained from three particles) for the Yb^{3+}/Tm^{3+}, Yb^{3+}/Er^{3+}, and Nd^{3+}(25%) dopant systems at orthogonal angles of ω for which the maximum difference in spectral shape was observed.

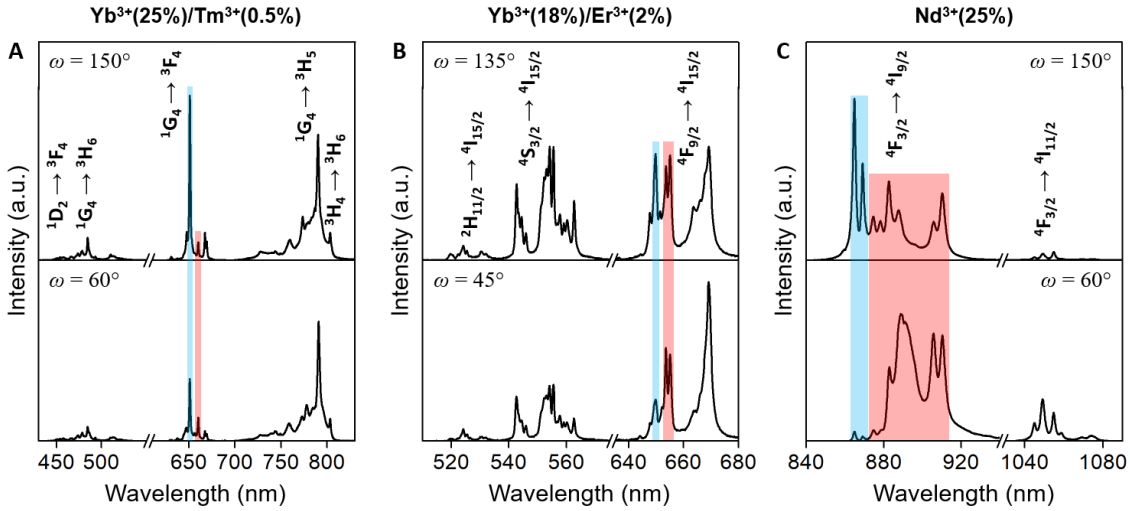

Figure 43. Emission spectra recorded at orthogonal orientations (ω) of the linear polarizer for neutrally oriented ($\beta = 33°$, $\theta = 56°$) $LiYF_4$ microparticles featuring the A) Yb^{3+}(25%)/Tm^{3+}(0.5%), B) Yb^{3+}(20%)/Er^{3+}(2%), and C) Nd^{3+}(25%) dopant systems. Highlighted bands were used for constructing the respective polar plots.

The degree of emission polarization for each dopant system can be better visualized with the use of a polar plot. A polar plot is typically constructed by plotting the intensity ratio between two particular emission bands in a manifold as a function of the linear polarizer angle (ω; *vide infra* **Figure 44**). In this work, well-resolved manifolds in the $^1G_4 \rightarrow {}^3F_4$ band of Yb^{3+}/Tm^{3+} (650–653 nm and 659–661nm), the $^4F_{9/2} \rightarrow {}^4I_{15/2}$ band of Yb^{3+}/Er^{3+} (648–651 nm and 653–656 nm), and the $^4F_{3/2} \rightarrow {}^4I_{9/2}$ band of Nd^{3+} (860–870 nm and 870–910 nm) were used because they demonstrated relatively strong polarization-dependence as judged from the respective orthogonal polarized emission spectra presented in **Figure 43**.

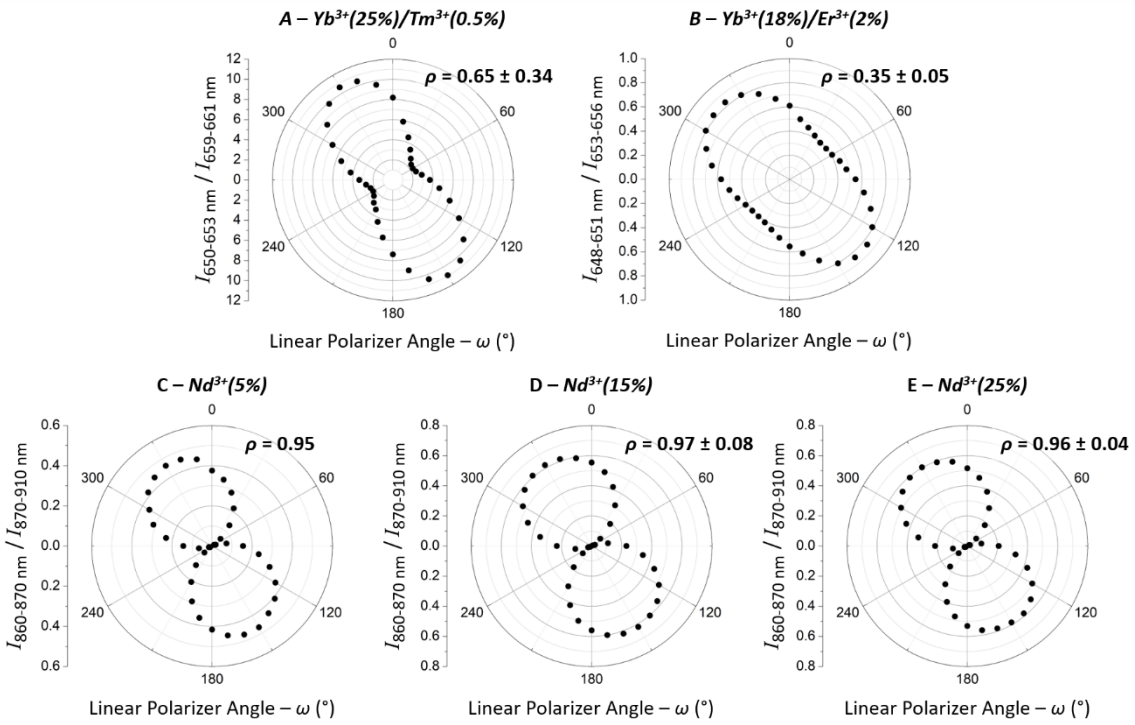

Figure 44. Polar plots depicting the intensity ratio between specific manifolds of the $^1G_4 \rightarrow {}^3F_4$ band of Yb^{3+}/Tm^{3+} (650–653 nm and 659–661nm), the $^4F_{9/2} \rightarrow {}^4I_{15/2}$ band of Yb^{3+}/Er^{3+} (648–651 nm and 653–656 nm), and the $^4F_{3/2} \rightarrow {}^4I_{9/2}$ band of Nd^{3+} (doping rate of 5, 15, 25%; 860–870 nm and 870–910 nm) as a function of the linear polarizer angle ω (°). Polarizability constant ρ indicates the degree of polarizability displayed by the emission bands that were used to construct the polar plot. All data, for the exception of that presented in C, is based on triplicate measurements.

The emission used to construct the experimental polar plots presented above was generated in one direction (θ = 56°) relative to the optic axis of the neutrally oriented microparticles of each respective dopant system. Thus, the origin of their shape difference must originate from the fact that the selection rules governing the respective 4f ↔ 4f electronic transitions in Tm^{3+}, Er^{3+}, and Nd^{3+} are dependent upon different photon polarization states.[59] More specifically, the shape of an experimental polar plot serves as an indication of the degree to which one emission band in a manifold is polarized relative to another, *i.e.*, how the polarization-dependence of one electronic transition compares to another. A circular plot indicates that both emission bands do not exhibit any preferential polarization in the emission direction being probed, whereas a plot with two pronounced lobes, *i.e.*, figure "8", indicates that one of the emission bands in a manifold is polarized to a much greater degree than the other. This comparative degree of polarization between two

emission bands can be quantitatively expressed as a polarizability constant ρ *via* **Equation 4**, which utilizes the maximum (I_{max}) and minimum (I_{min}) intensity band ratio values obtained from the polar plot.

Eq. 4
$$\rho = \frac{I\,max - I\,min}{I\,max + I\,min}$$

As indicated in **Figure 44**, the following values of ρ were obtained for the $LiYF_4:RE^{3+}$ systems subjected to single-particle polarized emission spectroscopy: 0.35 ± 0.05 for the Yb^{3+}/Er^{3+} system, 0.65 ± 0.34 for the Yb^{3+}/Tm^{3+} system, and an average value of *ca*. 0.96 for the three Nd^{3+} systems. Thus, it can be concluded that the selected emission bands in the Nd^{3+} system have the greatest difference in polarization, *i.e.*, the respective electronic transitions differ in their polarization-dependence the most, whereas the selected emission bands of the Yb^{3+}/Er^{3+} system exhibited the least difference in their polarization-dependence when probed in the same direction (θ = 56°) relative to the optic axis of the neutrally oriented microparticles.

Overall, these results confirm that emission stemming from the $LiYF_4$ host matrix is polarized in at least one direction (θ = 56°), irrespective of the dopant system and the dopant concentration.

4.3.2.2. *Single-particle polarized emission spectroscopy study of a $LiYF_4:Yb^{3+}/Er^{3+}$ microparticle inside an optical trap*

Having confirmed that emission stemming from neutrally oriented $LiYF_4:RE^{3+}$ microparticles is polarized when probed in the direction θ = 56° relative to the optic axis, optical trapping and consequent spatial orientation manipulation of a single $LiYF_4:Yb^{3+}/Er^{3+}$ microparticle was performed to probe for polarized emission propagating in other directions.

The main components of the experimental setup used for simultaneous optical trapping and luminescence detection of a single $LiYF_4:Yb^{3+}/Er^{3+}$ microparticle are depicted in **Figure 45** (*vide infra*). Please refer to **Section 4.1** for further experimental details.

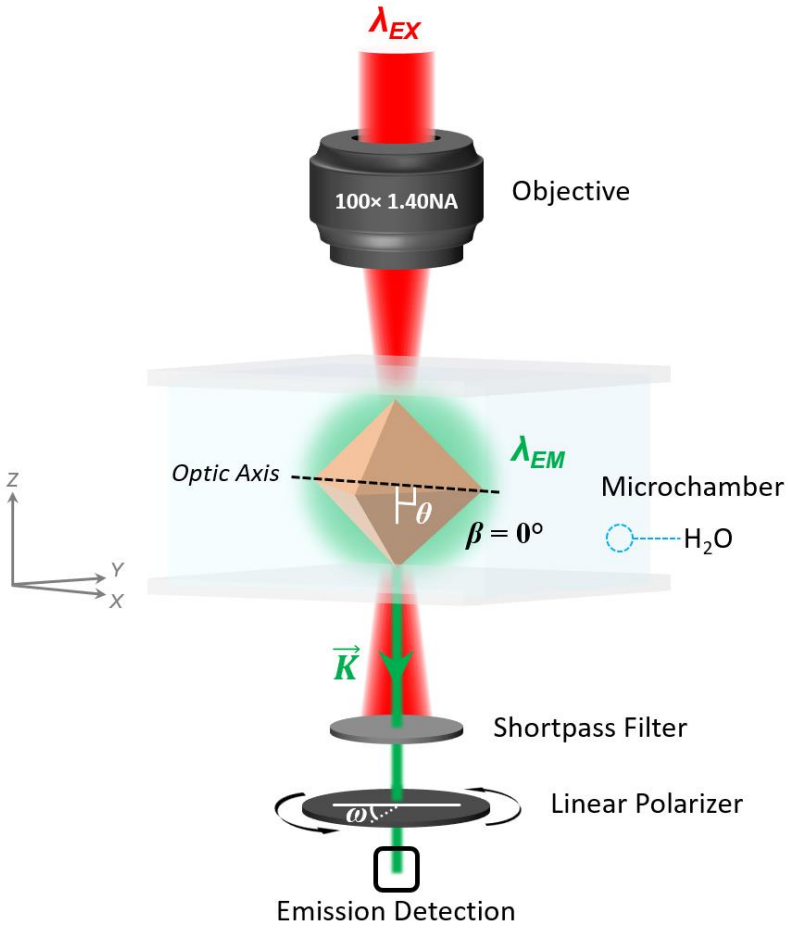

Figure 45. Single-particle polarized emission spectroscopy setup. A single $LiYF_4:Yb^{3+}/Er^{3+}$ microparticle out of a dilute aqueous microparticle dispersion was simultaneously optically trapped and excited by a highly focused 975 nm laser radiation. Particle orientation (neutral – β = 33° *vs.* non-neutral – β = 0°) inside the optical trap was controlled by adjusting the laser focus (only one of the non-neutral orientation is depicted in the scheme). Consequently, its polarized emission ($\vec{K}$) was probed ∥ to *z*-axis (neutral particle orientation – θ = 56° and β = 33°; non-neutral particle orientation – θ = 90° and β = 0°). Polarized emission spectra were recorded at 10° intervals of ω from 0 to 360°.

In brief, a single $LiYF_4:Yb^{3+}/Er^{3+}$ microparticle out of an aqueous microparticle dispersion was optically trapped and excited by highly focused, linearly polarized 975 nm laser radiation. Stability and spatial orientation of a particle inside the optical trap during polarized emission spectroscopy measurements was monitored in real time with a CMOS camera. Manipulating the laser focus within a particular range revealed that four stable particle orientations could be obtained. **Figure 46** (*vide infra*) depicts the schematic representations and top-view photographs of a microparticle in all four spatial orientations. Note that orientations №2 and 4 are likely equivalent.

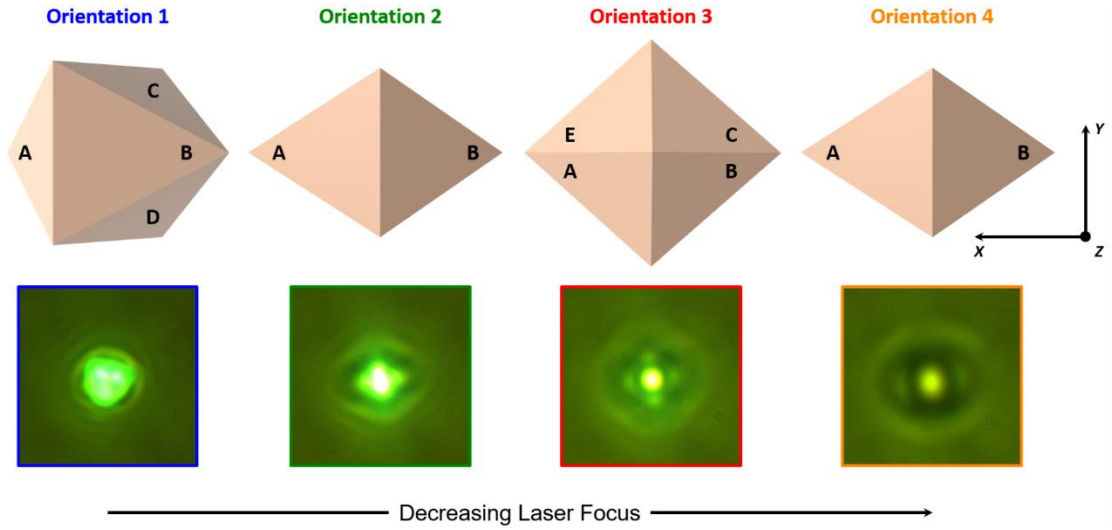

Figure 46. Schematic representations and top-view photographs of a $LiYF_4:Yb^{3+}/Er^{3+}$ microparticle optically trapped and excited in four spatial orientations by 975 nm laser radiation. Different spatial orientations could be achieved by manipulating the laser focus. Orientations 2 and 4 are likely equivalent.

From **Figure 46**, it is evident that in all four orientations, the optic axis *AB*/*EC* of the particle is (almost) parallel with the *x*-axis. Thus, the particle is neutrally oriented relative to the *xy* plane when in orientation №1 and non-neutrally oriented when in orientations №2–4. More specifically, because the emission was probed from underneath the microparticle along the *z*-axis, the direction of the probed emission relative to its optic axis was again $\theta = 56°$ in orientation №1 and $\theta = 90°$ in orientations №2–4. Thus, optically trapping a $LiYF_4:Yb^{3+}/Er^{3+}$ microparticle yielded one new spatial orientation relative to the *xy* plane that could be used to probe the polarized emission stemming in the direction 90° relative to the particle's optic axis (orientations №2-4). This is very fortunate, since probing the polarized emission propagating in two different directions from the same microparticle under *identical experimental conditions* would provide insight into how the degree of polarization changes as a function of emission direction relative to its optic axis. Indeed, precisely for this reason, single-particle polarized emission spectroscopy measurements inside an optical trap were limited only to the $LiYF_4:Yb^{3+}/Er^{3+}$ microparticles (4.4 ± 0.4 μm by 4.0 ± 0.2 μm). More specifically, when optically trapped, the smaller $LiYF_4:Yb^{3+}/Tm^{3+}$ (3.8 ± 0.4 μm by 3.3 ± 0.2 μm) and $LiYF_4:Nd^{3+}$ (doping rate of 2.5–25%; average dimensions of 2.4 ± 0.3 μm by 2.0 ± 0.3 μm) microparticles always oriented such that their

optic axis was perpendicular to the direction of laser propagation (OA $\perp \vec{K}$; *vide infra*). Thus, probing their polarized emission only in the direction 90° relative to the microparticle optic axis would not provide any insight into how the polarizability changes as a function of emission direction.

As for the single-particle polarized emission spectroscopy study performed on dry $LiYF_4:Yb^{3+}/Er^{3+}$ particles, the intensity ratios between the same two well-resolved Stark bands were used to construct the polar plots for each respective $LiYF_4:Yb^{3+}/Er^{3+}$ microparticle orientation inside the optical trap (**Figure 47**).

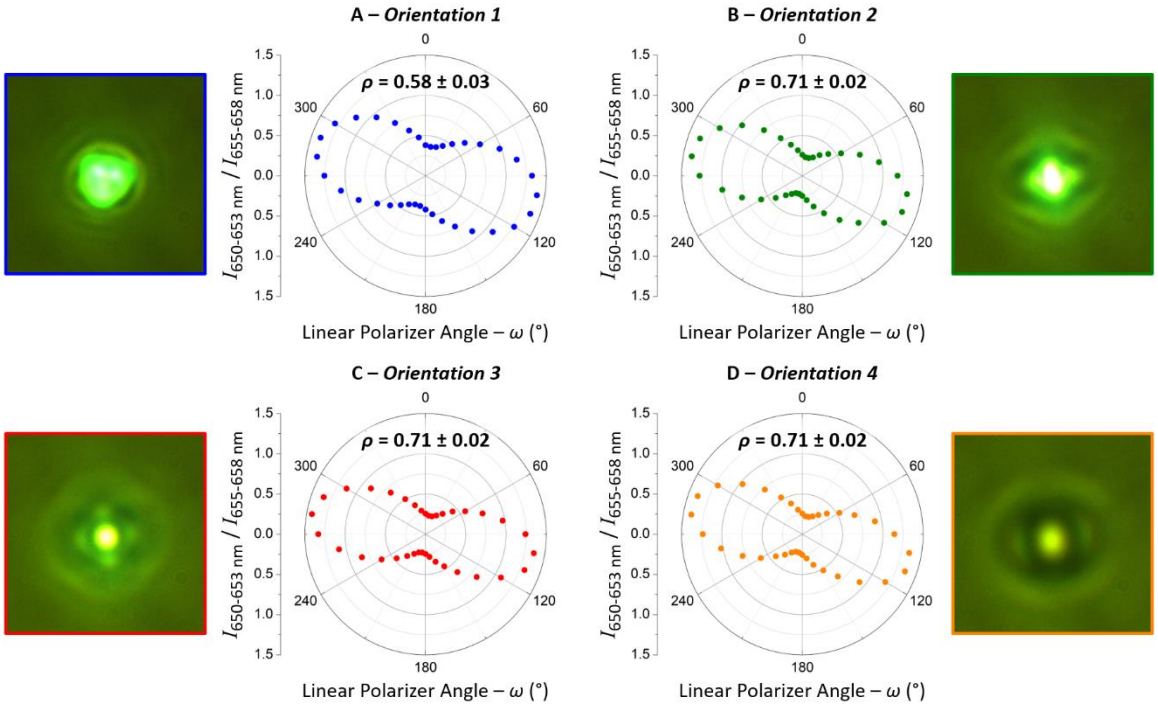

Figure 47. A-D) Polar plots for every respective $LiYF_4:Yb^{3+}/Er^{3+}$ microparticle orientation inside an optical trap. Polar plots depict the intensity ratio between specific Stark bands of the $^4F_{9/2} \rightarrow {}^4I_{15/2}$ transition (650–653 nm and 655–658 nm) as a function of the linear polarizer angle ω (°). All data is based on triplicate measurements.

As expected, because the emission stemming from microparticles in orientations №2–4 was probed at the same angle relative to their optic axis ($\theta = 90°$), the respective polar plots have identical shapes and a common polarizability constant ($\rho = 0.71 \pm 0.02$). Conversely, because the emission stemming from the microparticle in orientation №1 was probed at a different angle relative to its optic axis ($\theta = 56°$; different in comparison to the

microparticles in orientations №2–4), the respective polar plot has a unique shape and polarizability constant (ρ = 0.58 ± 0.03).[XXVI]

These results provide unequivocal evidence that the degree of emission polarization (ρ) does indeed change as a function of emission direction relative to the optic axis (θ). However, this does not necessarily mean that the overall intensity of the emission bands, *i.e.*, average band intensity for all values of ω, used to construct the respective polar plots also changes as a function of emission direction.

To determine whether or not the observed change in the degree of polarization between the two probed bands coincides with the change in their overall emission intensity as a function of emission direction relative to the optic axis, the polarized emission spectra obtained for all values of ω were averaged and analysed for all four particle orientations (three particles were probed for every orientation; **Figure 48**).

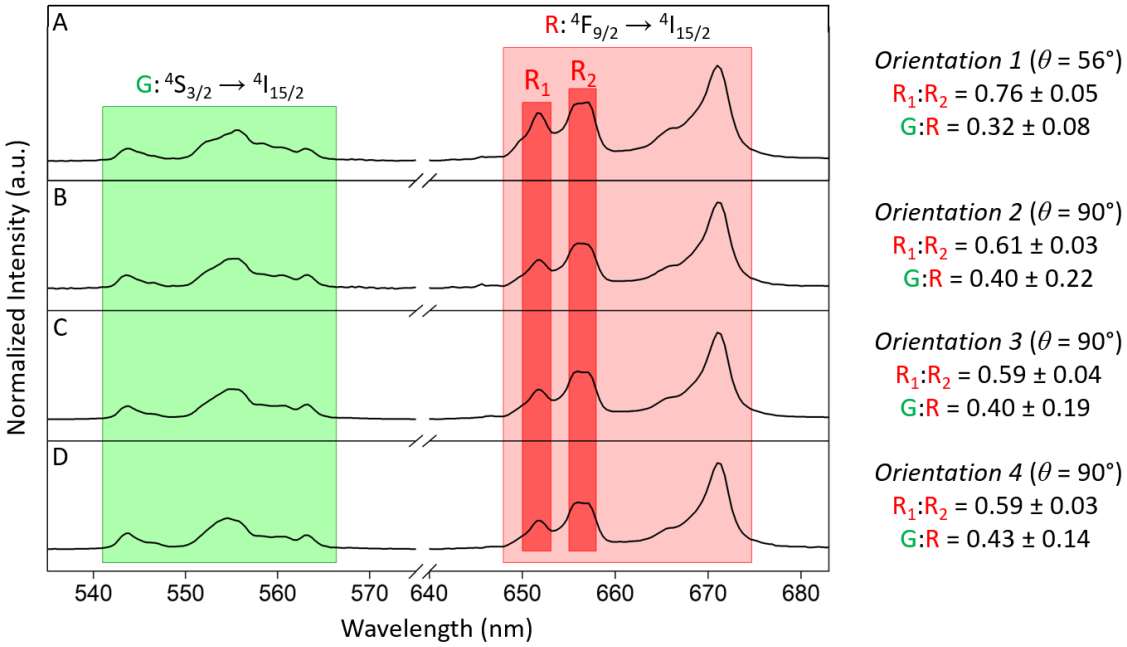

Figure 48. Average polarized emission spectra (obtained by averaging the spectra corresponding to all linear polarizer angles ω) for each of the four spatial $LiYF_4:Yb^{3+}/Er^{3+}$ microparticle orientations inside an optical trap. All data is based on triplicate measurements.

[XXVI] It should be noted that the difference in ρ between the two polar plots depicting the polarized emission distribution stemming from a neutrally oriented (θ = 56°) $LiYF_4:Yb^{3+}/Er^{3+}$ microparticle inside an optical trap (ρ = 0.58 ± 0.03) *vs.* a neutrally oriented $LiYF_4:Yb^{3+}/Er^{3+}$ microparticle in a dry sample (ρ = 0.35 ± 0.05) is a consequence of the different experimental conditions, *e.g.*, milieu and laser power density.[52]

Indeed, it is evident from **Figure 48** that the intensity ratio between the two bands (R_1: 650–653 nm; R_2: 655–658 nm) used to construct the polar plots (in **Figure 47**) changes as a function of emission direction: R_1:R_2 = 0.76 ± 0.05 for orientation 1 (θ = 56°), R_1:R_2 = 0.61 ± 0.03 for orientation 2 (θ = 90°), R_1:R_2 = 0.59 ± 0.04 for orientation 3 (θ = 90°), and R_1:R_2 = 0.59 ± 0.03 for orientation 4 (θ = 90°).

It is now apparent that R_1:R_2 = 0.76 ± 0.05 for ρ = 0.58 ± 0.03 (orientation 1; emission direction (θ) = 56°) and that the average R_1:R_2 = 0.60 ± 0.02 for ρ = 0.71 ± 0.02 (orientations 2–4; emission direction (θ) = 90°), *i.e.*, the R_1:R_2 ratio is different when probed in the direction of θ = 56° (R_1:R_2 = 0.76 ± 0.05) *vs*. when it is probed in the direction of θ = 90° (average R_1:R_2 = 0.60 ± 0.02). Furthermore, it is also tempting to point out that the change in the intensity ratio between the green ($^4S_{3/2} \rightarrow {}^4I_{15/2}$; 541–566 nm) and red ($^4F_{9/2} \rightarrow {}^4I_{15/2}$; 648–674 nm) emission bands also follows a similar trend: G:R = 0.32 ± 0.08 for orientation 1 (θ = 56°), G:R = 0.40 ± 0.22 for orientation 2 (θ = 90°), G:R = 0.40 ± 0.19 for orientation 3 (θ = 90°), and G:R = 0.43 ± 0.14 for orientation 4 (θ = 90°), *i.e.*, the G:R ratio is different when probed in the direction of θ = 56° (G:R = 0.32 ± 0.08) *vs*. when it is probed in the direction of θ = 90° (average G:R = 0.41 ± 0.11). However, because the intensity ratio between the green and red bands of Er^{3+} is power density-dependent (and because the different particle orientations were obtained by means of manipulating the laser focus, *i.e.*, power density), the latter set of evidence concerning the observed change in the G:R ratio as a function of emission direction should be treated with caution.[52] Nevertheless, even on the basis of the evidence concerning the change in the R_1:R_2 ratio, it may be postulated that the change in the degree of polarization (ρ) is associated with the change in emission intensity as a function of emission direction relative to the optic axis.

Postulated association aside, the fact that this study also revealed that the intensity of the probed emission bands, *i.e.*, the probability of the respective electronic transitions, appears to be dependent on the emission direction relative to the optic axis provides confirmation for the results obtained *via* hyperspectral imaging (*vide supra* **Section 4.3.1**). However, if one is to *i*) also accept the postulated association between the emission direction-dependent change in the degree of polarization (ρ) and the respective change in emission band intensity (irrespective of the dopant system), and *ii*) consider that different selection rules with respect to polarization may govern the various electronic transitions

that manifest as the herein probed emission bands, then the following tentative conclusion may be drawn – the difference in the degree of emission intensity change for the blue (40%), red (32%), and NIR (31%) bands stemming from the neutrally *vs*. non neutrally oriented $LiYF_4:Yb^{3+}/Tm^{3+}$ microparticles subjected to hyperspectral imaging is a product of the emission direction-dependent difference in the degree of polarization (*vide supra* **Figure 38**). More broadly, the observed change in the degree of polarization as a function of emission direction relative to the optic axis of a $LiYF_4$ microparticle may provide a plausible explanation for the accompanying spatial emission band intensity variation observed *via* both hyperspectral imaging and single-particle polarized emission spectroscopy conducted inside an optical trap.

On a different note, it is interesting to point out that optical trapping of differently-sized $LiYF_4:RE^{3+}$ microparticles revealed that the number of possible $LiYF_4:RE^{3+}$ microparticle orientations inside an optical trap appeared to be inversely proportional to their size – the relatively large $LiYF_4:Yb^{3+}/Er^{3+}$ microparticles could be trapped in four stable orientations (№1–4), intermediately-sized $LiYF_4:Yb^{3+}/Tm^{3+}$ microparticles could be trapped in two stable orientations (№2 and 3), and only one stable orientation (№3) was observed when trapping the smaller $LiYF_4:Nd^{3+}$ microparticles. It is also interesting to note that a particle orientation in which the optic axis aligned parallel with the direction of laser propagation was not observed, since probing for polarized emission in this orientation would yield a perfectly circular polar plot, *i.e.*, emission generated parallel to the optic axis is not polarized.[60]

These observations are in line with previously reported simulations, which revealed that the most stable orientation for a square-based bipyramidal $LiYF_4$ particle with dimensions of 7.6 μm by 5.5 μm (AR *ca*. 1.4) in water would be obtained if its optic axis aligned orthogonally with the laser propagation direction ($OA \perp \vec{K}$), whereas the most stable orientation for a particle with dimensions of 200 nm by 143 nm (AR = 1.4) would be obtained if its optic axis aligned parallel with the laser propagation direction ($OA \parallel \vec{K}$).[87] Ultimately, this explains why all of the $LiYF_4:RE^{3+}$ microparticles involved in this work exhibited the "$OA \perp \vec{K}$" orientation and why none of the particles exhibited the "$OA \parallel \vec{K}$" orientation, for which they were all insufficiently small.

In general, a stable particle orientation inside an optical trap is achieved when the optical forces and torques exerted by the highly focused trapping radiation achieve an equilibrium.[60,87] Consequently, factors such as radiation wavelength and power density, as well as material composition, size, and geometric shape of the particle greatly influence particle behaviour inside an optical trap.[69] Interestingly, the largest $LiYF_4:Yb^{3+}/Er^{3+}$ microparticles (4.4 ± 0.4 μm by 4.0 ± 0.2 μm) exhibited at least three different laser focus-dependent spatial orientations, allowing for polarized emission to be probed oblique to the optic axis as well as perpendicular to it. This is a valuable observation because the more commonly investigated β-$NaYF_4$ particles of various sizes and morphologies offer only two spatial orientations inside the optical trap: one that allows for emission to be probed parallel to the optic axis (a direction in which the emission is not polarized), and another perpendicular to it.[60,69] Overall, experimental insight regarding the relationship between particle size and orientation inside an optical trap may be useful for future investigations involving optical trapping of square-based bipyramidal $LiYF_4:RE^{3+}$ microparticles.

4.4. Summary of Chapter 4

The optical characterization study discussed in the first section of this chapter confirmed good upconverting capabilities of the reported $LiYF_4:Yb^{3+}/Tm^{3+}$, $LiYF_4:Yb^{3+}/Er^{3+}$, and $LiYbF_4:Er^{3+}$ microparticles, the α-$NaYF_4:Yb^{3+}/Er^{3+}$ and β-$NaGdF_4:Yb^{3+}/Er^{3+}$ nanoparticles, as well as good downshifting capabilities of the $LiYF_4:Ce^{3+}/Tb^{3+}$ microparticles.

Hyperspectral imaging revealed that $LiYF_4$ microparticles featuring the Yb^{3+}/Er^{3+} and Yb^{3+}/Tm^{3+} dopant systems exhibit non-uniform spatial emission intensity distribution. A single-particle polarized emission spectroscopy study conducted in collaboration with the Fluorescent Imaging Group of the Universidad Autónoma de Madrid confirmed that both upconverted and downshifted emission stemming from the $LiYF_4:Yb^{3+}/Er^{3+}$ and $LiYF_4:Yb^{3+}/Tm^{3+}$ microparticles, as well as the $LiYF_4:Nd^{3+}$ microparticles, respectively, was polarized in at least one direction. Optical trapping and subsequent manipulation of the spatial particle orientation was employed in order to gain greater insight into how the

polarized emission stemming from a single $LiYF_4:Yb^{3+}/Er^{3+}$ microparticle changes as a function of emission direction. It was determined that the degree of emission polarization (measured by the polarizability constant ρ) and the emission band intensity (and hence, the probability of the respective electronic transitions) changes as a function of emission direction relative to the optic axis. It was concluded that these results provide a plausible explanation for the variation in spatial emission intensity observed *via* hyperspectral imaging.

Lastly, optical trapping of the differently-sized $LiYF_4:RE^{3+}$ microparticles revealed an inverse relationship between particle size and the number of possible spatial orientations inside the optical trap.

Chapter 5. Summary and outlook

5.1. Summary

Continuous development, optimization and subsequent application of novel functional materials is made possible only through rigorous investigation and understanding of their underlying physical and chemical properties. Taking into account the importance of fundamental research, this research project aimed to expand the scope of luminescent $M(RE)F_4$ (M = Li, Na; RE = Gd, Yb, Y) materials that could be accessed by a rapid microwave-assisted solvothermal synthesis method and to provide greater insight into the luminescence properties of $LiYF_4:RE^{3+}$ microparticles, specifically.

Chapter 3 described the development of a microwave-assisted solvothermal synthesis route toward $LiYF_4:RE^{3+}$ microparticles exhibiting upconversion and downshifting luminescence. Salient characteristics of this approach are the significantly reduced reaction duration (as short as 2 min *vs.* ≥ 12 h), the *in-situ* surface functionalization with acetate groups allowing for applications in aqueous media, and the use of inexpensive and more environmentally benign solvents, *i.e.*, ethanol and water. Furthermore, the versatility of this method was highlighted by extending it toward the preparation of other state-of-the-art $M(RE)F_4$ micro- ($LiYbF_4$) and nanoscale (α-$NaYF_4$, and β-$NaGdF_4$) materials. The synthesis method was developed by means of rigorous control of multiple physicochemical reaction parameters: $M^+:RE^{3+}$ ratio, pH of the initial reaction mixture, and reaction temperature/duration profile. The $LiYF_4$ particle growth mechanism under optimal microwave-assisted solvothermal conditions was also investigated, revealing a phase transformation from $Y_X(NH_4)_YF_Z$ to $LiYF_4$ and the subsequent ripening of the $LiYF_4$ microparticles. Lastly, a critical review of potential challenges associated with microwave-assisted synthesis was provided along with possible solutions.

Chapter 4 provided an overview of the upconverting and downshifting capabilities of the respective materials. Hyperspectral imaging and single-particle polarized emission spectroscopy revealed and provided a plausible explanation for the existence of spatial variation in emission intensity within individual $LiYF_4;RE^{3+}$ microparticles. Optical

trapping of differently-sized $LiYF_4;RE^{3+}$ microparticles revealed an inverse relationship between particle size and the number of possible spatial orientations inside the optical trap.

5.2. Outlook

In December of 2016, Bernard Feringa delivered a Nobel Lecture titled "The Art of Building Small: from Molecular Switches to Motors",[126] in which he emphasized the importance of rational design in the development of light-fueled "machines", *e.g.*, motors, rotors, switches, and pumps, and the necessity for understanding the intricacies of light-matter interactions that govern their autonomous function (light-induced physical motion). Indeed, Feringa's Nobel Prize in Chemistry signifies the prominence of optically active molecules and materials in science, ever increasing attention to which is generating a broad range of potential and actualized applications.

Optical trapping is a technique that can be leveraged in order to harness the benefits of light-induced physical motion (also a technique that earned Arthur Ashkin the 2018 Nobel Prize in Physics).[127] In this thesis, the utility of optical trapping in investigating direction-dependent polarized emission stemming from microscale crystalline particles has been demonstrated. However, optical trapping can offer much more. Specifically, an optical trap that is generated by a circularly-polarized laser can induce rotation of nano/microscale particles characterized by uniaxial crystallinity, *e.g.*, $Na(RE)F_4$ and $Li(RE)F_4$. For example, the Fluorescence Imaging Group of the Universidad Autónoma de Madrid has already developed $NaYF_4:RE^{3+}$ microrotors, rotational frequency of which can be leveraged for precise *in-vitro* temperature sensing and detection of bacteria.[67] Next, it would be intriguing to leverage the square-based bipyramidal morphology of the $LiYF_4$ microparticles for drilling at the microscale. It is conceivable that drilling though a cell membrane with a $LiYF_4$ microparticle can allow one to study the cellular response to mechanical stress.[128] Furthermore, combining light-induced rotation with the optical properties of the REs can enable even more complex applications. For example, it is intriguing to invoke $LiYF_4$ microparticles (or other $M(RE)F_4$ particles) with a relatively high Nd^{3+} content (*ca*. 25%) as NIR photon counters. An increase in Nd^{3+} doping

concentration has been shown to promote cross-relaxation that fosters non-radiative relaxation, *i.e.*, generation of heat.[129] Hence, it is conceivable that quantum yield can be inferred from the rise and subsequent equilibration of local temperature upon optical trapping, rotation, and excitation of a single $LiYF_4:Nd^{3+}$ microparticle with circularly-polarized radiation (*e.g.*, λ_{EX} = 808 nm) in aqueous media.[130] The local temperature of the medium can be inferred from its viscosity, and viscosity can be inferred form the rotational frequency of the microparticle. I am excited to state that both of these projects are part of a future collaboration plan between the Hemmer Group of uOttawa and the Fluorescence Imaging Group of the Universidad Autónoma de Madrid. In fact, preliminary studies have already revealed their feasibility.

On a different note, bright $LiYF_4:RE^{3+}$ microparticles presented in this work could also serve as excellent candidates in applications such as photocatalysis, anticounterfeiting, and colour-tunable phosphors. And last but not least, the herein presented microwave-assisted solvothermal synthesis approach can be leveraged to provide rapid access not only to the materials reported herein, but likely to other crystalline materials as well. Furthermore, it is my hope that the systematic approach toward optimizing the physicochemical reaction parameters undertaken in the context of this work will inspire others to develop even more rapid, reliable, and versatile microwave-assisted syntheses that yield useful RE-based materials.

Bibliography

1. Bünzli, J.-C. G. Lanthanide Photonics: Shaping the Nanoworld. *Trends Chem.* **2019**, *1*, 751–762.

2. Jha, M. K. *et al.* Review on Hydrometallurgical Recovery of Rare-Earth Metals. *Hydrometallurgy* **2016**, *165*, 2–26.

3. Dinér, P. Yttrium from Ytterby. *Nat. Chem.* **2016**, *8*, 192.

4. Bünzli, J.-C. G. Rising Stars in Science and Technology: Luminescent Lanthanide Materials. *Eur. J. Inorg. Chem.* **2017**, *2017*, 5058–5063.

5. Meijerink, A. and Wegh, R. T. VUV Spectroscopy of Lanthanides: Extending the Horizon. *Mater. Sci. Forum* **1999**, *315–317*, 11–26.

6. Dieke, G. H., Crosswhite, H. M., and Dunn, B. Emission Spectra of the Doubly and Triply Ionized Rare-Earths. *J. Opt. Soc. Am.* **1961**, *51*, 820.

7. Vleck, J. H. V. The Puzzle of Rare-Earth Spectra in Solids. *J. Phys. Chem.* **1937**, *41*, 67–80.

8. Judd, B. R. Optical Absorption Intensities of Rare-Earth Ions. *Phys. Rev.* **1962**, *127*, 750–761.

9. Ofelt, G. S. Intensities of Crystal Spectra of Rare-Earth Ions. *J. Chem. Phys.* **1962**, *37*, 511–520.

10. De Bettencourt-Dias, A. The Electronic Structure of the Lanthanides in *The Rare Earth Elements: Fundamentals and Applications*, pg. 27–33, ed. Atwood, D. A., John Wiley and Sons, Ltd., **2012**.

11. Setlur, A. A. *et al.* Crystal Chemistry and Luminescence of Ce^{3+}-Doped $Lu_2CaMg_2(Si,Ge)_3O_{12}$ and Its Use in LED Based Lighting. *Chem. Mater.* **2006**, *18*, 3314–3322.

12. Li, L., Zhou, S., and Zhang, S. Investigation on Charge Transfer Bands of Ce^{4+} in Sr_2CeO_4 Blue Phosphor. *Chem. Phys. Lett.* **2008**, *453*, 283–289.

13. DeLoach, L. D. *et al.* Evaluation of Absorption and Emission Properties of Yb^{3+} Doped Crystals for Laser Applications. *IEEE J. Quantum Electron.* **1993**, *29*, 1179–1191.

14. Henke, M., Perßon, J., and Kück, S. Preparation and Spectroscopy of Yb^{2+}-doped $Y_3Al_5O_{12}$, $YAlO_3$, and $LiBaF_3$. *J. Lumin.* **2000**, *87*, 1049–1051.

15. Bünzli, J.-C. G. Lanthanide Luminescence: From a Mystery to Rationalization, Understanding, and Applications in *Handbook on the Physics and Chemistry of Rare Earths*, pg. 142–171, Elsevier B.V., **2016**.

16. De Bettencourt-Dias, A. Introduction to Lanthanide Ion Luminescence in *Luminescence of Lanthanide Ions in Coordination Compounds and Nanomaterials*, pg. 1–46, ed. De Bettencourt-Dias, A., John Wiley and Sons, Ltd., **2014**.

17. Chen, X. A General Introduction to Lanthanide Ions in *Lanthanide-Doped Luminescent Nanomaterials: From Fundamentals to Bioapplications*, pg. 1–15, Springer-Verlag Berlin Heidelberg, **2014**.

18. Walsh, B. M., Barnes, N. P., and Di Bartolo, B. Branching Ratios, Cross Sections, and Radiative Lifetimes of Rare-Earth Ions in Solids: Application to Tm^{3+} and Ho^{3+} Ions in $LiYF_4$. *J. Appl. Phys.* **1998**, *83*, 2772–2787.

19. Cotton, S. A. Lanthanides: Comparison to 3d metals in *The Rare Earth Elements: Fundamentals and Applications*, pg. 105–109, ed. Atwood, D. A., John Wiley and Sons Ltd., **2012**.

20. Sahu, N. K. *et al*. Ce^{3+}-Sensitized GdPO4:Tb^{3+} Nanorods: An Investigation on Energy Transfer, Luminescence Switching, and Quantum Yield. *ACS Photonics* **2014**, *1*, 337–346.

21. Gao, D., Zhang, X., and Zhang, J. The Effects of Structural Characterization on the Luminescence of Eu^{3+}-Doped Fluoride Nano/Microcrystals. *CrystEngComm* **2014**, *16*, 11115–11121.

22. Mahalingam, V. *et al*. Colloidal Tm^{3+}/Yb^{3+}-Doped $LiYF_4$ Nanocrystals: Multiple Luminescence Spanning the UV to NIR Regions *via* Low-Energy Excitation. *Adv. Mater.* **2009**, *21*, 4025–4028.

23. Auzel, F. Upconversion and Anti-Stokes Processes with f and d Ions in Solids. *Chem. Rev.* **2004**, *104*, 139–174.

24. Yu, D.-C. *et al*. Multi-Photon Quantum Cutting in Gd_2O_2S:Tm^{3+} to Enhance the Photo-Response of Solar Cells. *Sci. Appl.* **2015**, *4*, 344.

25. Wegh, R. T. *et al*. Quantum Cutting Through Downconversion in Rare-Earth Compounds. *J. Lumin.* **2000**, *87*, 1017–1019.

26. Rocha, U. *et al.* Neodymium-Doped LaF_3 Nanoparticles for Fluorescence Bioimaging in the Second Biological Window. *Small* **2014**, *10*, 1141–1154.

27. Del Rosal, B. *et al.* Neodymium-Doped Nanoparticles for Infrared Fluorescence Bioimaging: The Role of the Host. *J. Appl. Phys.* **2015**, *118*, 143104.

28. Rocha, U. *et al.* Subtissue Thermal Sensing Based on Neodymium-Doped LaF_3 Nanoparticles. *ACS Nano* **2013**, *7*, 1188–1199.

29. Kim, S. Y., Won, Y. H., and Jang, H. S. A Strategy to Enhance Eu^{3+} Emission From $LiYF_4:Eu^{3+}$ Nanophosphors and Green-to-Orange Multicolor Tunable, Transparent Nanophosphor-Polymer Composites. *Sci. Rep.* **2015**, *5*, 1–11.

30. Hemmer, E. *et al.* Upconverting and NIR Emitting Rare-Earth Based Nanostructures for NIR-Bioimaging. *Nanoscale* **2013**, *5*, 11339–11361.

31. Chen, G. *et al.* (α-$NaYbF_4:Tm^{3+}$)/CaF_2 Core/Shell Nanoparticles with Efficient Near-Infrared to Near-Infrared Upconversion for High-Contrast Deep Tissue Bioimaging. *ACS Nano* **2012**, *6*, 8280–8287.

32. Kim, S. Y. *et al*. Direct Observation of the Core/Double-Shell Architecture of Intense Dual-Mode Luminescent Tetragonal Bipyramidal Nanophosphors. *Nanoscale* **2016**, *8*, 10049–10058.

33. Kiliaan, H. S., Kotte, J. F. A. K., and Blasse, G. Energy Transfer in the Luminescent System $Na(Y,Gd)F_4:Ce^{3+},Tb^{3+}$. *J. Electrochem. Soc.* **1987**, *134*, 2359–2364.

34. Van Der Ende, B. M., Aarts, L., and Meijerink, A. Lanthanide Ions as Spectral Converters For Solar Cells. *Phys. Chem. Chem. Phys.* **2009**, *11*, 11081–11095.

35. Wang, F. *et al*. Multicolour PEI/NaGdF4:Ce^{3+},Ln^{3+} Nanocrystals By Single-Wavelength Excitation. *Nanotechnology* **2007**, *18*, 025701.

36. Van Veggel, F. Upconversion of Ln^{3+}-based Nanoparticles for Optical Bio-Imaging in *Luminescence of Lanthanide Ions in Coordination Compounds and Nanomaterials*, pg. 269–295, ed. De Bettencourt-Dias, A., John Wiley and Sons, Ltd., **2014**.

37. Berezin, M. Y. and Achilefu, S. Fluorescence Lifetime Measurements and Biological Imaging. *Chem. Rev.* **2010**, *110*, 2641–2684.

38. Wang, F. *et al.* Tuning upconversion through energy migration in core-shell nanoparticles. *Nat. Mater.* **2011**, *10*, 968–973.

39. Mai, H.-X. *et al*. Highly Efficient Multicolor Up-Conversion Emissions and Their Mechanisms of Monodisperse $NaYF_4$:Yb,Er Core and Core/Shell-Structured Nanocrystals. *J. Phys. Chem. C.* **2007**, *111*, 13721–13729.

40. Bettinelli, M., Carlos, L., and Liu, X. Lanthanide-Doped Upconversion Nanoparticles. *Phys. Today* **2015**, *68*, 38–44.

41. Chen, S. *et al.* Near-Infrared Deep Brain Stimulation Via Upconversion Nanoparticle-Mediated Optogenetics. *Science* **2018**, *359*, 679–684.

42. Haase, M. and Schäfer, H. Upconverting Nanoparticles. *Angew. Chem. Int. Ed.* **2011**, *50*, 5808–5829.

43. Jiang, X. *et al*. Nd^{3+}-Doped $LiYF_4$ Nanocrystals For Bio-Imaging in the Second Near-Infrared Window. *J. Mater. Chem. B.* **2016**, *4*, 87–95.

44. Tu, D. *et al.* Breakdown of Crystallographic Site Symmetry in Lanthanide-Doped $NaYF_4$ Crystals. *Angew. Chem. Int. Ed.* **2013**, *52*, 1128–1133.

45. Cheng, J. *et al*. Crystal-Field Analyses For Trivalent Lanthanide Ions in $LiYF_4$. *J. Rare Earths* **2016**, *34*, 1048–1052.

46. Li, C. *et al*. Highly Uniform and Monodisperse β-$NaYF_4$:Ln^{3+} (Ln = Eu, Tb, Yb/Er, and Yb/Tm) Hexagonal Microprism Crystals: Hydrothermal Synthesis and Luminescent Properties. *Inorg. Chem.* **2007**, *46*, 6329–6337.

47. Wisser, M. D. *et al.* Strain-Induced Modification of Optical Selection Rules in Lanthanide-Based Upconverting Nanoparticles. *Nano Lett.* **2015**, *15*, 1891–1897.

48. Wang, L. *et al.* A New Cubic Phase for a $NaYF_4$ Host Matrix Offering High Upconversion Luminescence Efficiency. *Adv. Mater.* **2015**, *27*, 5528–5533.

49. Xue, X. *et al.* Size-Dependent Upconversion Luminescence and Quenching Mechanism of $LiYF_4$:Er^{3+}/Yb^{3+} Nanocrystals with Oleate Ligand Adsorbed. *Opt. Mater. Express* **2013**, *3*, 989.

50. Cheng, T. *et al*. Small and Bright Lithium-Based Upconverting Nanoparticles. *J. Am. Chem. Soc.* **2018**, *140*, 12890–12899.

51. Homann, C. *et al.* $NaYF_4$:Yb,Er/$NaYF_4$ Core/Shell Nanocrystals with High Upconversion Luminescence Quantum Yield. *Angew. Chem. Int. Ed.* **2018**, *57*, 8765–8769.

52. Würth, C. *et al.* Excitation Power Dependent Population Pathways and Absolute Quantum Yields of Upconversion Nanoparticles in Different Solvents. *Nanoscale* **2017**, *9*, 4283–4294.

53. Dong, X. *et al.* A Review of Hyperspectral Imaging for Nanoscale Materials Research. *Appl. Spectroscop. Rev.* **2019**, *54*, 285–305.

54. Krupnik, D. and Khan, S. Close-Range, Ground-Based Hyperspectral Imaging for Mining Applications at Various Scales: Review and Case Studies. *Earth-Sci. Rev.* **2019**, *198*, 102952.

55. Nadort, A. *et al.* Quantitative Imaging of Single Upconversion Nanoparticles in Biological Tissue. *PLoS One* **2013**, *8*, e63292.

56. Debasu, M. L. *et al.* Nanoplatforms for Plasmon-Induced Heating and Thermometry. *ChemNanoMat* **2016**, *2*, 520–527.

57. Ovens, J. S. PhD Thesis. An In-Depth Examination of the Properties and Behaviour of Au(III)-based [AuX2(CN)2] (X = Cl, Br, I) as a Coordination Polymer Building Block. Simon Fraser University, 2015.

58. Chen, P. *et al.* Polarization Modulated Upconversion Luminescence: Single Particle *vs*. Few-Particle Aggregates. *Nanoscale* **2015**, *7*, 6462–6466.

59. Chen, X. Appendix 1: Selection Rules for Induced Electric Dipole and Magnetic Dipole Transitions of Lanthanide Ions in *Lanthanide-Doped Luminescent Nanomaterials: From Fundamentals to Bioapplications*, pg. 193–199, ed. Chen, X., Springer-Verlag Berlin Heidelberg, **2014**.

60. Rodríguez-Sevilla, P. *et al.* Optical Torques on Upconverting Particles for Intracellular Microrheometry. *Nano Lett.* **2016**, *16*, 8005–8014.

61. Payne, S. A. *et al*. Infrared Cross-Section Measurements for Crystals Doped with Er^{3+}, Tm^{3+}, and Ho^{3+}. *IEEE J. Quantum Electron.* **1992**, *28*, 2619–2630.

62. Ashkin, A. Forces of a Single-Beam Gradient Laser Trap on a Dielectric Sphere in the Ray Optics Regime. *Biophys. J.* **1992**, *61*, 569–582.

63. Ashkin, A. *et al*. Observation of a Single-Beam Gradient Force Optical Trap for Dielectric Particles. *Opt. Lett.* **1986**, *11*, 196–198.

64. Rodríguez-Sevilla, P. *et al*. Optical Trapping for Biosensing: Materials and Applications. *J. Mater. Chem. B.* **2017**, *5*, 9085–9101.

65. Rodríguez-Sevilla, P. *et al.* Assessing Single Upconverting Nanoparticle Luminescence by Optical Tweezers. *Nano Lett.* **2015**, *15*, 5068–5074.

66. Rodríguez-Sevilla, P. *et al*. The Temperature of an Optically Trapped, Rotating Microparticle. *ACS Photonics* **2018**, *5*, 3772–3778.

67. Rodriguez-Sevilla, P. *et al.* Light-Activated Upconverting Spinners. *Adv. Opt. Mater.* **2018**, *6*, 1800161.

68. Rodríguez-Sevilla, P. *et al.* Thermal Scanning at the Cellular Level by an Optically Trapped Upconverting Fluorescent Particle. *Adv. Mater.* **2016**, *28*, 2421–2426.

69. Rodríguez-Sevilla, P. *et al.* Determining the 3D Orientation of Optically Trapped Upconverting Nanorods by in Situ Single-Particle Polarized Spectroscopy. *Nanoscale* **2016**, *8*, 300–308.

70. J. Jiefu. Upconversion Nanoparticles for Bioimaging Applications in *The Rare Earth Elements: Fundamentals and Applications*, pg. 389–404, ed. Atwood, D. A., John Wiley and Sons Ltd., **2012**.

71. Yan, C. *et al*. Lanthanide Ion Doped Upconverting Nanoparticles: Synthesis, Structure and Properties. *Small* **2016**, *12*, 3888–3907.

72. Wang, H.-Q. Upconverting Nanoparticles in *Lanthanide Luminescence Photophysical, Analytical and Biological Aspects*, pg. 115–132, ed. Hanninen, Pekka, Springer-Verlag Berlin Heidelberg, **2011**.

73. Baghbanzadeh, M. *et al*. Microwave-Assisted Synthesis of Colloidal Inorganic Nanocrystals. *Angew. Chem. Int. Ed.* **2011**, *50*, 11312–11359.

74. Mai, H.-X. *et al.* High-Quality Sodium Rare-Earth Fluoride Nanocrystals: Controlled Synthesis and Optical Properties. *J. Am. Chem. Soc.* **2006**, *128*, 6426–6436.

75. Wang, F. *et al.* Simultaneous Phase and Size Control of Upconversion Nanocrystals Through Lanthanide Doping. *Nature* **2010**, *463*, 1061–1065.

76. Gao, W. *et al*. Luminescence Investigation of Yb^{3+}/Er^{3+} Co-Doped Single $LiYF_4$ Microparticle. *J. Lumin.* **2014**, *152*, 44–48.

77. Bilecka, I. and Niederberger, M. Microwave Chemistry for Inorganic Nanomaterials Synthesis. *Nanoscale* **2010**, *2*, 1358–1374.

78. Kappe, C. O. Unraveling the Mysteries of Microwave Chemistry Using Silicon Carbide Reactor Technology. *Acc. Chem. Res.* **2013**, *46*, 1579–1587.

79. Halimi, I. *et al.* Pick Your Precursor! Tailoring the Size and Crystal Phase of Microwave-Synthesized Sub-10 nm Upconverting Nanoparticles. *J. Mater. Chem. C.* **2019**, *7*, 15364–15374.

80. Yi, G. S. and Chow, G. M. Synthesis of Hexagonal-Phase $NaYF_4$:Yb,Er and $NaYF_4$:Yb,Tm Nanocrystals with Efficient Up-Conversion Fluorescence. *Adv. Funct. Mater.* **2006**, *16*, 2324–2329.

81. Boyer, J.-C., Cuccia, L. A., and Capobianco J. A., Synthesis of Colloidal Upconverting $NaYF_4:Er^{3+}/Yb^{3+}$ and Tm^{3+}/Yb^{3+} Monodisperse Nanocrystals. *Nano Lett.* **2007**, *7*, 847–852.

82. De Leebeeck, H., Binnemans, K., and Görller-Walrand, C. Magneto-Optical Properties of Neodymium-Doped $LiYF_4$. *J. Alloys Compd.* **1999**, *291*, 300–311.

83. Xue, X. *et al*. "Size-Dependent Luminescence of Nd^{3+}-Doped $LiYF_4$ Nanocrystals" in *Frontiers in Optics 2013*, ed. Kang, I. *et al.*, OSA Technical Digest (online) (Optical Society of America, 2013), paper FTu3A.19.

84. Zhou, A. *et al.* Simultaneous Size Adjustment and Upconversion Luminescence Enhancement of β-$NaLuF_4:Yb^{3+}/Er^{3+}$, Yb^{3+}/Tm^{3+} Microcrystals by Introducing Ca^{2+} for Temperature Sensing. *CrystEngComm* **2018**, *20*, 2029–2035.

85. Wu, T. *et al.* Synthesis and Photocatalytic Activity of Hexagonal Phase $NaYF_4:Ho^{3+}@TiO_2$ Core-Shell Microcrystals. *CrystEngComm* **2016**, *18*, 6471–6482.

86. Yao, W. *et al.* Preparation and RGB Upconversion Optic Properties of Transparent Anti-Counterfeiting Films. *Nanoscale* **2017**, *9*, 15982–15989.

87. Roder, P. B. *et al*. Laser Refrigeration of Hydrothermal Nanocrystals in Physiological Media. *Proc. Natl. Acad. Sci. U. S. A.* **2015**, *112*, 15024–15029.

88. Ullah, S. *et al.* Microwave-Assisted Synthesis of $NaYF_4:Yb^{3+}/Tm^{3+}$ Upconversion Particles with Tailored Morphology and Phase for the Design of UV/NIR-Active $NaYF_4:Yb^{3+}/Tm^{3+}@TiO_2$ Core@Shell Photocatalysts. *CrystEngComm* **2017**, *19*, 3465–3475.

89. Chen, C. *et al.* Ionic Liquid-Based Route to Spherical $NaYF_4$ Nanoclusters with the Assistance of Microwave Radiation and Their Multicolor Upconversion Luminescence. *Langmuir* **2010**, *26*, 8797–8803.

90. Quintanilla, M. *et al*. Light Management in Upconverting Nanoparticles: Ultrasmall Core/Shell Architectures to Tune the Emission Color. *ACS Photonics* **2014**, *1*, 662–669.

91. Lorbeer, C. *et al*. Charge Compensation in RE^{3+} (RE = Eu, Gd) and M^+ (M = Li, Na, K) Co-Doped Alkaline Earth Nanofluorides Obtained by Microwave Reaction with Reactive Ionic Liquids Leading to Improved Optical Properties. *J. Mater. Chem. C*. **2014**, *2*, 9439–9450.

92. Reddy, K. L. *et al*. Microwave-Assisted One-Step Synthesis of Acetate-Capped $NaYF_4$:Yb/Er Upconversion Nanocrystals and Their Application in Bioimaging. *J. Mater. Sci.* **2017**, *52*, 5738–5750.

93. Tong, L. *et al.* Comparative Study on Upconversion Luminescence and Temperature Sensing of α- and β-$NaYF_4$:Yb^{3+}/Er^{3+} Nano-/Micro-Crystals Derived From a Microwave-Assisted Hydrothermal Route. *J. Lumin.* **2015**, *167*, 386–390.

94. Wang, D. *et al.* Rapid Microwave-Enhanced Hydrothermal Synthesis and Shape Evolution of Uniform $NaGdF_4$:Yb, Er (Tm/Ho) Nanocrystals with Upconversion and Paramagnetic Properties. *Nanotechnology* **2012**, *23*, 225705.

95. Wang, H. Q., Tilley, R. D., and Nann, T. Size and Shape Evolution of Upconverting Nanoparticles Using Microwave Assisted Synthesis. *CrystEngComm* **2010**, *12*, 1993–1996.

96. Andrade, A. B. *et al*. Synthesis and Characterization of Luminescent Ln^{3+} (Ln = Eu, Tb and Dy)-Doped $LiYF_4$ Microcrystals Produced by a Facile Microwave-Assisted Hydrothermal Method. *J. Lumin.* **2020**, *219*, 116843.

97. Chen, G. *et al*. Intense Visible and Near-Infrared Upconversion Photoluminescence in Colloidal $LiYF_4$:Er^{3+} Nanocrystals Under Excitation at 1490 nm. *ACS Nano* **2011**, *5*, 4981–4986.

98. Du, Y. P. *et al*. Optically Active Uniform Potassium and Lithium Rare Earth Fluoride Nanocrystals Derived from Metal Trifluroacetate Precursors. *J. Chem. Soc. Dalt. Trans.* **2009**, 8574–8581.

99. Wang, J. *et al.* Lanthanide-Doped $LiYF_4$ Nanoparticles: Synthesis and Multicolor Upconversion Tuning. *Comptes Rendus Chim.* **2010**, *13*, 731–736.

100. Liu, S. *et al.* Oleic Acid-Modified $LiYF_4$:Er,Yb Nanocrystals for Potential Optical-Amplification Applications. *J. Nanosci. Nanotechnol.* **2014**, *14*, 3718–3721.

101. Zhang, Q. and Yan, B. Hydrothermal Synthesis and Characterization of $LiREF_4$ (RE = Y, Tb−Lu) Nanocrystals and Their Core-Shell Nanostructures. *Inorg. Chem.* **2010**, *49*, 6834–6839.

102. Bogdan, N. *et al*. Synthesis of Ligand-Free Colloidally Stable Water Dispersible Brightly Luminescent Lanthanide-Doped Upconverting Nanoparticles. *Nano Lett.* **2011**, *11*, 835–840.

103. Zhang, X., Wang, M., and Ding, J. Shape-Selective Synthesis, Characterization and Upconversion Improvement of Yb^{3+}/Er^{3+} Doped $LiYF_4$ Microphosphors Through pH Tuning. *RSC Adv.* **2014**, *4*, 29165–29172.

104. Capello, C., Fischer, U., and Hungerbühler, K. What is a Green Solvent? A Comprehensive Framework for the Environmental Assessment of Solvents. *Green Chem.* **2007**, *9*, 927–934.

105. Henderson, R. K. *et al.* Expanding GSK's Solvent Selection Guide - Embedding Sustainability Into Solvent Selection Starting at Medicinal Chemistry. *Green Chem.* **2011**, *13*, 854–862.

106. Song, Y. *et al.* Phase and luminescent intensity control of hydrophilic rare-earth up-converting nanophosphors prepared by one-pot solvothermal synthesis. *J. Alloys Compd.* **2011**, *509*, 6539–6544.

107. Lutterotti, L.; Wenk, H.; Matthies, S. MAUD: A Friendly Java Program for Material Analysis Using Diffraction. *Proc. Twelfth International Conference on Textures of Materials (ICOTOM 12)*, Montreal (Canada) **1999**, 1599.

108. Na, H. *et al.* Facile Synthesis of Intense Green Light Emitting $LiGdF_4$:Yb,Er-Based Upconversion Bipyramidal Nanocrystals and Their Polymer Composites. *Nanoscale* **2014**, *6*, 7461–7468.

109. LaMer, V. K. and Dinegar, R. H. Theory, Production and Mechanism of Formation of Monodispersed Hydrosols. *J. Am. Chem. Soc.* **1950**, *72*, 4847–4854.

110. Speakman, S. A. *Basics of X-Ray Powder Diffraction Training to Become an Independent User of the X-Ray SEF at the Center for Materials Science and Engineering at MIT*. http://prism.mit.edu/xray/Basics%20of%20X-Ray%20Powder%20Diffraction.pdf

111. Tian, L. *et al.* Hydrothermal Synthesis and Formation Mechanism of Hexagonal Yttrium Hydroxide Fluoride Nanobundles. *Mater. Res. Bull.* **2013**, *48*, 4481–4485.

112. Shao, B. *et al.* Novel Two-Step Topotactic Transformation Synthetic Route Towards Monodisperse LnOF:Re^{3+} (Ln = Y, Pr-Lu) Nanocrystals with Down/Upconversion Luminescence Properties. *Adv. Opt. Mater.* **2015**, *3*, 583–592.

113. Liu, B. *et al.* Synthesis, Characterization and Luminescent Properties of Needle-Like Lanthanide-Doped Orthorhombic $Y_5O_4F_7$. *J. Rare Earths* **2013**, *31*, 745–749.

114. Wang, H. Q. and Nann, T. Monodisperse Upconverting Nanocrystals by Microwave-Assisted Synthesis. *ACS Nano* **2009**, *3*, 3804–3808.

115. Mukherjee, A., Mishra, S., and Krishnamurthy, N. Thermogravimetric Studies and Kinetics of Decomposition of Ammonium Yttrium Fluoride. *React. Kinet. Mech. Catal.* **2011**, *103*, 53–70.

116. Wang, Y. *et al*. Thermodynamics Versus Kinetics in Nanosynthesis. *Angew. Chem. Int. Ed.* **2015**, *54*, 2022–2051.

117. Ye, S. *et al*. pH Value Manipulated Phase Transition, Microstructure Evolution and Tunable Upconversion Luminescence in Yb^{3+}-Er^{3+} Co-Doped $LiYF_4/YF_3$ Nanoparticles. *Dalt. Trans.* **2015**, *44*, 15583–15590.

118. Yu, S. *et al*. Microwave–Assisted Synthesis of Water–Disperse and Biocompatible $NaGdF_4$:Yb,Ln@$NaGdF_4$ Nanocrystals for UCL/CT/MR Multimodal Imaging. *J. Fluor. Chem.* **2017**, *200*, 77–83.

119. Amouroux, B. *et al.* Importance of the Mixing and High-Temperature Heating Steps in the Controlled Thermal Coprecipitation Synthesis of Sub-5-nm Na(Gd−Yb)F_4:Tm, *Inorg. Chem.* **2019**, *58*, 5082–5088.

120. Aebischer, A. *et al.* Structural and Spectroscopic Characterization of Active Sites in a Family of Light-Emitting Sodium Lanthanide Tetrafluorides. *Angew. Chem. Int. Ed.* **2006**, *45*, 2802–2806.

121. The Clausius-Clapeyron Equation. https://chemed.chem.purdue.edu/genchem/topicreview/bp/ch14/clausius.php.

122. Niu, N. *et al.* Tuning Upconversion Luminescence of $LiYF_4$:Yb^{3+}, Er^{3+}/Tm^{3+}/Ho^{3+} Microcrystals Synthesized Through a Molten Salt Process. *J. Nanosci. Nanotechnol.* **2014**, *14*, 3509–3514.

123. Wang, F. and Liu, X. Upconversion Multicolor Fine-Tuning: Visible to Near-Infrared Emission from Lanthanide-Doped $NaYF_4$ Nanoparticles. *J. Am. Chem. Soc.* **2008**, *130*, 5642–5643.

124. Gao, W. *et al*. Multicolor Upconversion Emission of Lanthanide-Doped Single $LiYF_4$ and $LiLuF_4$ Microcrystal. *Mater. Res. Bull.* **2017**, *91*, 77–84.

125. Zhou, J. *et al.* Ultrasensitive Polarized Up-Conversion of Tm^{3+}–Yb^{3+} Doped β-$NaYF_4$ Single Nanorod. *Nano Lett.* **2013**, *13*, 2241–2246.

126. The Nobel Prize in Chemistry 2016. https://www.nobelprize.org/prizes/chemistry/2016/feringa/lecture/.

127. The Nobel Prize in Physics 2018. https://www.nobelprize.org/prizes/physics/2018/summary/.

128. Liu, D. *et al.* Near-Infrared Light Activates Molecular Nanomachines to Drill into and Kill Cells. *ACS Nano* **2019**, *13*, 6813–6823.

129. Bednarkiewicz, A. *et al*. Optically Stimulated Heating Using Nd^{3+} Doped $NaYF_4$ Colloidal Near Infrared Nanophosphors. *Appl. Phys. B Lasers Opt.* **2011**, *103*, 847–852.

130. Shen, J., Lowe, R. D., and Snook, R. D. A Model for cw Laser Induced Mode-Mismatched Dual-Beam Thermal Lens Spectrometry. *Chem. Phys.* **1992**, *165*, 385–396.